
UNIVERSIDAD NACIONAL AUTÓNOMA DE MÉXICO
MAESTRÍA EN CIENCIAS FÍSICAS
INSTITUTO DE CIENCIAS NUCLEARES

# MULTIPLICITY AND ENERGY DEPENDENCE OF THE TRANSVERSE MOMENTUM DISTRIBUTION OF CHARGED HADRONS IN PROTON-PROTON COLLISIONS

TESIS
QUE PARA OPTAR POR EL GRADO DE:
MAESTRO EN CIENCIAS FÍSICAS (FÍSICA)

PRESENTA: SERGIO ARTURO IGA BUITRÓN

TUTOR PRINCIPAL:

ELEAZAR CUAUTLE FLORES
INSTITUTO DE CIENCIAS NUCLEARES

MIEMBROS DE COMITÉ TUTOR:

VARLEN GRAVSKI
INSTITUTO DE FÍSICA

RUBEN ALFARO MOLINA
INSTITUTO DE FÍSICA

CIUDAD DE MÉXICO, MARZO DE 2019

*"Para mi esposa Alejandra, que estuvo siempre conmigo a lo largo de este viaje"*
*-Con cariño, Sergio*

# Agradecimientos (Acknowledgements)

Agradezco en general al grupo de ALICE-ICN, estudiantes e investigadores, por el trabajo que logramos sacar adelante en conjunto. Por la críticas y sugerencias recibidas a lo largo del proyecto.

Al Dr. Eleazar Cuautle, director de la tesis. Su paciencia y apoyo, tanto en lo académico como en lo personal fueron parte fundamental en la construcción de este proyecto, así como las discusiones sobre los resultados obtenidos.

Al Dr. Antonio Ortiz, miembro del comité tutor. Las largas discusiones y debates sobre la parte técnica del análisis así como la interpretación de los resultados son uno más de los pilares que soportan este trabajo.

Al Dr. Guy Paic. Por su manera muy particular de pensar las cosas, es difícil seguir su forma de pensar, lleva tiempo digerir y desenredar lo que tiene en mente, al final, después de pensarlo un rato (a veces un par de semanas), logras entender y te das cuenta que ¡siempre hay una buena idea detrás! algunas de las cuales quedan plasmadas en esta tesis. Guy me enseñó que los sentimientos y el trabajo no caben en la misma bolsa, decidir con cabeza fría.

Al Dr. Rubén Alfaro, miembro del comité tutor. Por el seguimiento al trabajo realizado desde el inicio de la maestría. Por asesorar las decisiones sobre el rumbo que tomó mi maestría, planificar los tiempos, decidir los cursos a inscribir, etc.

To all the people in CERN that follow and advised this work in SPECTRA-PAG and PWG-LF, especially to Alexander Kalweit, Francesca Bellini, Yasser Corrales and Antonio Ortiz. For the common effort during the analysis and especially during the approvals.

To the groups and institutions that supported me with stay researches, ALICE-GSI and CERN. Both of my stays were really helpful, the first in CERN to introduce my self with the ALICE community, and the second in GSI, where I formally started the data analysis presented in this thesis.

Por último, pero no menos importante, se agradece al ICN, a la UNAM y al posgrado en ciencias físicas, por permitirme ser parte de su comunidad y hacer uso de las instalaciones. A CONACYT por el apoyo con su programa de becas de posgrado, DGAPA-PAPIIT proyecto IN109817.

A mi familia, mis padres Sergio y Beatriz, así como a mis hermanos Daniela y Hector y mi esposa Alejandra. El apoyo moral, consejos y animos me ayudaron a salir adelante.

# Summary

The ALICE (**A L**arge **I**on **Collider E**xperiment) experiment was designed to study the desconfined matter in heavy ion collisions, however, it also includes studies based on pp collisions, like the presented in this work.

This thesis presents an analysis of the measurement of transverse momentum spectra of primary charged particles in pp collisions at $\sqrt{s} = 5.02$ and 13 TeV , for events with at least one charged particle in $|\eta| < 1$ (INEL $> 0$) collected in ALICE experiment. The analyses were done in multiplicity bins, using tracklets for multiplicity estimator at central pseudo-rapidity $|\eta| < 0.8$ and the V0M Percentile Estimator in forward-backward pseudo-rapidity $2.8<\eta<5.1$ for V0A and $-3.7<\eta<-1.7$ for V0C. The spectra were measured in the pseudo-rapidity range of $|\eta| < 0.8$. Significant differences were found between both multiplicity estimators: in the ratios to INEL $> 0$, a saturation effect is observed in the highest multiplicity bins for the V0M case, and, for the tracklets, a gradual increase is observed, which is stronger for higher multiplcity bins. We also present an analysis of the intermediate to high $p_{\mathrm{T}}$ region by extracting the exponent of power law fits in function of multiplicity bins. The integrated yields, from 4 to 10 GeV/$c$, of the spectra in function of multiplicity divided by the INEL $> 0$ one are also presented in comparison with heavy flavor data. In the power law exponents, a similar behaviour is observed, the exponent tends to saturate at high multiplicty for the V0M case, but for the Tracklets case, it tends to continuously decrease.

It seems that most of the differences between the two multiplicity estimators are strongly related with the different physics processes that are selected with the region in which the multiplicity is measured. There is evidence that selecting high multiplicity events in the central barrel is to select jetty-like events. The power law exponent that we reach for high multiplicity in the central barrel is close to 5, that is similar to the one measured for hadrons and photons jets and to the QCD predictions. With the forward-backward multiplicity estimator, the physical processes that we are selecting is a mixture of hard and soft physics. Thats why the ratios to INEL $> 0$ for high multiplicity and also the power law exponents seems to saturate for the high multiplicity V0M bins, it means, for high V0M multiplicity we have contributions from jetty-like and soft events.

The results were compared with three different Monte Carlo (MC) models, PYTHIA 8, PYTHIA 6 and EPOS. It is interesting to see how PYTHIA 6 and 8 can describe, at least qualitatively, the measurements for the intermediate-high $p_{\mathrm{T}}$ region (4 to 10 GeV/$c$), while EPOS, one of the best generators in the description of the soft physics, is very far to describe it. The mechanisms of evolution of both event generators are different, while EPOS uses hydrodynamics to evolve the soft component while the hard component evolves apart, PYTHIA uses pQCD for hard processes and phenomenological models for soft processes, like Color Reconnection and Multiple Parton Interactions, which give a probability of interaction between final and initial partons. Taking into account these models, PYTHIA gives a better description of the $p_{\mathrm{T}}$ spectra analyzed.

# Resumen

El experimento ALICE (de sus siglas en inglés **A L**arge **I**on **Collider E**xperiment), diseñado para estudiar la materia en estado desconfinado en colisiones núcleo-núcleo (AA), también incluye estudios basados en colisiones (pp) como los presentados en esta tesis. El experimento cuenta con múltiples detectores dedicados a realizar diferentes mediciones especificas, y algunos funcionan en conjunto. Por ejemplo, la cámara de proyección temporal (TPC) funciona en conjunto con el detector más interno de ALICE, sistema de rastreo interno (ITS), teniendo como una de sus funciones en común, rastrear las partículas generadas en la colisión. Para el análisis presentado en esta tesis, se utilizaron tres detectores para diferentes propósitos. La TPC en conjunto con el ITS fueron utilizados para seguir la traza de las partículas producidas en la colisión. El ITS ademas de ser esencial para encontrar el vértice del evento, también se utiliza como estimador de multiplicidad en el barril central. Por ultimo, se utilizaron los centelladores V0A y V0C, en conjunto llamados V0M, para medir la multiplicidad en las regiones adelante-atrás. Para este propósito se mide la amplitud de la señal en ambos detectores, la cual después es normalizada y presentada en forma de percentiles.

El estudio de la producción de partículas cargadas, como función de la multiplicidad, en sistemas pequeños en colisión, por ejemplo pp, es una herramienta atractiva para entender similitudes y diferencias entre sistemas pequeños y grandes. Evidencia de similitudes, como efectos colectivos, bien conocidos en colisiones núcleo-núcleo AA, han sido encontradas experimentalmente en sistemas pequeños.

Se ha observado continuidad de ciertas mediciones de pp con pA y AA en función de multiplicidad, como la producción de partículas extrañas en función de multiplicidad. Las mediciones de pp, pA y AA parecen evolucionar de manera continua y con suaves traslapes entre si, desde una decena de partículas cargadas (colisiones pp) hasta miles de ellas (AA). Aunque cabe mencionar que esta comparación se hizo utilizando solamente el estimador V0M.

El espectro de momento transverso ($p_{\mathrm{T}}$ ) de hadrones cargados primarios es una herramienta muy útil para entender la física de las colisiones. Dividiendo la muestra en intervalos de multiplicidad (número de partículas cargadas producidas en el evento en una región cinemática), somos capaces de estudiar el sistema con más detalle.

El capítulo uno está dedicado a explicar el marco teórico y algunos de los conceptos que necesitan ser clarificados para poder entender los resultados. Esta sección contiene una pequeña introducción al modelo estándar y a la Cromodinámica Cuántica (QCD), así como una idea general de algunos de los modelos fenomenológicos que han demostrado estar en buen acuerdo con los datos medidos de algunos observables. El modelo estándar es una teoría que estudia la materia en su forma más fundamental y sus interacciones. Lo aceptado hasta ahora es que existen cuatro de ellas: interacción fuerte, débil, electromagnética y la gravitatoria. Uno de los propósitos de las extensiones modelo estándar es el de la gran unificación de todas las interacciones, por el momento, se han unificado las interacciones electromagnéticas y las débiles en lo que se conoce como el modelo electro-débil.

La QCD, es la teoría dedicada a estudiar las interacciones fuertes que ocurren durante las colisiones de hadrones. Dentro de QCD, podemos distinguir entre QCD perturbativa y QCD no perturbativa. La primera describe las interacciones o eventos duros (pueden hacerse cálculos analíticamente) mientras

la segunda describe los procesos de física suave, de QCD no perturbativa donde no se pueden realizar los cálculos analíticos, de manera que se tiene que recurrir a la fenomenología para describir la parte suave de las colisiones.

Los eventos duros, que como mencionamos anteriormente y que son descritos por la QCD perturbativa, son usualmente eventos con Jets. Un Jet es un conjunto de partículas colimadas producidas por un partón dispersado en una interacción muy energética. Generalmente, este es acompañado por otro partón en dirección opuesta en el plano transverso, aunque a veces pueden ser tres partones con $\frac{2}{3}\pi$ de separación, y que son los causantes de generar los conocidos eventos tipo "mercedes". Hay evidencia que eventos con alta multiplicidad en el barril central son eventos Jets, esto será importante al momento de explicar los resultados.

En el capítulo dos se presenta de manera general los detectores de ALICE que se usaron para las mediciones presentes en esta tesis. Dentro de los detectores utilizados se encuentran los encargados de trazar la ruta de las partículas generadas en la colisión (la cámara de proyección temporal (TPC) y el sistema de rastreo interno (ITS)) así como también los detectores de centelleo adelante-atrás V0, utilizados para medir la multiplicidad por medio de la amplitud medida en su región de operación.

En el tercer capítulo se describe el proceso de medición de manera detallada. Esto incluye una descripción detallada de las correcciones aplicadas a los datos crudos, comenzando por los efectos de los detectores, por ejemplo, la eficiencia de rastreo, contaminación por partículas secundarias etc. Junto con los resultados, es una parte importante del trabajo hecho. Básicamente, dos tipos de correcciones son aplicadas a los datos crudos, las que presentan una dependencia con $p_{\mathrm{T}}$ , y las correcciones al factor de normalización.

Las correcciones realizadas a nivel de trazas, es decir, las que dependen de $p_{\mathrm{T}}$ , se describen a continuación: primero tenemos la contaminación de partículas secundarias, entendiendo por secundarias todas aquellas partículas que que provienen de decaimientos débiles, por lo cual no provienen del vértice primario de la colisión. Para corregir por este efecto, se utiliza una técnica basado en datos llamado "feed-down". Básicamente, este método ajusta las distribuciones de distancia de las trazas con el vértice primario de las partículas primarias y secundarias generadas en el MonteCarlo (MC) a la distribución de los datos, será descrito con más detalle en la sección correspondiente. Después tenemos la corrección por eficiencia de rastreo, esta corrección se hace debido a que el detector no es capaz de rastrear en su totalidad todas las partículas generadas en la colisión, por este motivo, usando también un método basado en datos "particle-composition", se corrige por este efecto. Para esta corrección de utilizan las eficiencias de cada una de las partículas cargadas y las distribuciones medidas por ALICE para hacer una eficiencia pesada por la abundancia de cada especie, este método es más preciso que calcular solo con MonteCarlo, pues se sabe que este no reproduce la composición química de los datos. Por último tenemos la pérdida de señal que se da en la selección de eventos, es decir, la modificación a la forma del espectro debido a los eventos que no fueron seleccionados, esta corrección se calcula con la razon entre los espectro antes y después de la selección de eventos. Esta última corrección es basada en simulaciones MC.

Después tenemos las correcciones que son a nivel evento, las cuales solamente modifican la normalización o escala de los espectros. En este caso tenemos dos correcciones, la primera es aplicada debido a la cantidad de eventos perdidos en la selección del trigger INEL $> 0$, la cual se calculó en base a simulaciones con PYTHIA 6. La segunda es calculada para corregir por todos aquellos eventos que fueron desechados por no tener un vértice con la calidad requerida, se calculó utilizando datos.

Los errores sistemáticos básicamente indican el rango de error que tiene el resultado debido a los cortes y parámetros de medición así como las técnicas aplicadas. Para esto, los cortes son variados, y el resultado obtenido de la variación es comparado con el resultado nominal, es decir, con los cortes optimizados. Esto se hace para cada uno de los cortes y correciones aplicadas a los datos de manera

que el error calculado sea lo más completo posible.

En el cuarto capítulo, se muestran las mediciones de los espectros de $p_{\mathrm{T}}$ para hadrones cargados primarios producidos en colisiones, usando dos estimadores de multiplicidad. Uno a pseudorapidez central $|\eta| < 0.8$ y otro a pseudorapidez adelante-atrás $-3.7 < \eta < -1.7$ and $2.8 < \eta < 5.1$, con el propósito de estudiar las diferencias causadas por la selección de multiplicidad en diferentes ventanas de pseudorapidez. El análisis se realizó para colisiones pp, a dos energías de centro de masa de la colisión, $\sqrt{s} = 5.02$ y $\sqrt{s} = 13$ TeV.

Una de las cosas que llamó nuestra atención es el endurecimiento de los espectros conforme la multiplicidad crece, efecto presente con el estimador a pseudorapidez central. Este efecto se observa al calcular las razones de los espectros medidos en intervalos de multiplicidad divididos entre el espectro INEL $> 0$. Para el estimador V0M, se observa un efecto de saturación y no un crecimiento constante. Esto surge de hacer un estudio más detallado de la componente dura de los espectros a alto $p_{\mathrm{T}}$ , ya que a bajo $p_{\mathrm{T}}$ el comportamiento entre ambos estimadores de multiplicidad se presenta muy similar. Para el estudio del $p_{\mathrm{T}}$ intermedio a alto, fueron ajustadas a las distribuciones de $p_{\mathrm{T}}$ para $p_{\mathrm{T}} > 4$ GeV/$c$ leyes de potencia, y la evolución del exponente del ajuste, como función de la multiplicidad, es uno de los resultados importantes a discutir, pues se muestran resultados que ilustran de mejor manera el efecto observado en las razones antes mencionadas. Se observa una tendencia del exponente ajustado a ir hacia el valor de 5, para alta multiplicidad en el barril central, el cual es muy similar a lo que se ha medido para Jets de fotones y hadrones y coinciden con la predicción de pQCD. Mientras que para el estimador de multiplicidad V0, se observa una saturación. Lo anterior, tiene que ver con el tipo de procesos de física que estamos seleccionando cuando hacemos un corte de multiplicidad en diferentes regiones de pseudo-rapidez. Si seleccionamos alta multiplicidad en el barril central, significa que estamos seleccionado eventos con Jets, es decir, estamos seleccionado eventos duros. Por otra parte tenemos que en alta multiplicidad en el estimador V0 tiene mezcla de alta y baja multiplicidad en el barril central, en este sentido, este es una mezcla de procesos físicos suaves y duros, lo que lleva al exponente a evolucionar hacia esta saturación.

En el presente trabajo también se estudia la razón de los espectros integrados sobre la referencia INEL $> 0$, como función de la multiplicidad, para una ventana de $p_{\mathrm{T}}$ alto ($4 < p_{\mathrm{T}} < 10$ GeV/$c$) y es comparada con resultados para partículas con sabores pesados. Similitudes son encontradas entre partículas cargadas de alto $p_{\mathrm{T}}$ y hadrones de sabores pesados, sugiriendo un mismo mecanismo de producción detrás de esto.

También se presentan los resultados en comparación con generadores de eventos MonteCarlo, como EPOS-LHC y PYTHIA 6 y 8. Es importante comparar diferentes modelos que tratan de manera diferente la evolucion del bulto creado en las colisiones. Mientras EPOS-LHC usa hidrodinámica para evolucionar la componente suave de la colisión, PYTHIA 6 y 8 usa modelos de QCD no perturbativa como por ejemplo el de reconexión por color, el cual se sabe, induce patrones de flujo radial. De las comparaciones realizadas en este trabajo, se puede concluir que PYTHIA con su mecanismo de reconexión por color es bueno reproduciendo los resultados para $p_{\mathrm{T}}$ intermedio y alto (resultado basado en términos de los exponentes ajustados) al menos de manera cualitativa, mientras EPOS esta lejos de tener el comportamiento de los datos, esto es de alguna manera una sorpresa, ya que hasta ahora EPOS es el generador que usualmente mejor describe los resultados producidos en LHC para colisiones pp, aunque cabe mencionar que muchos de ellos, como el $p_{\mathrm{T}}$ promedio en función de multiplicidad, son observables que están altamente gobernados por el bajo momento transverso.

Por último en el capítulo cinco se presentan las conclusiones. Se han medido las razones de las distribuciones de momento transverso en intervalos de multiplicidad, normalizados a la referencia INEL $> 0$. Las distribuciones de momento transverso fueron ajustadas a una ley de potencia para $p_{\mathrm{T}}$ intermedio y alto ($p_{\mathrm{T}} > 4$ GeV/$c$) y el exponente del ajuste es presentado y comparado con diferentes energías y modelos.

La producción integrada fue comparada con los resultados de hadrones con sabores pesados, indicando un mecanismo general que da origen a la producción de hadrones.

# Contents

# Chapter 1

# Introduction

This section is dedicated to explain the theoretical framework and some of the concepts that need to be clarified in order to understand the results. This section contains a brief introduction of the Standard Model and the Quantum Chromodynamics, as well as a general idea of some of the phenomenological models that are in good agreement with experimental data. In the last section of this chapter, a synopsis of the thesis is presented.

## 1.1 The Standard Model

The Standard Model is the field of the physics that describes the matter in their most fundamental level. It can describes three of the four fundamental forces in the nature, the strong, the weak and the electromagnetic, while not describing the gravitational force. The unification of the electromagnetic and weak interactions into the $eletro - weak$ theory is one the most important results of the Standard Model. The Standard Model also classifies the fundamental particles in fermions (fractional spin) and bosons (integer spin). The fermions themselves can be classified in leptons and quarks. The elementary particles table can be observed in figure 1.1. All known matter is contructed from these fundamental particles. The $electro - weak$ theory describes the interaction of matter via $W^{\pm}, Z$ and $\gamma$ bosons. The field that studies the strong interaction that only occurs between quarks and gluons is the Quantum Chromodynamics. In the high energy hadron collisions, such as the ones studied in this thesis, the particles that actually interact are the quarks and gluons.

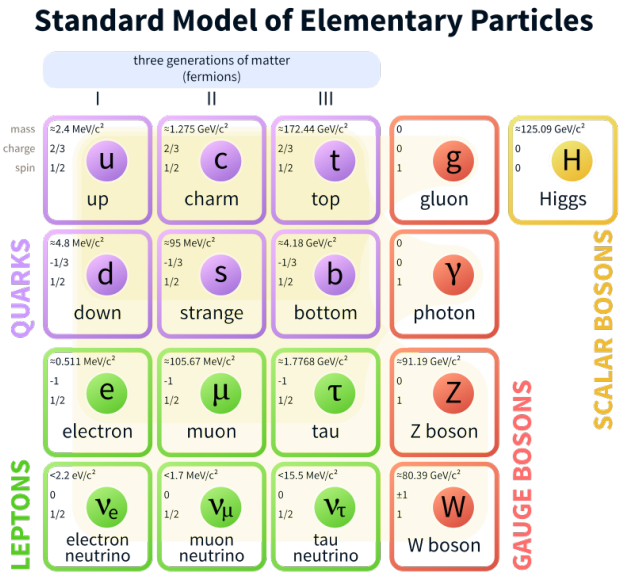


Figure 1.1: Table of elementary particles.[13]

## 1.2 Quantum Chromodynamics

In particle physics, Quantum Chromodynamics (QCD) is the field that studies the strong interactions, which occurs between quarks and gluons.

Analogous to the electrical charge, the quarks and gluons have a color charge. The gluons are the "force carriers" like photons in Quantum Electrodynamics. One of the properties of the quarks and gluons, is that it is not possible to observe them isolated, they can only exist in hadrons or in high-density, high-temperature system (Quark Gluon Plasma) that is created in high energy nucleus-nucleus collisions.

At large scale, i.e. protons and neutrons, the strong interaction is responsibly of binding the nucleons in the atom's nuclei, overcoming the electromagnetic repulsion of protons by exchanging $\pi$,$\rho$ and $\omega$ mesons. At small scale, the strong interaction is responsible for quarks staying together to form hadrons by exchanging gluons. The theory states that partons come in three different colors, green, red, and blue. Quarks can be found in two kind of hadrons, the baryons, which are composed of three valence quarks, and mesons, which are made up of a quark anti-quark valence pair. The hadrons need to be colorless (or white), that is to say, a baryon can be only formed by three quarks of different color (that "compound the white") and the mesons are formed by a color-anticolor pair that is also colorless.

The QCD processes can be separated into soft (non-perturbative) and hard (perturbative) scatterings. The hard QCD processes can be described by the perturbative QCD computations but the soft part can only be modelled phenomenologically. As will be described, the transverse momentum is one of the important observables that can be measured in order to characterize the collisions. The hadrons that come from parton hadronization of soft processes dominate the bulk of charged particle production at low momentum, while the high momentum region is dominated by hard dispersions that origin the jets. At the end, at "intermediate $p_{\mathrm{T}}$ ", we have a mixture of soft and hard physics [3].

### 1.2.1 The QCD Lagrangian density

The expression for the QCD Lagrangian density is shown next in equation 1.1

$$\mathcal{L}_{QCD} = \sum_q \bar{\psi}_{q,a}(i\gamma^\mu \partial_\mu \delta_{ab} - g_s \gamma^\mu t^C_{ab} \mathcal{A}^C_\mu - m_q \delta_{ab})\psi_{q,b} - \frac{1}{4} F^A_{\mu\nu} F^{\mu\nu}_A \tag{1.1}$$

where $\gamma^\mu$ are the Dirac $\gamma$-matrices. The $\psi_{q,a}$ are the quark-field spinors for a quark of flavor $q$ and mass $m_q$, with color index $a$ that runs from 1 to number of colors ($N_c = 3$). The $A^C_\mu$ correspond to the gluon fields, with C running from 1 to $N_c^2 - 1 = 8$ (eight kind of gluons). The $t^C_{ab}$ correspond to eight 3 x 3 matrices that are the generators of the SU(3) group. The $g_s$ is the QCD coupling constant, and $F^A_{\mu\nu}$ is the field tensor given by

$$F^A_{\mu\nu} = \partial_\mu \mathcal{A}^A_\nu - \partial_\nu \mathcal{A}^A_\mu + g_s f_{ABC} \mathcal{A}^B_\mu \mathcal{A}^C_\nu \tag{1.2}$$

where $f_{ABC}$ are the structure constants of the SU(3) group.

### 1.2.2 The transverse momentum ($p_{\mathrm{T}}$) and the power law exponent

The transverse momentum distribution is one of the most important observables that can be measured from the particles produced during a collision. It is important because is always associated with the physics that happened at the vertex, while the longitudinal momentum may just been left over by from the beam particles. In that way, the $p_{\mathrm{T}}$ is a parameter to identify the soft and hard physical processes that may occurs during a collision. It is not a rule but, usually, soft physics (low $p_{\mathrm{T}}$ ) is

considered to be in the region $p_T$ <2 GeV/c and hard processes (high $p_T$ ) is considered to in the region $p_T$ >10 GeV/c, and a mixture of processes occurs at intermediate $p_T$ . As mentioned before, the non-pertubative QCD is in charge to describe the low $p_T$ region while pertubative QCD studies the high $p_T$ region. Low $p_T$ is modeled phenomenologically while hard $p_T$ can be computed using QCD, so mid $p_T$ is a mixture of models and QCD computation. The $p_T$ is also useful to identify geometries in the events, for example, to identify events with Jets (Jets will be described latter) the highest $p_T$ particle in the event should be find in order to determine the center of the cone.

Perturbative QCD describes the high $p_T$ distributions as a power law function ($C\frac{1}{{p_T}^n}$) where $C$ is the scale and the exponent $n$ is parameter that tell us how hard the collision is. In that way, this observable is also important to compare experimental results with the theory. The exponent predicted by pQCD is 4. We have extracted the exponent from the measured data with a power law fit and the results are interesting.

### 1.2.3 Soft and Hard QCD processes

As mentioned before, the QCD processes can be divided into soft and hard processes and the transverse momentum distribution of hadrons is composed by the two parts aforementioned. The soft processes, modelled phenomenologically and dominant at the low momentum region, are mainly diffractive processes, where either two (double diffractive) or one (single diffractive) of the colliding hadrons are destroyed. Elastic collisions, where both protons remain just with a change in their momentum, are also included in the soft QCD sector in some models (i.e. PYTHIA 8 [4]). Other models also include hydrodynamical evolution of the soft component (i.e EPOS-LHC [5]). The soft component of the collisions is also usually called **U**nderlying **E**vent (UE).

The hard scatterings occur when two partons "violently" collide, exchanging a large amount of momentum and are being dispersed in opposite directions (in the transverse plane). The high energy partons hadronize to form a cone of particles. The cone of particles is called Jet. A picture of a typical proton-antiproton collision can be observed in figure 1.2.

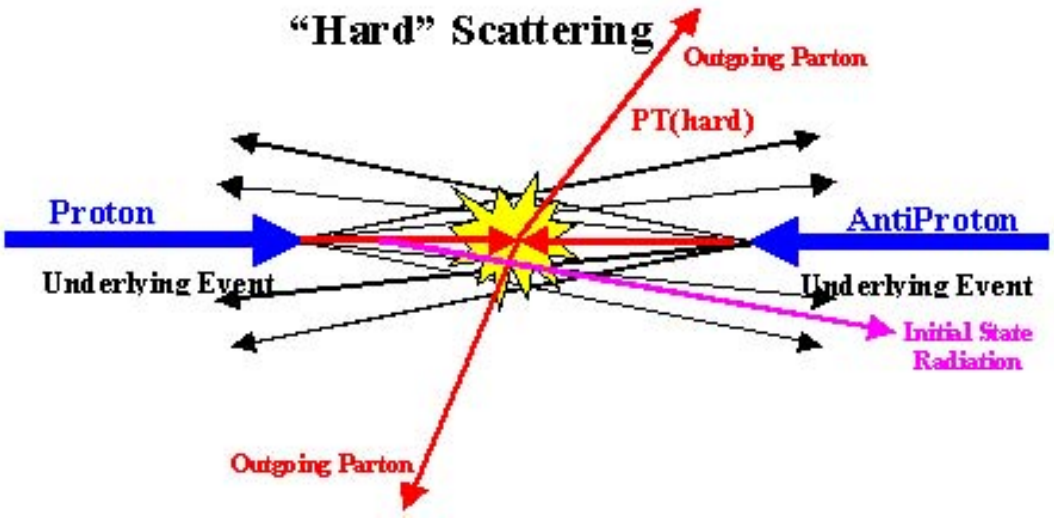


Figure 1.2: Typical proton-antiproton collision, the underlying event can be observed in black while the hard component can be observed in red.

## 1.3 Multi-Parton Interactions and Color Reconnection

It is possible to have more than one (semi)hard scattering in a single proton-proton event, i.e. Multi Parton Interactions (MPI). The probability increases with the center of mass energy ($\sqrt{s}$), since lower $\sqrt{s}$ decreases x-Bjiörken to lower values (which will be discussed in next section), causing it to be in a more gluon dense region. Experimental evidence of MPI has been found [6].

Some models, like PYTHIA 6 and 8, take into account that in MPI events, partons from different scatterings can interact via the **C**olor **R**econnection (CR) mechanism. The partons can also interact with the beam remnants. The probability for a (semi)hard scattering to be reconnected with another is given by

$$P = \frac{(p_{\mathrm{T}\,0} \cdot Range)^2}{(p_{\mathrm{T}\,0} \cdot Range)^2 + {p_{\mathrm{T}}}^2} \tag{1.3}$$

where $p_{\mathrm{T}}$ is the scale of transverse momentum for the hard scattering ($2 \to 2$), *Range* is a parameter that can take any value between 0 and 10, and $p_{\mathrm{T}\,0}$ is an energy dependent constant. This and other CR models included in PYTHIA 8 can be consulted from [14].

## 1.4 Fragmentation functions and Parton Distribution Functions

The **P**arton **D**istribution **F**unctions (PDFs) tell us that the probability of finding a parton inside a hadron with a longitudinal fraction of the hadron momentum "$x$" at a squared energy scale $Q^2$. Experimental results of the proton PDFs measurements can be observed in figure 1.3.

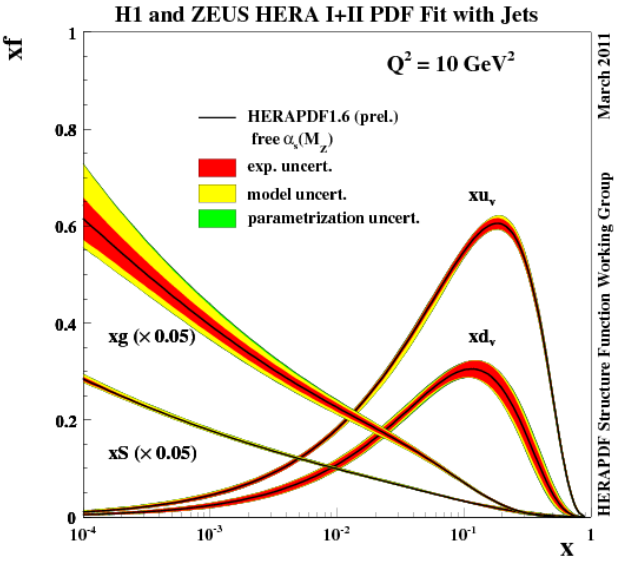


Figure 1.3: Parton distribution functions as a function of x.

It can be observed from the previous figure, smaller values of x lead to a higher gluons and sea quarks distribution, making it more likely to have an MPI event.

**F**ragmentation **F**unctions (FFs) basically describe how the partons become hadrons. FFs play a role as the non-perturbative ingredient in the QCD factorization theorem. In general the next three processes have played and continue playing an important role in the study of the FFs:

- single-inclusive hadron production in electron-positron annihilation, $e^+ + e^- \to h + h$.
- single-inclusive deep-inelastic lepton-nucleon scattering, $l + N \to l + h + X$.
- single-inclusive hadron production in pp collisions, $p + p \to h + X$.

In the previous cases QCD factorization theorems schematically reads:

$$\sigma^{e^+e^- \to hX} = \hat{\sigma} \otimes FF, \tag{1.4}$$

$$\sigma^{lN \to lhX} = \hat{\sigma} \otimes PDF \otimes FF, \tag{1.5}$$

$$\sigma^{pp \to hX} = \hat{\sigma} \otimes PDF \otimes PDF \otimes FF, \tag{1.6}$$

where $\hat{\sigma}$ indicates the respective process-dependent partonic cross section that can be computed in pQCD.

## 1.5 Jet production in pp collisions

It is important to define what a jet is, since there is evidence that this kind of structures are usually found in high multiplicity (at mid-pseudorapidity) pp collisions [9]. Jets are collimated sprays of particles, produced in hard parton-parton scatterings. The study of jet production and fragmentation allows us to test our understanding of perturbative and non-perturbative aspects of QCD [7]. The cone radius of the jet is defined as

$$R = \sqrt{\Delta\Phi^2 + \Delta\eta^2} \tag{1.7}$$

There are many algorithms to identify jets in pp collisions, one of the most recent and frecuently used is FastJet anti-$k_T$ [8].

Usually, due to energy and momentum conservation, the jets come with a recoil, a cone of particles in the opposite direction in the transverse plane. This effect is the responsibly of the characteristic shape of the $\Delta\eta$-$\Delta\Phi$ di-hadron correlations, where the trigger hadron (usually the highest $p_T$ hadron in the event) is correlated with the associated particles (usually lower $p_T$ particles than the trigger hadron), as observed in figure 1.4 taken from [10]. A pronounced peak structure with its center at (0,0) is caused by the jet, the cone of particles collimated with the leading hadron. The structure at $\Delta\Phi = \pi$, is created by the recoil of the jet, that can freely move in eta but is always in opposite direction with respect to the jet in the transverse plane.

The $p_T$ distributions of jets is also an important observable for the high $p_T$ studies. Since we are not measuring directly jets in this analysis, but we know that in high multiplicity in the central barrel events you have more jets abundance, we measure the power law exponent of high multiplicity in the central barrel events and compare with the results measured for jets, the results are very close. The exponent measured for jets by CDF [11] and D0 [12] are arround 4.5.

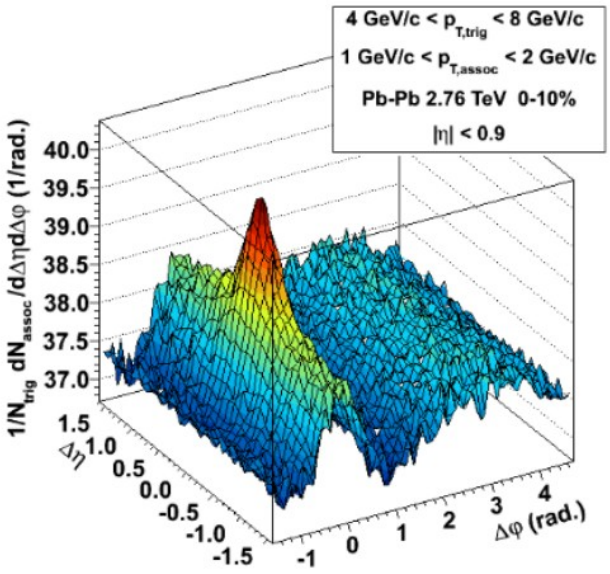


Figure 1.4: $\Delta\eta$-$\Delta\Phi$ di-hadron correlations measured in ALICE.

## 1.6 Multiplicity selection in pp collisions

The events in AA collisions are usually classified in centrality classes. This approach is not practical for pp collisions since it is very hard to measure the impact parameter of the colliding protons. Instead of centrality, pp collisions can be classified as a function of the charged particles produced during the event. Many important and recent multiplicity dependent results in pp collisions have been published, e.g. the strangeness enhancement with multiplicity [1] and the larger than linear enhancement of heavy flavor production [2]. Important results from these publications can be observed in figure 1.5.

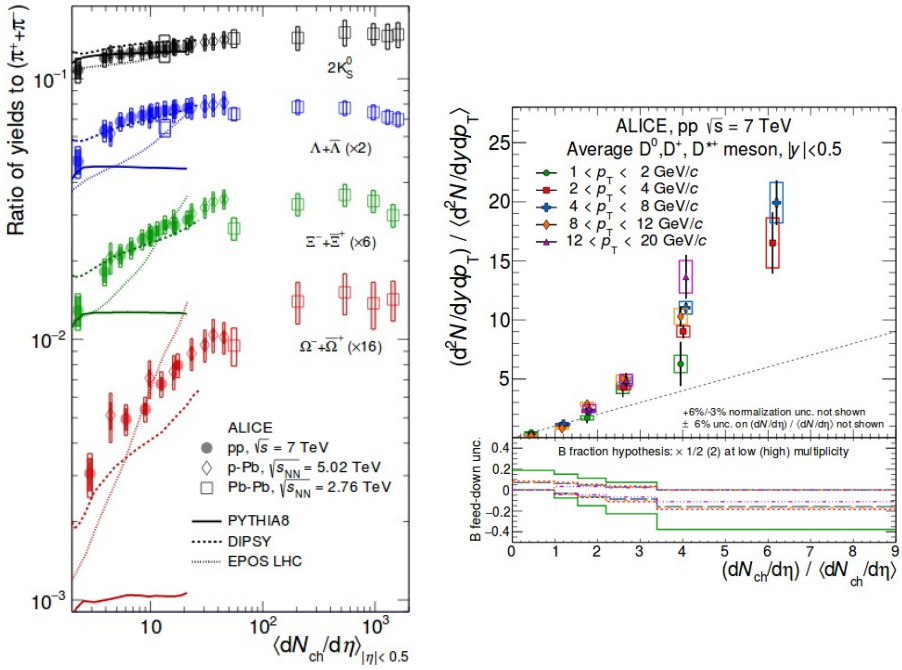


Figure 1.5: On the left, ratios of some strangeness and multi-strangeness particle yields to pions. On the right relative production of D mesons in function of multiplicity for different $p_{\mathrm{T}}$ cuts.

As can be observed from the previous figures, in the strangeness sector, the pp, pPb and AA results are connected via the mean multiplicity of the event classes. An interesting comparison of the results of high $p_{\mathrm{T}}$ charged hadrons and hadrons from the heavy flavor sector will be shown and discussed in the results of this thesis.

Two multiplicity estimators were used for this analysis. One at forward rapidity, based on the V0 detectors, and the other at central rapidity, based on the SPD sub-detector of the ITS. A detailed description of the multiplicity estimators will be given in the next chapters.

We can observed how important it can be to measure the evolution in function of multiplicity for observables in pp collisions if we want to compare with other colliding systems. Also it can be useful to study the different kind of physical processes that occurs in pp collisions, as described in previous section, by selecting high multiplicity events in the central barrel we are selecting jetty events, while using the V0M, a mixture of different physics is present.

## 1.7 On this thesis

A general description of the ALICE detectors that were used for measurement in this analysis, i.e. TPC, ITS, and V0 forward-backward scintillators, is presented in this thesis in chapter 2.

The measurement procedure will be also presented in chapter 3 section 3.5. A detailed description of the corrections applied to the raw data in order to compensate the detector effects, *i.e.* tracking efficiency, secondary particles contamination etc., is also presented. Together with the results, this is a very important part of the work done. Basically, two kind of corrections were applied, the $p_{\mathrm{T}}$ dependent, and the corrections to the normalization factor.

The computation of the systematic uncertainties will be also described in detail in chapter 3 section 3.7 . The systematics basically give us an error range due to the measurements cuts and techniques. Basically, the cuts are variated into a considerable range and the results after the variations are compared with the nominal ones (the nominal results are the ones obtained with the nominal values for all the cuts). Simplifying, the systematic uncertainties give us an idea of how precise is our measurement.

Then, the results and a comparison of the results with Monte Carlo event generators and models, like EPOS-LHC and PYTHIA 6 and 8, is also included in chapter 4. It is important to compare different MC models which have a very different approach for the evolution of the bulk created in the collisions. While EPOS-LHC uses hydrodynamics to evolve the soft component of the collisions, PYTHIA 8 uses the so called Color Reconnection mechanism, which has been proven to produce radial flow patterns.

Finally conclusion can be observed in chapter 4 section 4.2.

# Chapter 2

# The ALICE experiment

The ALICE experiment is one of the seven experiments located at the LHC at CERN. It is designed to study the hot system created in heavy-ion collisions, the so called strongly-interacting Quark Gluon Plasma (sQGP). This is done by studying the particles that come from the dense hot medium as it expands and cools down. The experiment is also capable of identifying most of the particles produced in the collisions. ALICE is comprised by many detectors, a scheme of these detectors can be observed in figure 2.1.

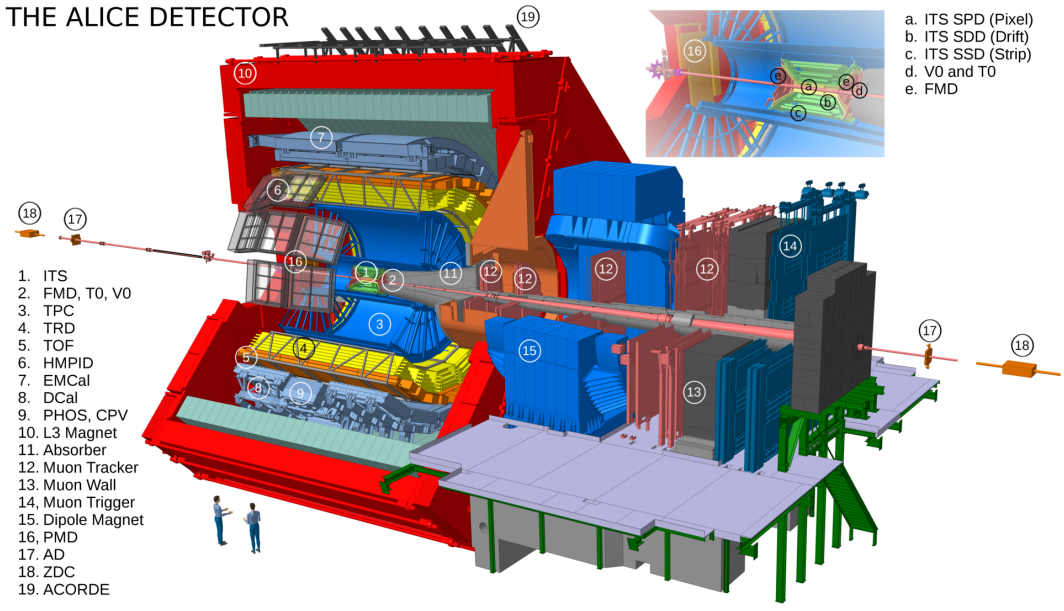


Figure 2.1: The ALICE experiment and its detectors [15].

The ALICE detectors used in this analysis, and their purpose, can be observed in table 2.1. This chapter is dedicated to briefly explaining the detectors used. More detailed information of all detectors can be consulted from the ALICE Technical Design Report [16].

| **Detector** | **Used by** |
|---|---|
| TPC | Tracking |
| ITC | Tracking (SPD, central multiplicity estimator) |
| V0A and V0C | Trigger and forward multiplicity estimator |

Table 2.1: ALICE detectors used in this analysis and their purpose.

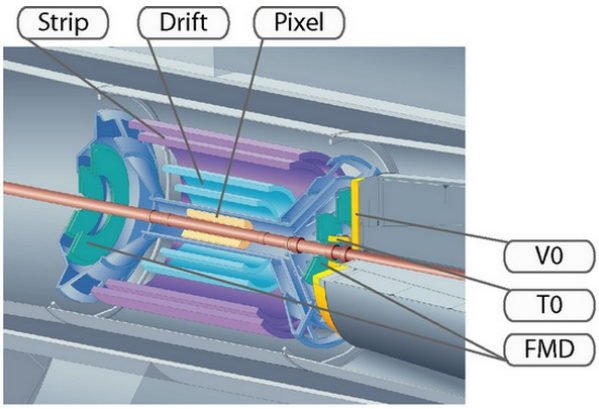


Figure 2.2: ITS scheme and its sub-detectors, SPD, SDD and SSD.

## 2.1 Inner Tracking System

The **I**nner **T**racking **S**ystem (ITS) is the ALICE detector that is closest to the interaction point. It is designed to accomplish three main functions:

- Reconstruction of primary vertex and secondary vertices
- Particle identification and tracking at low-momenta
- Improvement of the momentum and angular measurements of the TPC

The detector is composed of six cylindrical layers. It covers the central pseudo-rapidity region, $|\eta| < 0.9$, for events that have a primary vertex in $Z_{\text{vtx}} \approx \pm 10.6$ cm. The two innermost layers make up the **S**ilicon **P**ixel **D**etectors (SPD), the third and forth layers the **S**ilicon **D**rift **D**etectors (SDD) and the outer two layers, the **S**ilicon **S**trip **D**etectors (SSD). A diagram with the three ITS sub-detectors can be seen in figure 2.2.

### 2.1.1 Silicon Pixel Detectors

The SPD is fundamental to determine the position of the primary vertex and secondary vertices. This sub-detector works in a region where the track density is close to 50 tracks/cm$^2$. The detector must be able to operate in a relative high-radiation environment.

The SPD is composed by two silicon micro-pattern layers with true two-dimensional readout. Some of its characteristics include geometrical precision, double-hit resolution, speed, simplicity of calibration and easy alignment. The trade-off of using very high segmentation is a large number of connections and electronic channels.

### 2.1.2 Silicon Drift Detectors

The two intermediate layers of the ITS. They were chosen because their capacity of providing tracking and $\mathrm{d}E/\mathrm{d}x$ information. The SDD, like the gaseous drift detectors, exploit the measurement of the transport time of the charge deposited by a particle going through it.

### 2.1.3 Silicon Strip Detectors

The two outermost layers of the ITS. The SSD consist of 1698 double-sided micro strip silicon devices. It is efective at providing $\mathrm{d}E/\mathrm{d}x$ information to help with particle identification and to match up with

TPC tracks.

## 2.2 Time Projection Chamber

The **T**ime **P**rojection **C**hamber (TPC) is the most important ALICE detector for the central barrel tracking. It is designed to reconstruct up to 20,000 tracks coming from primary and secondary particles produced during the collisions, in the kinematic window of $|\eta| < 0.9$. A TPC scheme can be observed in figure 2.3.

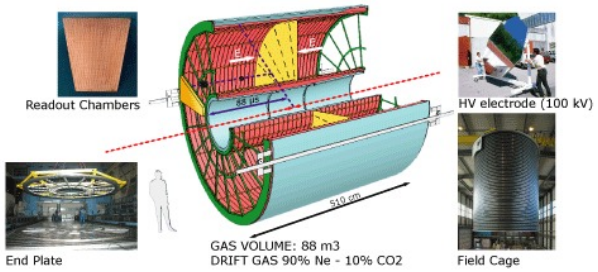


Figure 2.3: ALICE TPC scheme.

In general, the TPC detectors consist of a gas filled volume, inside an electro-magnetic field, with an electron collection system. High energy particles travels into the cylinder ionizing the gas, striping electrons, which are collected in the covers (multi-wire proportional chambers) of the cylinder. In figure 2.4 it is possible to observe how a generic TPC works.

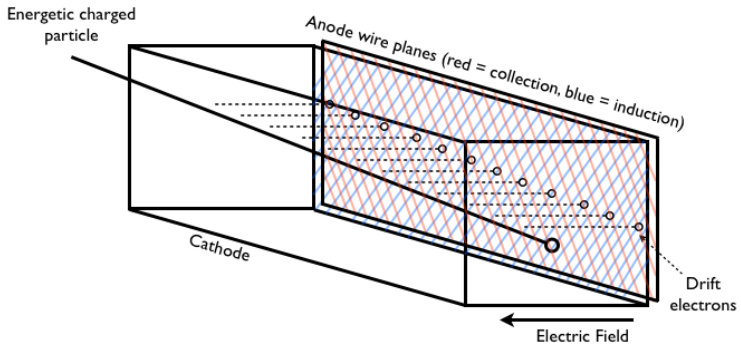


Figure 2.4: Generic TPC cartoon. High energy particles ionize the gas inside the TPC, which strip electrons that are collected in the multi-wire proportional chambers.

### 2.2.1 TPC design considerations

The most important TPC design considerations are shown next.

- **Acceptance:** It covers the pseudo-rapidity window of $|\eta| < 0.9$ and it matches the ITS, TRD and TOF pseudo-rapidity windows. To achieve it, the TPC has an inner radius of about 80 cm, an outer radius of about 250 cm and an overall length in the beam direction of 500 cm.

- **Read-out chambers:** They cover the two end caps of the TPC cylinder, a total area of 32.5 $m^2$. There are about 570 000 readout pads with three different sizes varying from 0.3 $cm^2$ near the inner radius to 0.9 $cm^2$ near the outer radius.
- **Material budget:** It needs to be optimized to minimize the scattering of particles with the detector and the secondary-material particle production. The overall thickness of the TPC was kept to less than 3% of a radiation length.

## 2.3 The V0 detector

The V0 detector consist of two discs (V0A and V0C) made of plastic scintillator tiles that are read out by optical fiber. They cover the forward-backward pseudo-rapidity windows of (2.8< $\eta$ <5.1) for V0A and (-3.7< $\eta$ <-1.7) for V0C. The V0 detector is mostly used as a Minimum Bias off-line trigger (signal in both scintillators is required), forward-backward multiplicity estimator, and for the centrality determination in AA collisions. A scheme of V0 detector can be observed in figure 2.5.

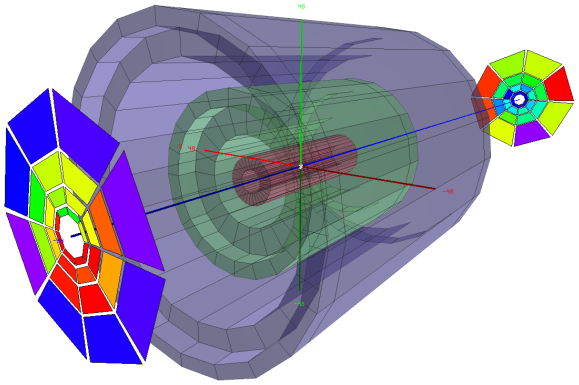

Figure 2.5: V0A and V0C scintillators. In the center, the three ITS sub detectors.

### 2.3.1 V0 detector as a multiplicity estimator in pp collisions

The amplitude of V0A & V0C detectors, usually called V0M amplitude, is one of the ALICE multiplicity estimators. The multiplicity estimator is given in percentiles of the integrated signal as observed in 2.6. For the analysis presented in this thesis, MB trigger binning was used.

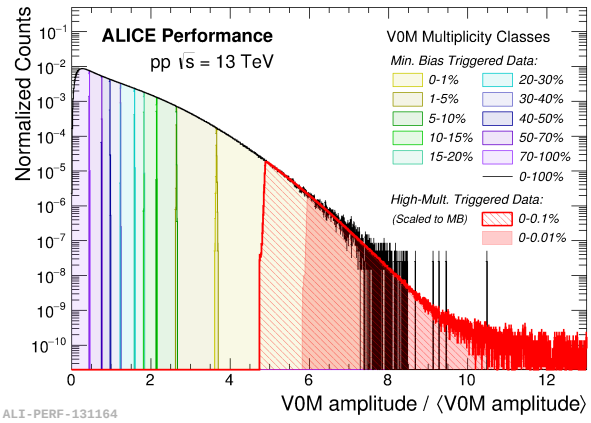


Figure 2.6: V0M multiplicity bins for MB and hign multiplicity triggers.

# Chapter 3

# Data analysis

## 3.1 Data and MC samples

### 3.1.1 pp at $\sqrt{s} = 5.02$ TeV analysis sample

For the pp collisions at $\sqrt{s} = 5.02$ TeV we have used the period **LHC15n pass 3**. The Monte Carlo (MC) simulations sample used for the corrections and the computation of the systematic errors are based on PYTHIA 6 (Perugia-11) and PYTHIA 8 (Monash) pp event generators with the detector response modelled in GEANT 3, the periods used for the MC simulations are **LHC16k5b** and **LHC16k5a** respectively. Only runs with Global Quality 1, which mean events that were taken without detector failures, on the run condition table were used.

The sample contain low and high intensity runs, that were analyzed separated and merged at the end. The list of runs analized is:

Low intensity runs:
244340, 244343, 244355, 244351, 244359, 244364, 244377

High intensity runs:
244411, 244416, 244418, 244421, 244453, 244456, 244480, 244481, 244482, 244483, 244484, 244531, 244540, 244542, 244617, 244618, 244619, 244626, 244627, 244628

### 3.1.2 pp at $\sqrt{s} = 13$ TeV analysis sample

For the pp collisions at $\sqrt{s} = 13$ TeV we have used the period **LHC15f pass 2**, the selection of runs was taken from a previous analysis [21] and correspons to the runs with Global Quality 1 in the run condition table. The MC simulations samples are also based on PYTHIA 8 (Monash) and PYTHIA 6 (Per-11) pp event generators with the detector response modeled in GEANT 3, the periods for the MC are **LHC15g3a3** and **LHC15g3c3** respectively. The list of analized runs is:

List of runs:
225026, 225031, 225035, 225037, 225041, 225043, 225050, 225051, 225052, 225753, 225757, 225762, 225763, 225766, 225768, 225106, 225305, 225307, 225309, 225310, 225313, 225314, 225315, 225322, 225576, 225578, 225579, 225586, 225587, 225705, 225707, 225708, 225709, 225710, 225716, 225717, 225719, 226062, 226170, 226220, 226225, 226444, 226445, 226452, 226466, 226468, 226472, 226476, 226483, 226495, 226500

## 3.2 Event selection

The event selection was done in the same way that in the strangeness analysis of pp vs multiplicity at $\sqrt{s} = 13$ TeV [22]. Criteria of the event selection are described as follow.

- Only triggered events with kINT7 trigger were used
- Events classified as incomplete DAQ were rejected
  *fESDEvent->IsIncompleteDAQ()*
- Background events were rejected, based on the standard diagonal cut in the number of tracklets vs clusters, using the function
  *IsSPDClusterVsTrackletBG(fESDEvent)*
  from the AliAnalysisUtils class
- Events with pile-up were rejected using the SPD
  *AliPPVsMultUtils::IsNotPileupSPDInMultBins(fESDEvent)*
  the cut variates with the tracklets multiplicity and is stronger for higher multiplicity events. The cut is looser for low multiplicity events and tighter for high multiplicity events and is based on the number of SPD tracklets. Details in [22].
- For the vertex selection, only events with Z position of the primary vertex inside $\pm$ 10 cm were used, additionally it is required a consistency between the Z positions of the SPD and the tracks vertex of at least 5 mm. It is also required an SPD vertex dispersion less than 0.04 and a resolution better than 2 mm
- Al least one tracklet in $|\eta| < 1.0$ is required in order to select INEL $> 0$ events
  *GetReferenceMultiplicity(ESD,AliESDtrackCuts::kTracklets,1.0)≥ 1*

The number of events that passes each of the event cuts can be seen in figures 3.2 and 3.1 for the $\sqrt{s} = 5.02$ and 13 TeV analyses respectively.

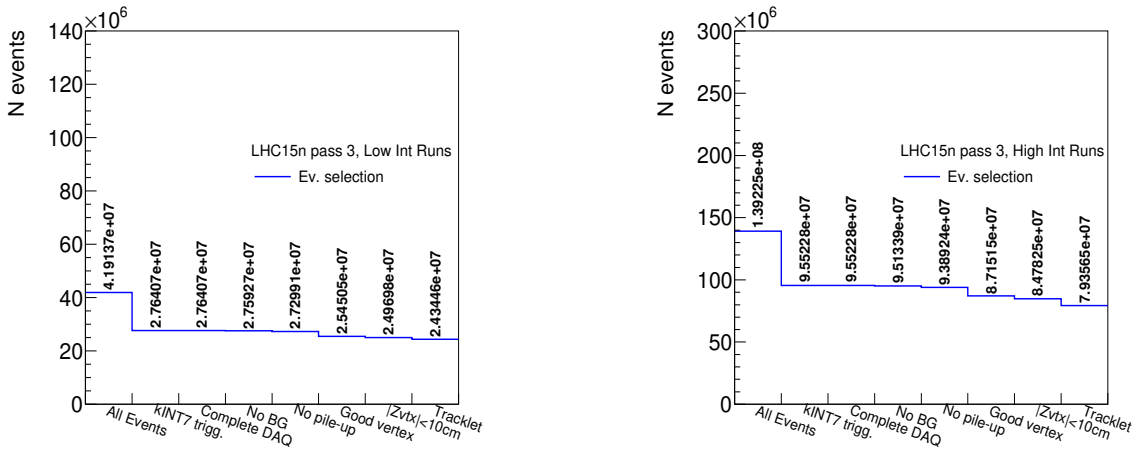


Figure 3.1: Event selection of the data for the $\sqrt{s} = 5.02$ TeV analysis, low (left) and high (right) intensity runs.

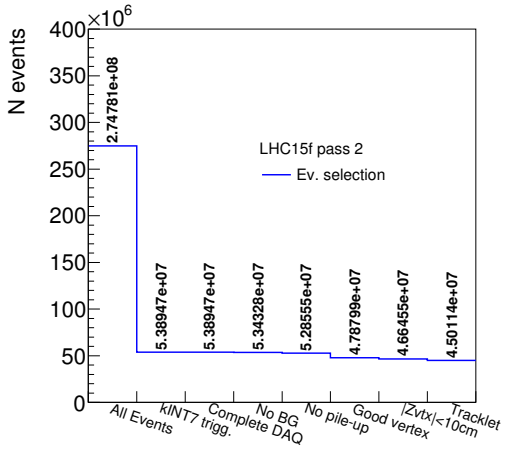


Figure 3.2: Event selection of the data for the $\sqrt{s} = 13$ TeV analysis.

## 3.3 Multiplicity estimators

For the event multiplicity selection we have used two estimators, one in forward rapidity (V0M percentile) and the other in the central barrel (N tracklets in $|\eta| < 0.8$). The performance and a brief explanation of both multiplicity estimators are described as follows. In figures 3.3, 3.4 and 3.5 we show the performance of the multiplicity estimators based on the reconstructed PYTHIA 8 simulations for both energies $\sqrt{s} = 5.02$ and 13 TeV . The same multiplicity binning was used in [19] and [22] for the V0M case.

- N tracklets: This estimator count the number of tracklets in a given pseudo-rapidity window, we choose $|\eta| < 0.8$, the number was extracted using:
  *AliESDtrackCuts::GetReferenceMultiplicity(fESDEvent, AliESDtrackCuts::kTracklets,0.8)*

- V0M percentile: The V0M percentile basically takes the amplitude of both, V0C and V0A, detectors and normalize the area to 100 in order to have percentiles, starting from the highest amplitude in 0% and ends in lowest amplitude with 100%. In this way, 0-1% is a bin with high multiplicity and 70-100% is a bin of low multiplicity events. More information and how to use V0M percentile for Run 2 data can be found in [24]

The binning used for the multiplicity selection can be consulted in table 3.1, it is important to notice that V0M percentiles are represented with roman numbers for an easier notation. The distribution of the tracklets for each of the V0M bins is shown in figures 3.6 and 3.7 for $\sqrt{s} = 5.02$ and 13 TeV analyses respectively. We observe that the V0M estimator for whatever percentile includes a very wide range of tracklets multiplicity.

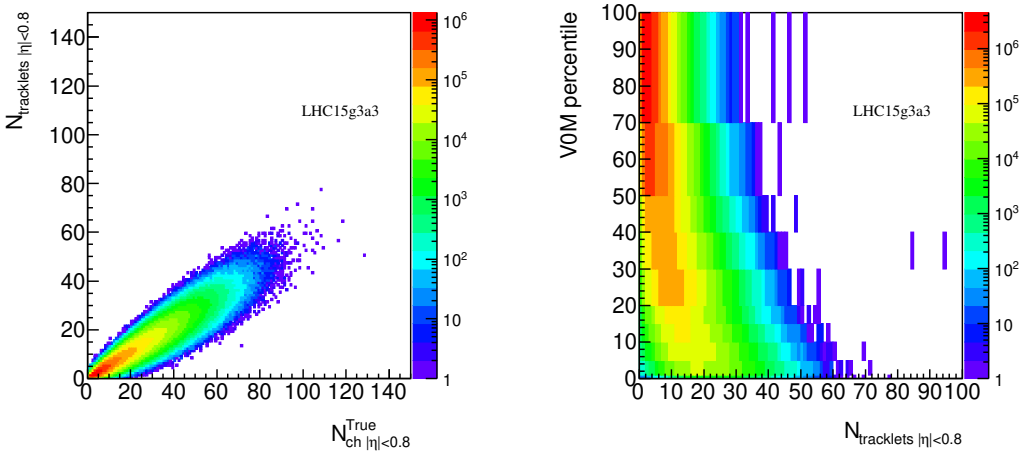


Figure 3.3: Performance of tracklets multiplicity estimator (left) and its correlation with the V0M percentile (right) for the $\sqrt{s} = 13$ TeV analysis.

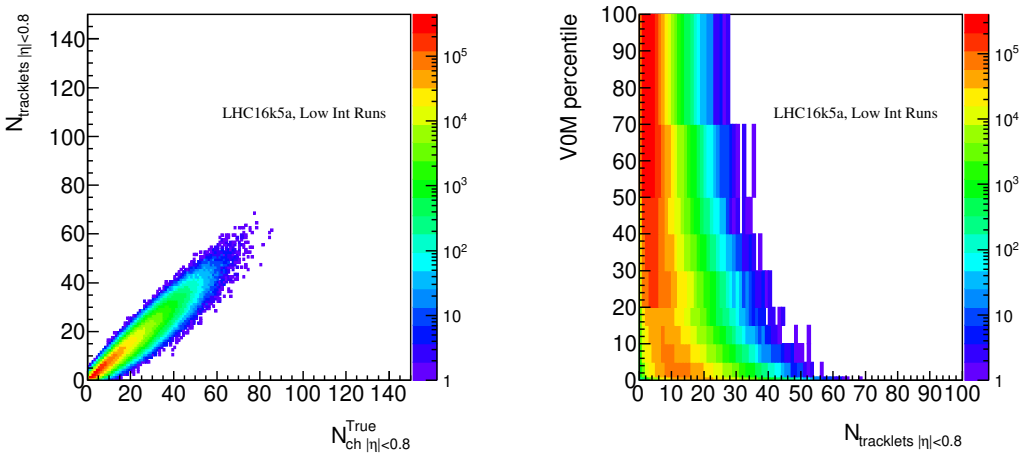


Figure 3.4: Performance of tracklets multiplicity estimator (left) and its correlation with the V0M percentile (right) for the $\sqrt{s} = 5.02$ TeV analysis, for low intensity runs.

| N SPD Tracklets ($\|\eta\| < 0.8$) |
|---|
| 0 to 5 |
| 6 to 10 |
| 11 to 15 |
| 16 to 20 |
| 21 to 25 |
| 26 to 30 |
| 31 to 35 |
| 36 to 40 |
| 41 to 50 |
| $\geq 51$ |

| Label | V0M Percentile |
|---|---|
| X | 70 - 100 % |
| IX | 50 - 70 % |
| VIII | 40 - 50 % |
| VII | 30 - 40 % |
| VI | 20 - 30 % |
| V | 15 - 20 % |
| IV | 10 - 15 % |
| III | 5 - 10 % |
| II | 1 - 5 % |
| I | 0 - 1 % |

Table 3.1: Bins of tracklets multiplicity (left) and V0M percentile (right) used in the present analysis.

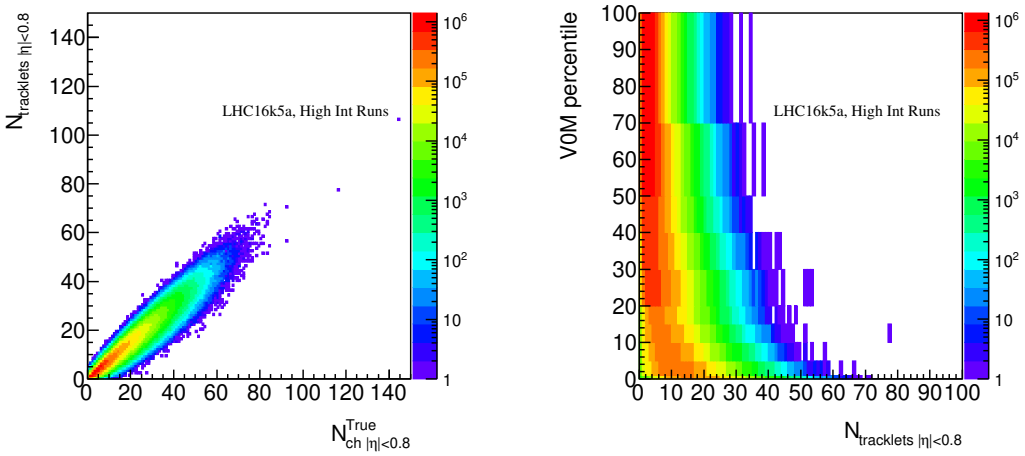


Figure 3.5: Performance of tracklets multiplicity estimator (left) and its correlation with the V0M percentile (right) for the $\sqrt{s} = 5.02$ TeV analysis, for high intensity runs.

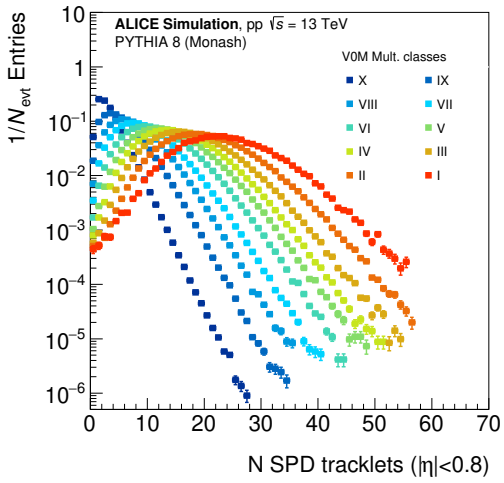


Figure 3.6: Tracklets distribution in function of V0M percentile for the $\sqrt{s} = 13$ TeV analysis.

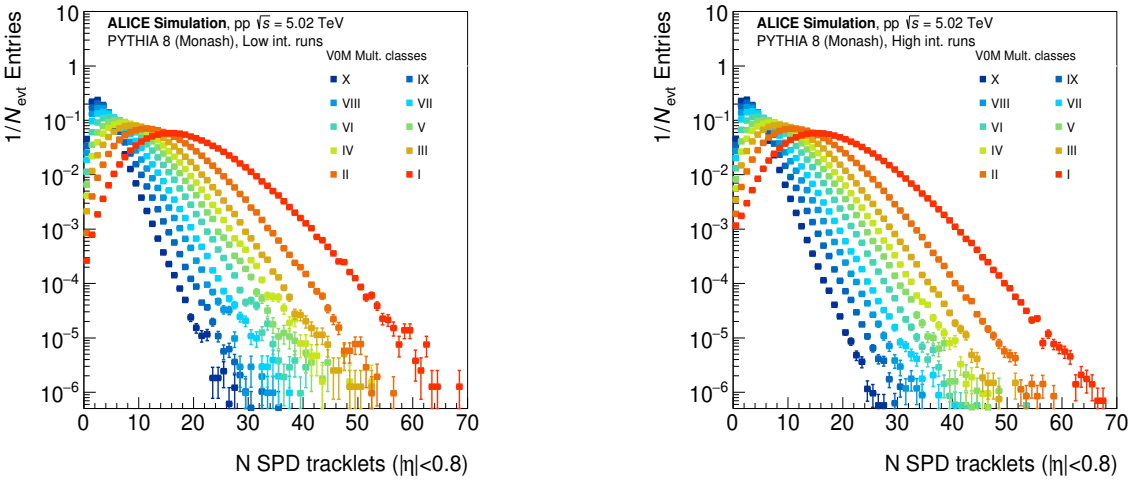


Figure 3.7: Tracklets distribution in function of V0M percentile for the $\sqrt{s} = 5.02$ TeV analysis, for low (left) and high (right) intensity runs.

## 3.4 Track cuts

The purpose of the track cuts is to select only tracks associated to the primary charged particles including decays products, except those that come from weak decays of strange hadrons. The track cuts used for this analysis are very similar to the ones of previous analyses, e.g. [20], but with the difference that the geometric-length cut is applied, the goal of this cut is to remove all the tracks that remain a long time in the TPC dead areas. The main effect of the geometric-length cut is around $p_{\mathrm{T}} \approx 3$ GeV/$c$ and is reflected in the tracking efficiency. All the track cuts are listed in table 3.2. Additionally, kinematic cuts to $\eta$ and $p_{\mathrm{T}}$ were applied:

- $|\eta| < 0.8$ and $p_{\mathrm{T}} > 0.15$ GeV/$c$

| **Track cut (used value)** |
|---|
| *SetRequireTPCRefit(kTRUE)* |
| *SetMinRatioCrossedRowsOverFindableClustersTPC(0.8)* |
| *SetMaxChi2PerClusterTPC(4.0)* |
| *SetMaxFractionSharedTPCClusters(0.4)* |
| *SetRequireITSRefit(kTRUE)* |
| *SetClusterRequerimentITS(AliESDtrackCuts::kSPD,AliESDtrackCuts::kAny)* |
| *SetMaxChi2PerClusterITS(36.0)* |
| *SetDCAToVertex2D(kFALSE)* |
| *SetRequireSigmaToVertex(kFALSE)* |
| *SetMaxDCAToVertexZ(2.0)* |
| *SetAcceptKinkDaughters(kFALSE)* |
| *SetMaxDCAToVertexXYPtDep("7(0.0026 + 0.0050 / $p_{\mathrm{T}}$ ^1.01)")* |
| *SetCutGeoNcrNcl(3.0,130.0,1.5,0.85,0.7)* |

Table 3.2: Table with the track cuts used and their values.

The explanation of each of the parameters of the geometric-length cut can be found in[20], details about the track cuts can be found in [23].

## 3.5 Corrections to raw data

Several corrections were done to the raw data, using the MC reconstructed simulations, in order to remove the detector effects. Basically, the corrections can be divided in two kinds, event-level and track-level. Event-level corrections only affects the normalization of the spectra and the track-level corrections affects also the shape, since they are $p_{\mathrm{T}}$ dependent. In the following sections a detailed description of the corrections is shown. The same procedures (each energy with its own corrections) were applied to both analyses, $\sqrt{s} = 5.02$ and 13 TeV , taking into account that the detector conditions were the same for both periods. All the corrections were computed for all the multiplicity bins with the purpose to check if there are multiplicity dependences for the corrections.

The raw spectra were corrected following equation 3.1

$$\frac{1}{N_{\mathrm{ev}}^{\mathrm{INEL>0}}} \frac{d^2N}{d\eta dp_{\mathrm{T}}} = \frac{(\epsilon^{\mathrm{trigg.\,INEL>0}})(M.V.)}{N_{\mathrm{ev}}^{\mathrm{INEL>0,|Zvtx|<10cm}}} \frac{d^2N^{Raw,|Zvtx|<10cm}}{d\eta dp_{\mathrm{T}}} \frac{(S.L.)(Prim.\,Frac.^{Feed\,down})}{(\epsilon^{\mathrm{tracking}})} \tag{3.1}$$

where $\epsilon^{\mathrm{trigg.\,INEL>0}}$ is the INEL>0 trigger efficiency, $\epsilon^{\mathrm{tracking}}$ is the tracking efficiency, $S.L.$ is the signal loss correction, $Prim.\,Frac.^{Feed\,Down}$ is the fraction of primary particles obtained with the DCAxy template fits technique, finally, $M.V.$ means missing vertex correction.

### 3.5.1 Secondary particles contamination

Although the track cuts remove most of the secondary particles, there is still a fraction of secondaries that remain. The secondary contamination is first computed with the MC (Only to have a first view), but, since the MC does not reproduce it perfectly, it is necessary to use the data in order to obtain a more precise result of the fraction of secondaries. A computation of the secondary particle contamination using only MC in number of tracklets and V0M bins can be seen in figure 3.8 for the $\sqrt{s} = 13$ TeV analysis and in figures 3.9 and 3.10 for the $\sqrt{s} = 5.02$ TeV case, low and high intensity analysis respectively.

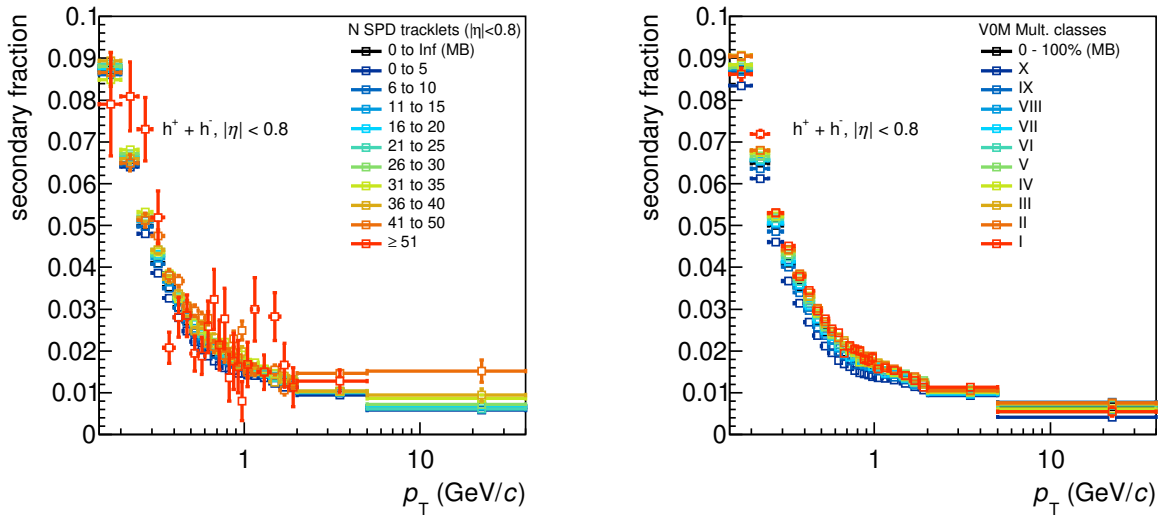


Figure 3.8: Secondary particles contamination for the $\sqrt{s} = 13$ TeV analysis computed with the PYTHIA 8 MC generator. Two multiplicity estimators, tracklets (left) and V0M (right).

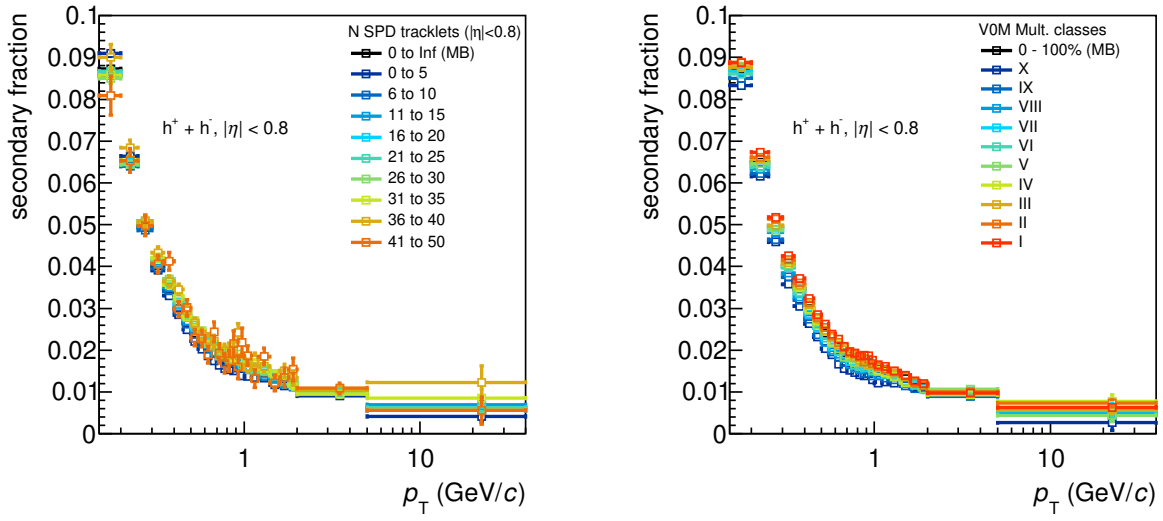


Figure 3.9: Secondary particles contamination for the $\sqrt{s} = 5.02$ TeV analysis, for low intensity runs, computed with the PYTHIA 8 MC generator. Two multiplicity estimators, tracklets (left) and V0M (right).

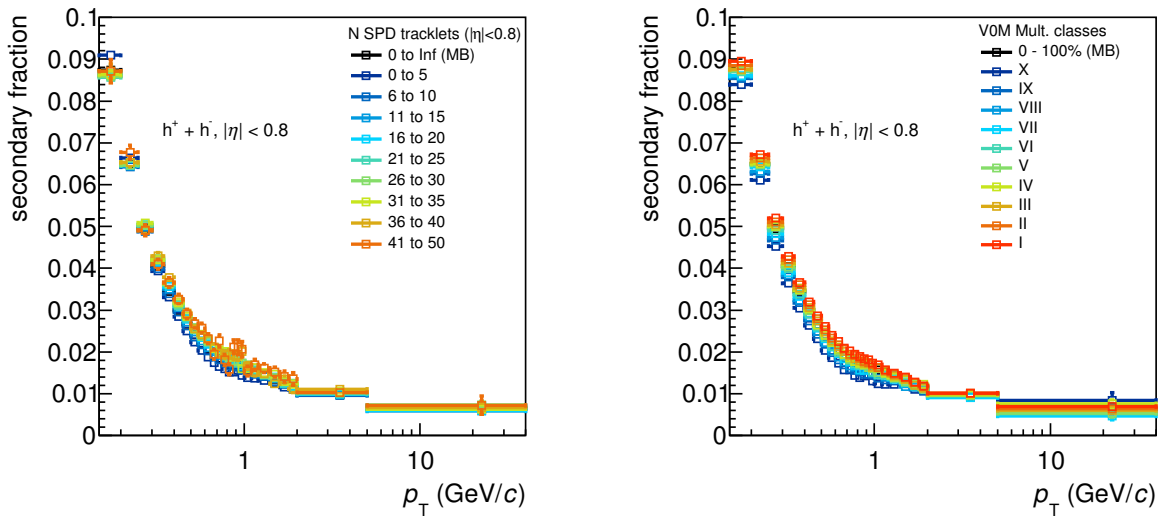


Figure 3.10: Secondary particles contamination for the $\sqrt{s} = 5.02$ TeV analysis, for high intensity runs, computed with the PYTHIA 8 MC generator. Two multiplicity estimators, tracklets (left) and V0M (right).

### DCAxy template fits

The so-called template fits to the DCAxy distribution of the MC simulations to fit the data were used for this correction. The procedure for this correction is as follows. First, it is necessary to open the DCAxy track cut, in data and MC. The track cut that needs to be removed is done by

- *SetMAxDCAToVertexXYPTDep("0.0182+0.035/*$p_{\mathrm{T}}{}^{1.01}$ *")*

With this cut open we allow a lot of secondaries to pass the track selection, this is necessary to execute the method. Once that the DCAxy distributions were obtained for the different contributions in the MC, primaries, secondaries from weak decay and secondaries from material, and for the data, it is necessary to find $\alpha$, $\beta$, and $\gamma$ that satisfy equation 3.2.

$$DCA_{xy}^{Data} = \alpha \cdot DCA_{xy}^{MC\,prim.} + \beta \cdot DCA_{xy}^{MC\,sec.\,matl.} + \gamma \cdot DCA_{xy}^{MC\,sec.\,decs.} \tag{3.2}$$

The constants $\alpha$, $\beta$ and $\gamma$ are the fraction of primaries, secondaries from material interaction and secondaries from weak decays with the DCAxy track cut open. Since this correction is $p_{\mathrm{T}}$ dependent it is necessary to make this procedure in several $p_{\mathrm{T}}$ bins. As an example, the DCAxy distributions from primaries and secondaries obtained from the MC, the data and the template fit can be seen in figure 3.11 for a selected $p_{\mathrm{T}}$ bin in the MB case for the $\sqrt{s} = 13$ TeV analysis. The fits were done in the range (-3,3) cm, it can be observed that the fit is not good in the very far region ( near to $\pm$ 3 cm), it is included into the systematics when we made the fits in a more narrow region, more details in section 9.

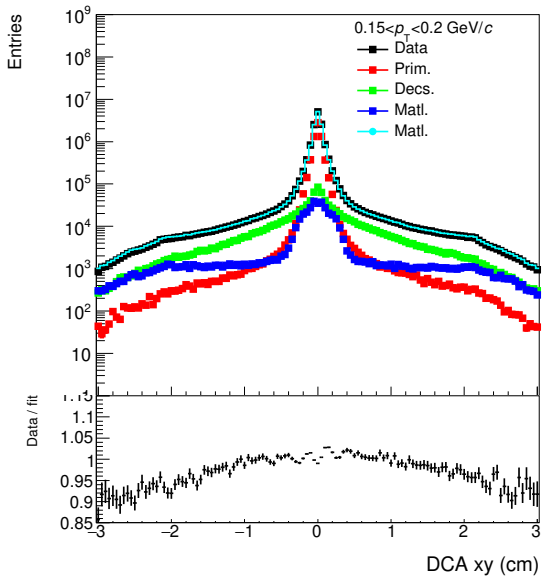


Figure 3.11: DCAxy distribution for one $p_{\mathrm{T}}$ bin used and the template fit to the data for the $\sqrt{s} =$ 13 TeV analysis (top) and the ratio between the data and the fit (bottom).

Since the contribution from material interaction to the secondaries is near zero for $p_{\mathrm{T}}$ higher than 1 GeV/$c$, the template fits were made with two components for the $p_{\mathrm{T}}$ region higher than this value (1 GeV/$c$), it means, secondary particles from material and secondary particles from weak decays were merged into one distribution (component one) and primaries (component two). For the $p_{\mathrm{T}}$ region bellow 1 GeV/$c$ the three-component fits were used, secondaries from weak decays (component one), secondaries from material (component two) and primaries (component three). In figure 3.12 the fractions of primary and secondary particle with the open DCAxy are shown, both multiplicity estimators, for the $\sqrt{s} = 13$ TeV analysis as an example, the same was done for $\sqrt{s} = 5.02$ TeV at low and high intensity runs.

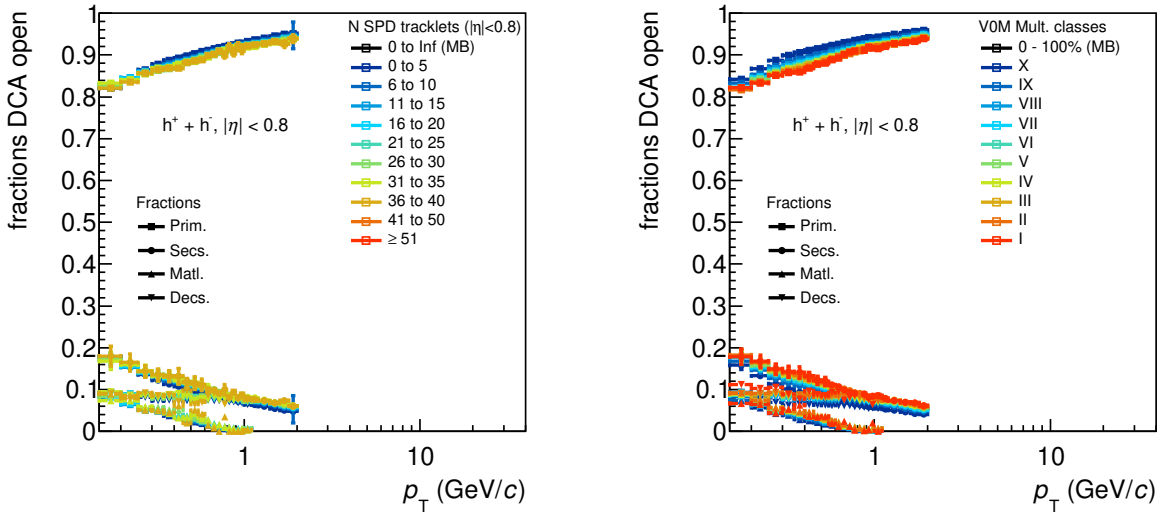


Figure 3.12: Fractions of primary and secondary particles computed with the template fits for the tracklets (left) and the V0M (right), at $\sqrt{s} = 13$ TeV .

The fractions obtained in figure 3.12 were obtained with the DCAxy cut open and considering a DCAxy region from -3 to 3 cm. The contribution in the DCAxy range that the track cuts allows is

needed, for that we follow the re-weight formula shown in equation 3.3

$$F^{i}_{clased\,DCAxy} = \frac{F^{i}_{open\,DCAxy} \cdot \frac{Integral^{i}_{DCAxy\,closed\,range}}{Integral^{i}_{DCAxy\,full\,range}}}{\sum_i \left( F^{i}_{open\,DCAxy} \cdot \frac{Integral^{i}_{DCAxy\,closed\,range}}{Integral^{i}_{DCAxy\,full\,range}} \right)} \tag{3.3}$$

where $i$ runs over all the components of the fits, $F$ is the fractions to that component and $Integral$ is the integral over the DCAxy distributions related to $i$, $full\,range$ means the whole range of the template fits (-3 to 3 cm) and $closed\,range$ limits are computed using the $p_{\mathrm{T}}$ dependent DCAxy cut formula, equation 3.4, with the mean $p_{\mathrm{T}}$ in each of the bins (the center of the bins in this case).

$$DCAxy(p_{\mathrm{T}}) = 0.0182 + \frac{0.0350}{p_{\mathrm{T}}{}^{1.01}} \tag{3.4}$$

Once that the fractions of primaries and secondaries are obtained in the closed range DCAxy, the fraction of primaries (1 - secondaries) can be applied to the raw spectra. To avoid statistical fluctuations, the fraction of secondaries was fitted with $a \cdot b^{c+p_{\mathrm{T}}} + d$, and we use the fit instead of the points, see figures 3.13, 3.14 and 3.15 for details on the secondaries fraction and the fits for $\sqrt{s} = 5.02$ and 13 TeV , low and high intensity runs respectively. It is important to mention that the secondaries do not depends significantly on the quality of the fits, when the primaries are computed, primaries = 1 - secondaries, the quality of the fits does not play a role. For the tracklets case, the last two bins were not computed because of poor statistics.

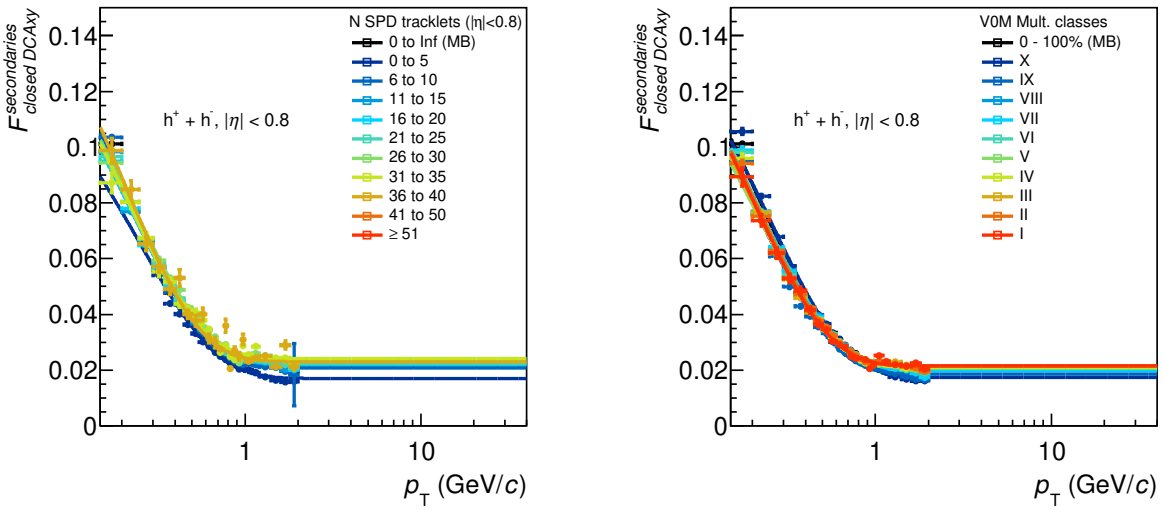


Figure 3.13: Secondary particles fractions, projected to the closed DCAxy region, and the exponential fits for the tracklets (left) and the V0M (right), at $\sqrt{s} = 13$ TeV analysis.

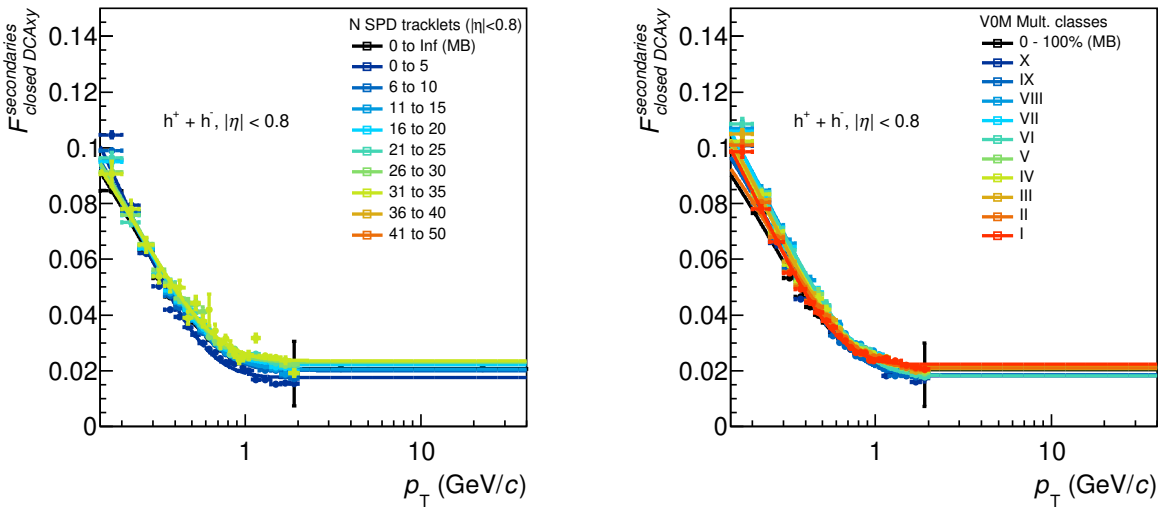


Figure 3.14: Secondary particles fractions, projected to the closed DCAxy region, and the exponential fits for the tracklets (left) and the V0M (right), at $\sqrt{s} = 5.02$ TeV analysis, for low intensity runs.

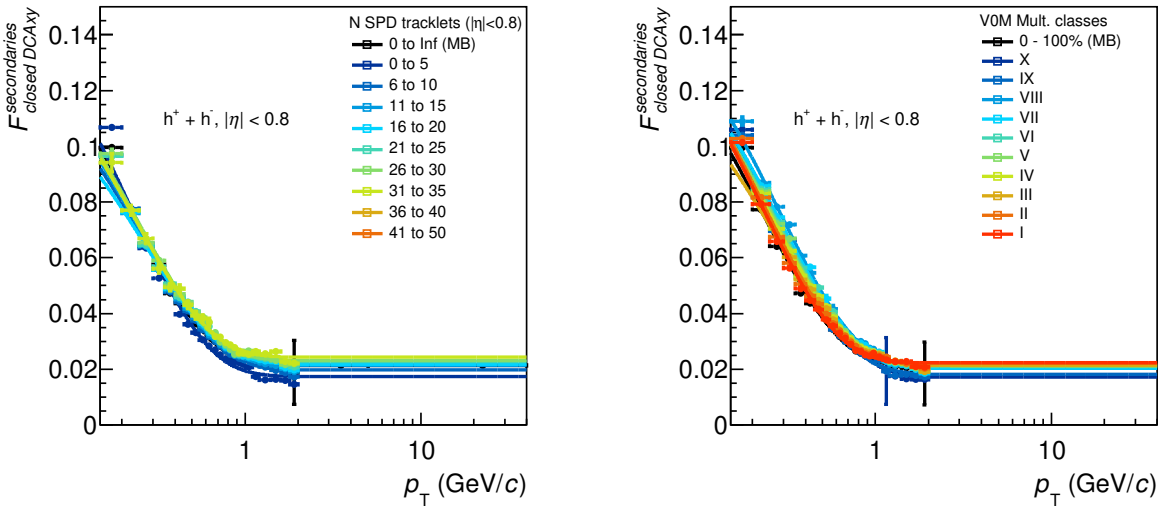


Figure 3.15: Secondary particles fractions, projected to the closed DCAxy region, and the exponential fits for the tracklets (left) and the V0M (right), at $\sqrt{s} = 5.02$ TeV analysis, for high intensity runs.

### 3.5.2 Tracking efficiency

The efficiency is the probability to reconstruct a track in a given $p_{\mathrm{T}}$ interval. Based on the MC simulations of pp collisions using PYTHIA 8 and the modeled response of the detector using GEANT 3, an estimation of the efficiency can be done as follows

$$\epsilon^{tracking} = \frac{(dN/dp_{\mathrm{T}})^{Rec}_{MC}}{(dN/dp_{\mathrm{T}})^{Gen}_{MC}} \tag{3.5}$$

where *Rec* means the reconstructed MC once it is passed through the simulated detector and *Gen* means the generated particles of the simulations. As an example, figure 3.16 shows the tracking efficiency computed with the MC for both multiplicity estimators at $\sqrt{s} = 13$ TeV analysis.

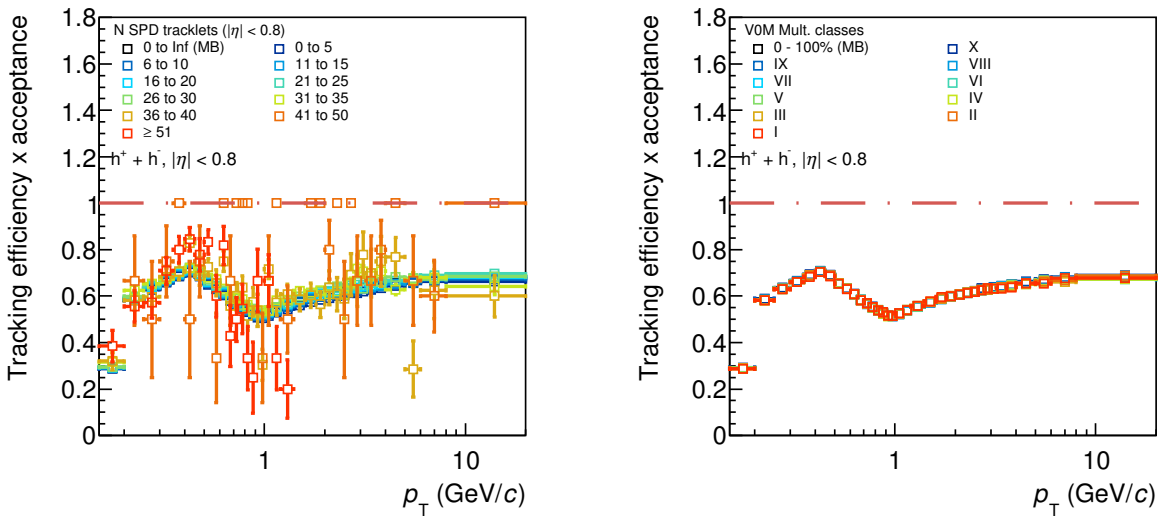


Figure 3.16: Tracking efficiency of charged particles computed with MC (PYTHIA 8) for the tracklets (left) and the V0M (right), $\sqrt{s} = 13$ TeV analysis.

The tracking efficiency of the charged hadrons depends of the chemical composition of the particles produced during the collisions, in other words, not all the particles are reconstructed with the same efficiency. Since MC generator does not reproduce very precisely the real particle composition in data, then an additional procedure is required to correct for this effect.

### Particle composition

The particle composition correction basically is a way to compute the tracking efficiency using the chemical composition measured from experimental data instead of the MC one, which not reproduce the data. The way to estimate the particle composition can be seen in equation 3.6, the reconstructed($Rec$) and generated($Gen$) $p_{\mathrm{T}}$ spectra need to be constructed using the $p_{\mathrm{T}}$ spectra of all the species. The study was done for both energies: $\sqrt{s} = 5.02$ and 13 TeV , only the results for $\sqrt{s} = 13$ TeV analysis are shown in this section since the final results are very similar. The procedure is very similar to the one in [20], with the difference that we use $\Omega^-$ and $\Xi$ from data

$$\epsilon_{part.\,comp.} = \frac{\sum_i \epsilon^i \cdot (dN/dp_{\mathrm{T}})^i + \epsilon^{Rest\,MC} \cdot (dN/dp_{\mathrm{T}})^{Rest\,MC}}{\sum_i (dN/dp_{\mathrm{T}})^i + (dN/dp_{\mathrm{T}})^{Rest\,MC}} \tag{3.6}$$

where $i$ runs over each of the particle species, and $Rest\,MC$ are the rest species that were not measured at the moment and taken from MC (i.e. $e$, $\mu$).

The spectra of $\pi$,k and p have been taken from the identified particle production in function of multiplicity in pp collisions at 7 TeV [25]. While the $\Omega^-$ and $\Xi$ particles were measured by ALICE and taken from the publication [1]. The $\Sigma^+$ and $\Sigma^-$ spectra were estimated using the $\Lambda^0$ spectra taken from [1], similar mass and same strangeness number, following equation 3.7

$$\Sigma^{+,-}_{estimation} = \frac{\Lambda_{Data}}{\Lambda_{MC} \cdot \Sigma^{+,-}_{MC}} \tag{3.7}$$

where $\Sigma^{+,-}$ indicates that the formula was used to estimate $\Sigma^+$ and $\Sigma^-$ particles.

In this approximation, the particles $\Omega^-$, $\Xi$, $\Sigma^+$ and $\Sigma^-$, were taken with efficiency equal to zero since they are not reconstructed for $p_{\mathrm{T}}$ lower than $\approx$ 20GeV/c [20]. The rest of the species like electrons and muons were taken from MC. All the particle species have been measured in a very similar

V0M bins, 7 TeV data were used for the particle composition computation because there are no measurements of identified species in multiplicity bins for $\sqrt{s} = 5.02$ and 13 TeV .

Although the particle composition depends on multiplicity, and hence the efficiency of the inclusive spectra, the efficiency for each species does not depend on the multiplicity as can be observed in figure 3.17.

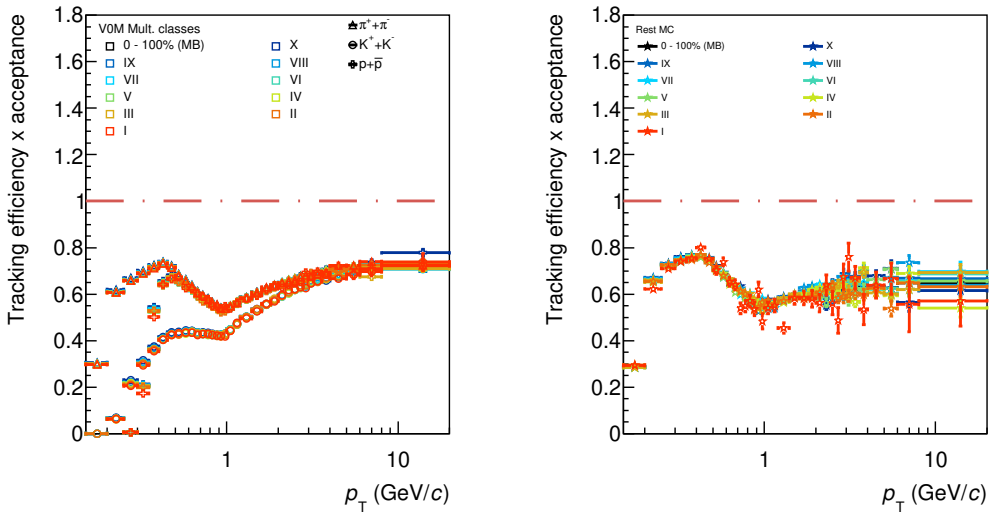


Figure 3.17: Tracking efficiency in V0M bins for $\pi$, k and p (left) and for the rest of the particles (right), at $\sqrt{s} = 13$ TeV .

Another fact that needs attention is that the identified particles spectra that were used to compute the particle composition correction have been measured in rapidity, it is necessary to convert it to pseudo-rapidity. An approximation to $\Delta y/\Delta\eta$ is:

$$\frac{\Delta y}{\Delta \eta} = \frac{y_{max} - y_{min}}{\eta(y_{max}, p_{\mathrm{T}}, m) - \eta(y_{mim}, p_{\mathrm{T}}, m)} \tag{3.8}$$

where the function $\eta(y_{mim}, p_{\mathrm{T}}, m)$ is given by equation 3.9, $y_{max,min}$ were chosen to be 0.5,-0.5 based on MC studies.

$$\eta = \frac{1}{2} \ln \frac{\sqrt{m_{\mathrm{T}}^2 \cosh^2(\mathrm{y}) - \mathrm{m}^2} + m_{\mathrm{T}} \sinh(\mathrm{y})}{\sqrt{m_{\mathrm{T}}^2 \cosh^2(\mathrm{y}) - \mathrm{m}^2} - m_{\mathrm{T}} \sinh(\mathrm{y})} \tag{3.9}$$

Since the measurements do not cover the whole $p_{\mathrm{T}}$ range, a Levy-Tsallis fit has been applied to each of the identified particle spectra to extrapolate to the unmeasured regions of $p_{\mathrm{T}}$ . For $\Xi$, $\Omega^-$ and $\Lambda^0$, that have a wider binning than the other species, we use the fit values in the whole $p_{\mathrm{T}}$ range in order to have the same binning.

The particle composition efficiency for the MB case and its comparison with the efficiency obtained purely from MC can be seen in figure 3.18 for $\sqrt{s} = 13$ TeV . In figure 3.19, the particle composition in function of the V0M and its comparison with the MB case are shown.

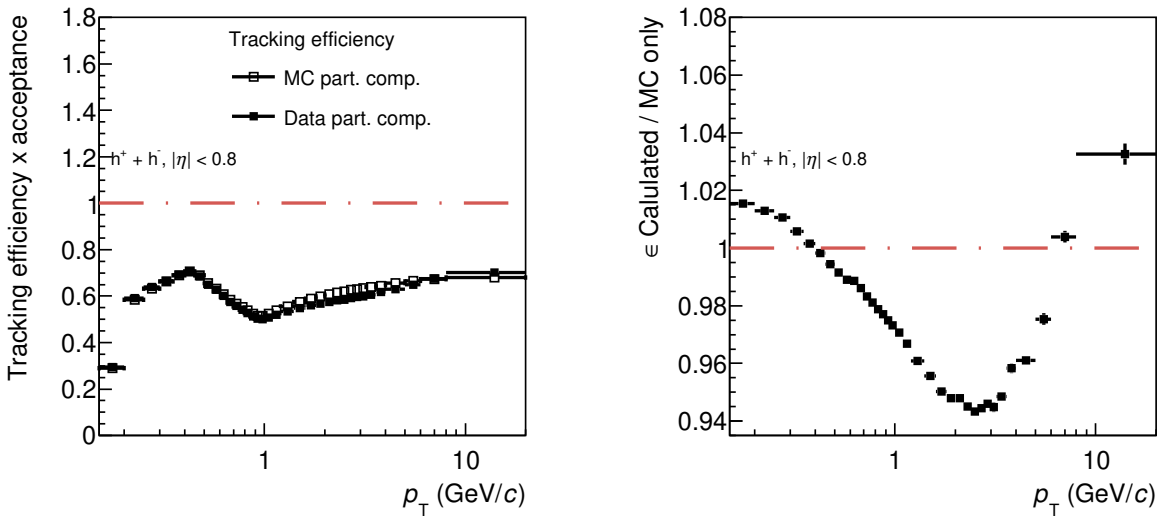


Figure 3.18: Tracking efficiency with real particle composition, and computed with MC (left) and the ratio between the two calculations (right) for the M.B. case, at $\sqrt{s} = 13$ TeV .

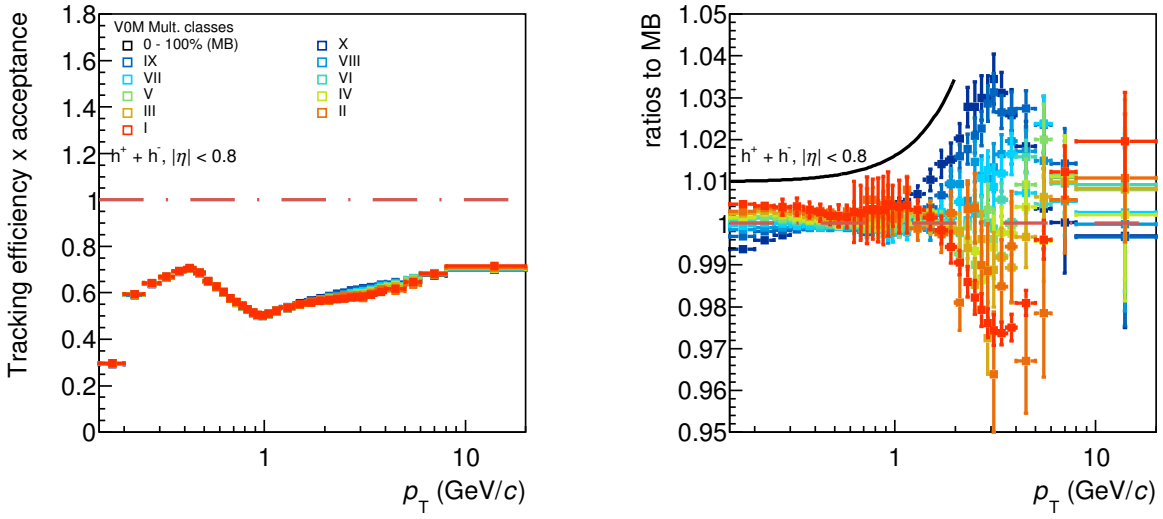


Figure 3.19: Tracking efficiency with real particle composition in V0M bins (left) the ratios to MB (right), at $\sqrt{s} = 13$ TeV .

In order to avoid statistical fluctuations, and taking into account that the $\langle dN_{ch}/d\eta \rangle$ of the V0M bins is different for $\sqrt{s} = 5.02$ TeV and $\sqrt{s} = 13$ TeV , i.e. the same percentile does not represent same multiplicity in the central barrel for different energies, we have used the MB efficiency to correct all the spectra. Another point is that we assign a systematic based on the right side of the figure 3.19.

### 3.5.3 Signal loss

Signal is missing due the event cuts, then we need to correct our signal that passes all the event cuts. This correction compensates the loss of signal due the event selection. Since our measurements and the corrections to the signal by efficiency and secondaries are computed in the class of events that

have a reconstructed vertex with a z values inside ± 10 cm. The signal loss is calculated as follows.

$$S.L. = \frac{(dN/dp_{\mathrm{T}})^{\text{All the event selection}}_{Gen}}{(dN/dp_{\mathrm{T}})^{\text{True INEL>0 ,|Z}_{\text{true-vtx}}\text{|<10cm}}_{Gen}} \tag{3.10}$$

Since the signal loss is purely MC driven, it is computed using PYTHIA 6 and PYTHIA 8, the average between the two models was used to correct the data. The signal loss, computed with PYTHIA 6, for the $\sqrt{s} = 13$ TeV case can be seen in figure 3.20, for the $\sqrt{s} = 5.02$ TeV data see figures 3.21 and 3.21, for low and high intensity runs respectively.

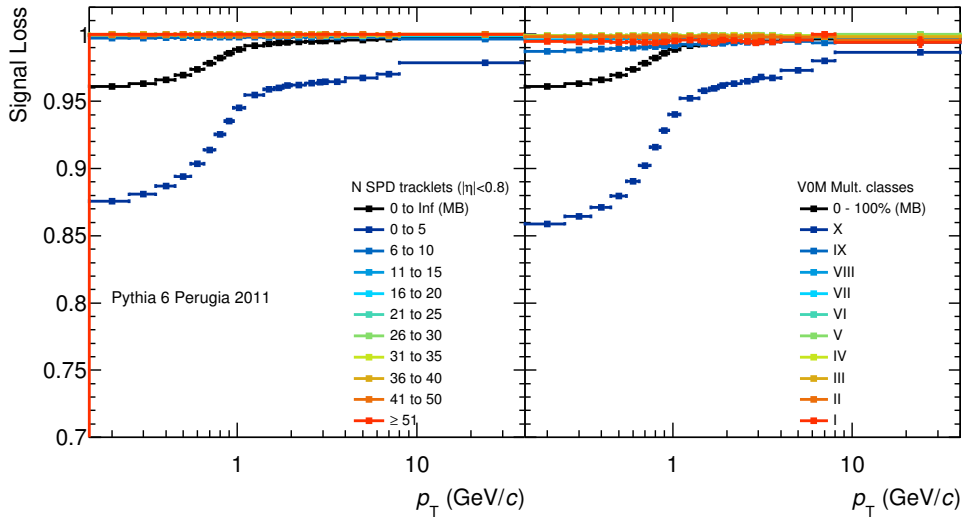


Figure 3.20: Signal loss correction in tracklets (left) and V0M (right) multiplicity bins, at $\sqrt{s} = 13$ TeV MC simulations using PYTHIA 6.

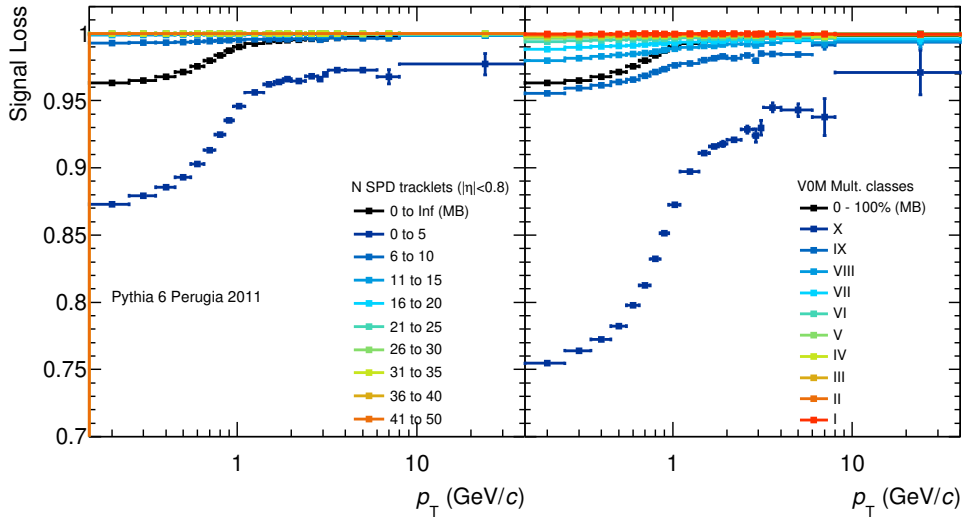


Figure 3.21: Signal loss correction in tracklets (left) and V0M (right) multiplicity bins, for low intensity runs at $\sqrt{s} = 5.02$ TeV MC simulations using PYTHIA 6.

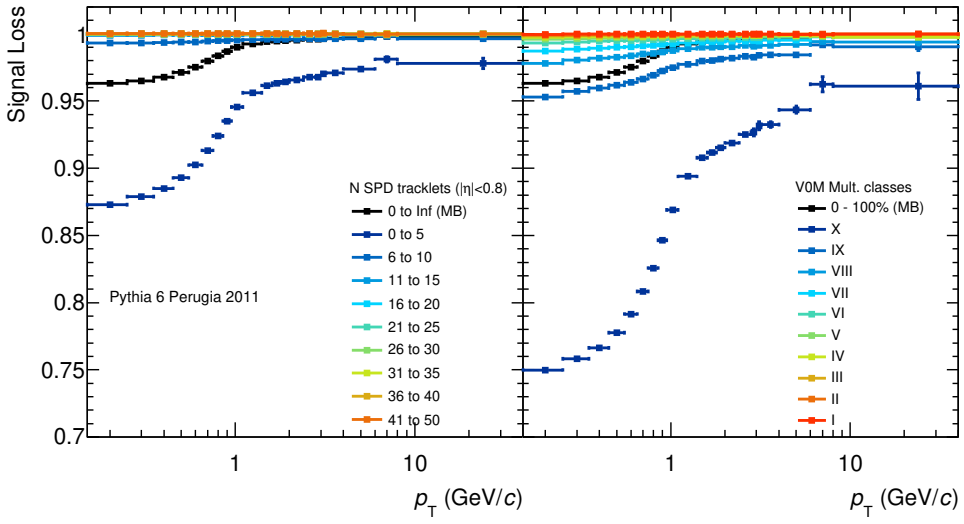


Figure 3.22: Signal loss correction in tracklets (left) and V0M (right) multiplicity bins, for high intensity runs at $\sqrt{s} = 5.02$ TeV MC simulations using PYTHIA 6.

Signal loss computed with PYTHIA 8 can be observed in figures 3.23, 3.24 and 3.25.

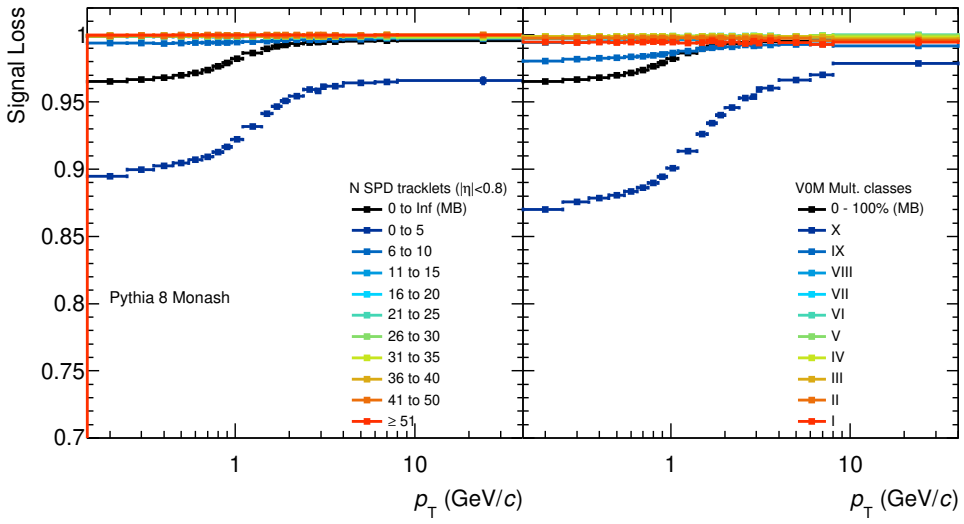


Figure 3.23: Signal loss correction in tracklets (left) and V0M (right) multiplicity bins, at $\sqrt{s} =$ 13 TeV MC simulations using PYTHIA 8

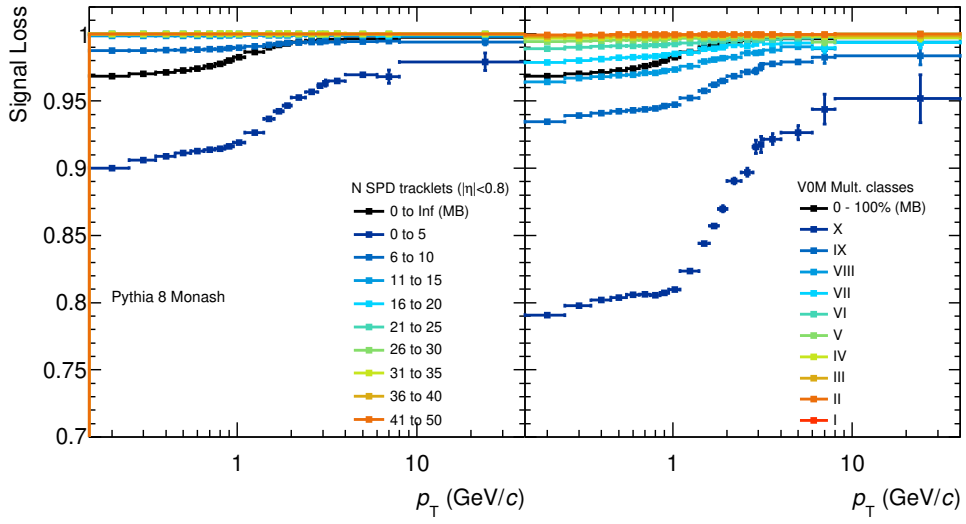


Figure 3.24: Signal loss correction in tracklets (left) and V0M (right) multiplicity bins, for low intensity runs at $\sqrt{s} = 5.02$ TeV MC simulations using PYTHIA 8.

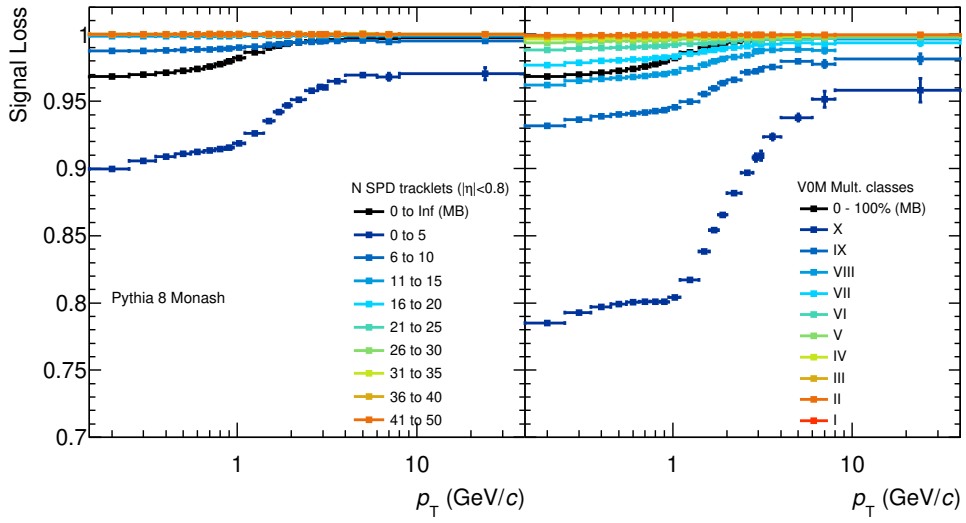


Figure 3.25: Signal loss correction in tracklets (left) and V0M (right) multiplicity bins, for high intensity runs at $\sqrt{s} = 5.02$ TeV MC simulations using PYTHIA 8.

At the end, the average signal loss between the two models can be observed in figures 3.26, 3.27 and 3.28. It is important to remember than average was used to correct the raw data.

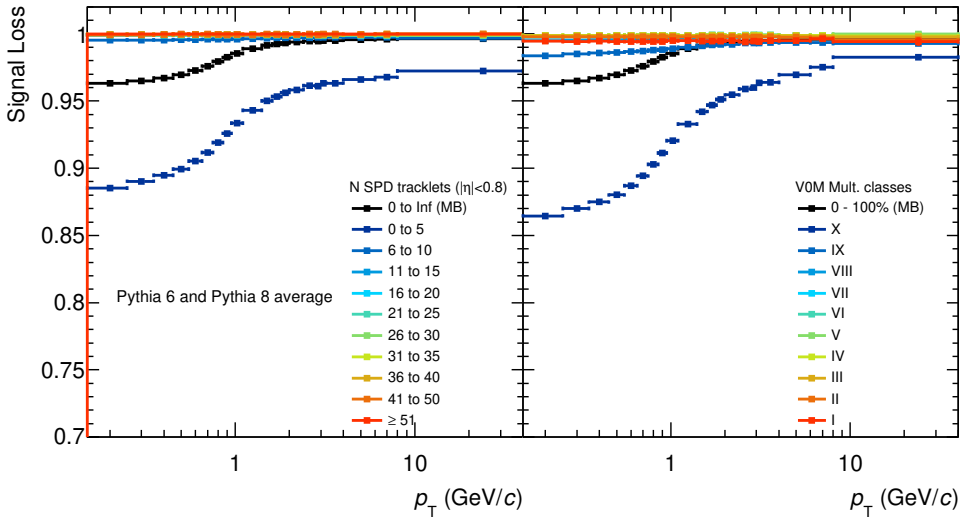


Figure 3.26: Signal loss correction in tracklets (left) and V0M (right) bins, at $\sqrt{s} = 13$ TeV MC simulations using PYTHIA 6 and PYTHIA 8 average.

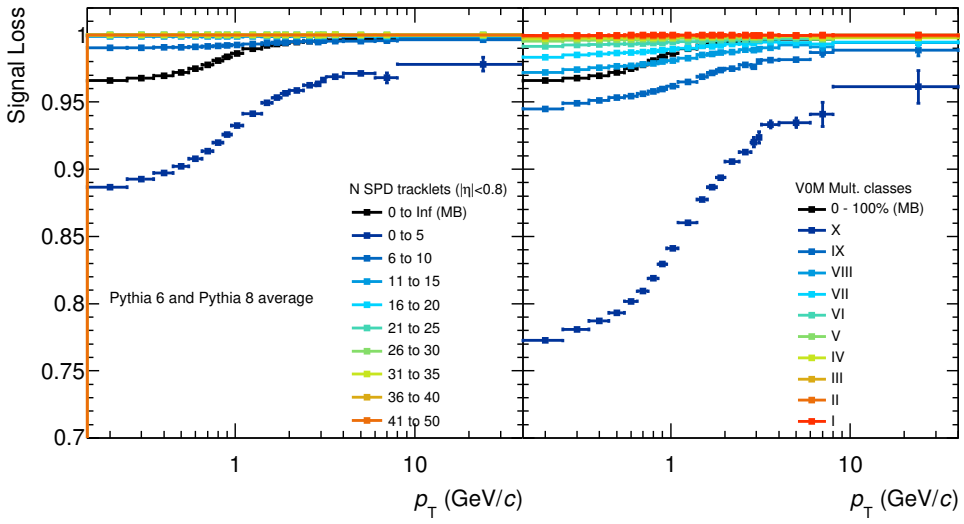


Figure 3.27: Signal loss correction in tracklets (left) and V0M (right) bins, at$\sqrt{s} = 5.02$ TeV MC simulations using PYTHIA 6 and PYTHIA 8 average, for low intensity runs.

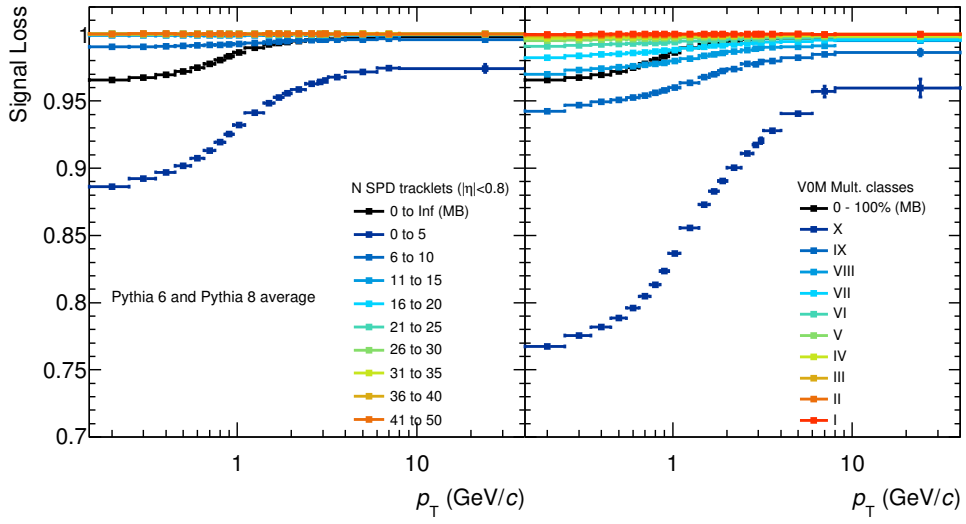


Figure 3.28: Signal loss correction in tracklets (left) and V0M (right) bins, at $\sqrt{s} = 5.02$ TeV MC simulations using PYTHIA 6 and PYTHIA 8 average, for high intensity runs.

## 3.6 Normalization

After our event selection, the spectra are normalized to the number of events that passes all the events cuts. There are some INEL>0 events that did not pass the Physics Selection (trigger efficiency) or were rejected because they did not have a good vertex (missing vertex correction). We follow the recipe stated in [29], strategy 2 with a small change to adapt it to INEL>0.

The missing vertex correction ($M.V.$) is computed with the data following the equation 3.11

$$M.V. = \frac{N_{ev}^{good\,vertex}}{N_{ev}^{P.S.}} \tag{3.11}$$

where $N_{ev}^{P.S.}$ is the number of events that passed the physics selection (kINT7 + 1 Tracklet $|\eta| < 1$ + NoIncDAQ + NoPileup + NoBG) and $N_{ev}^{good\,vertex}$ is the number of events that passed the physics selections and have a good vertex (existing tracks vertex + existing SPD vertex + consistency between z position of the tracks and the SPD vertex ). The missing vertex correction in function of multiplicity can be seen in figures 3.31, 3.29 and 3.30 for the $\sqrt{s} = 5.02$ and 13 TeV , for low and high intensity runs analyses.

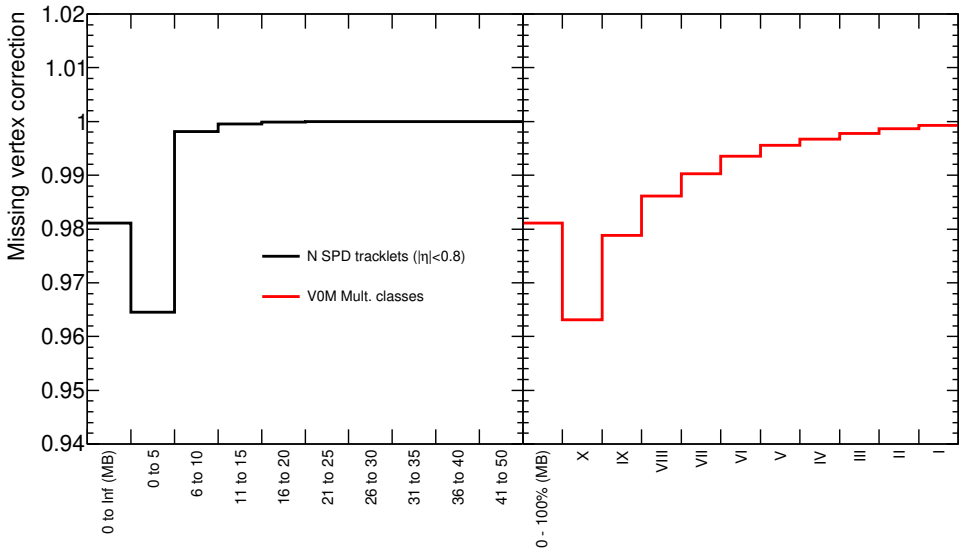


Figure 3.29: Missing vertex correction in function of tracklets (left) and V0M (right), for low intensity runs at $\sqrt{s} = 5.02$ TeV analysis.

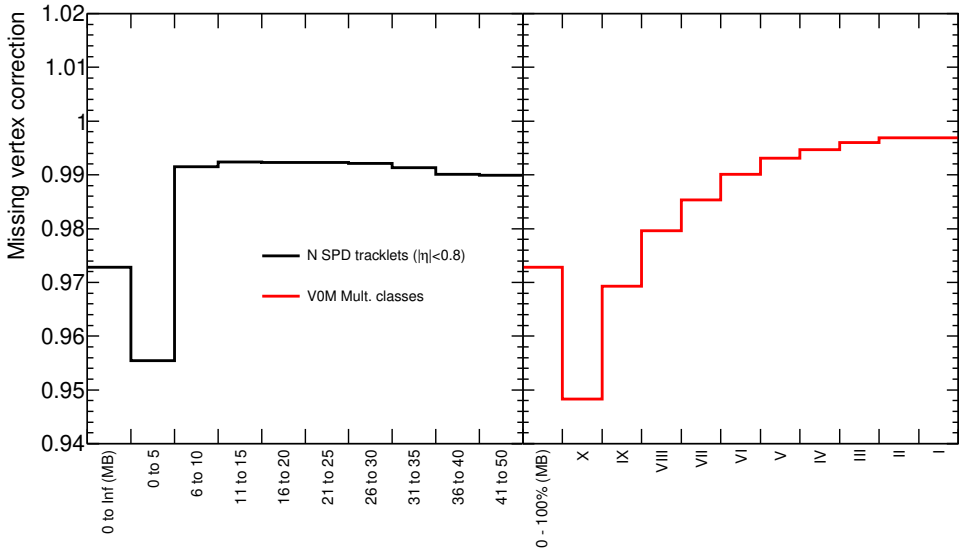


Figure 3.30: Missing vertex correction in function of tracklets (left) and V0M (right), for high intensity runs at $\sqrt{s} = 5.02$ TeV analysis.

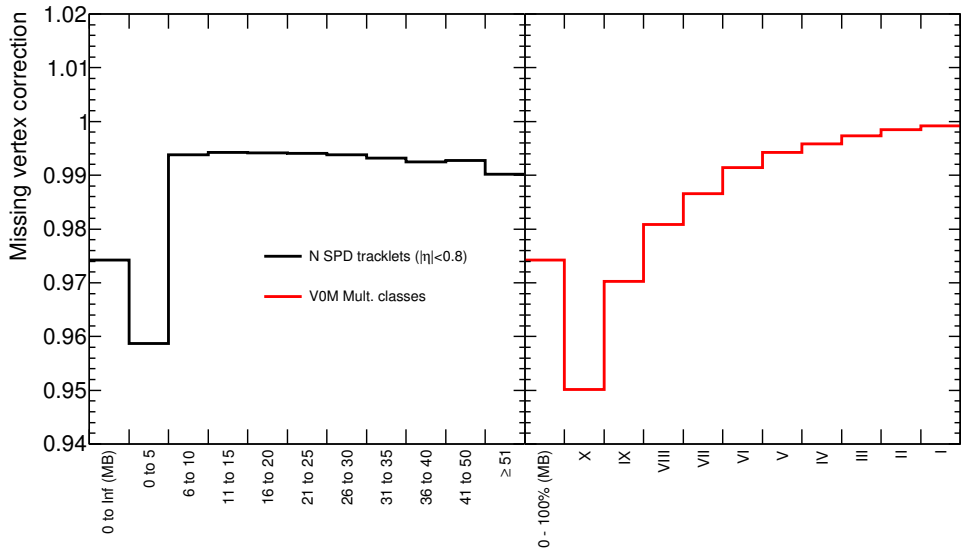


Figure 3.31: Missing vertex correction in function of tracklets (left) and V0M (right), at $\sqrt{s}$ = 13 TeV analysis.

The trigger efficiency was computed using PYTHIA 6 and the differences with PYTHIA 8 were assigned as a systematic error to the normalization. The way in which we compute the trigger efficiency can be seen in equation 3.12. The trigger efficiency can be consulted in figures 3.32, 3.33 and 3.34 for the $\sqrt{s} = 5.02$ and 13 TeV , for low and high intensity runs.

$$\epsilon^{trigg.\,INEL>0} = \frac{N_{ev}^{P.S.}}{N_{ev}^{(\text{True INEL}>0)}} \tag{3.12}$$

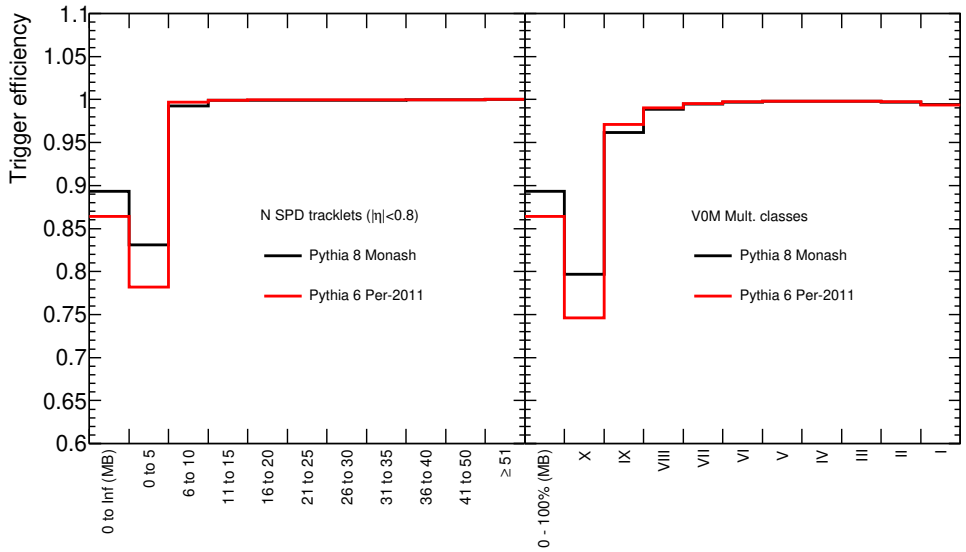


Figure 3.32: Trigger efficiency in function of tracklets (left) and V0M (right), at $\sqrt{s} = 13$ TeV .

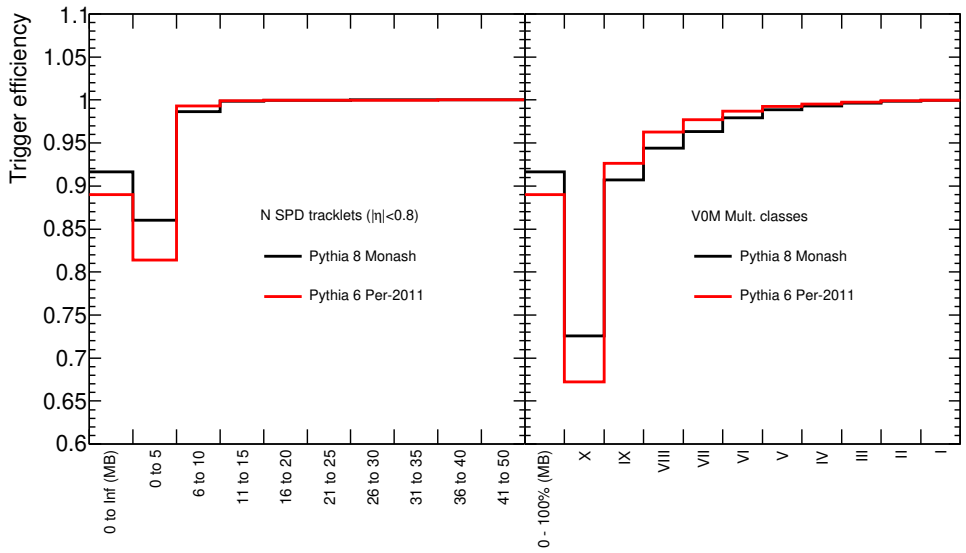


Figure 3.33: Trigger efficiency in function of tracklets (left) and V0M (right), for low intensity runs at $\sqrt{s} = 5.02$ TeV data.

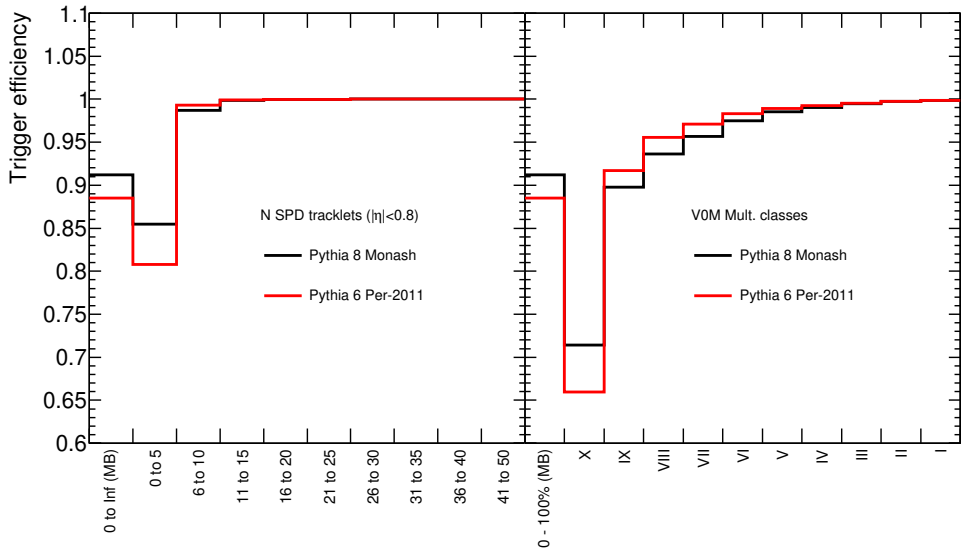


Figure 3.34: Trigger efficiency in function of tracklets (left) and V0M (right), for high intensity runs at $\sqrt{s} = 5.02$ TeV data.

## 3.7 Systematic uncertainties

The contributions to the systematic uncertainties that have been considered in this analysis are summarized in table 3.3. The uncertainties that correspond to matching efficiency, $p_{\mathrm{T}}$ resolution, and material budget were obtain from the GSI group and taking as a common systematic for all multiplicity bins.

| **Systematic unc. contribution** |
|---|
| Track cuts |
| Pile-up |
| Feed Down and secondaries |
| Efficiency and particle comp. |
| $Z_{vtx}$ selection |
| Matching efficiency |
| $p_{\mathrm{T}}$ resolution |
| Material budget |
| Signal loss |
| Trigger efficiency |

Table 3.3: List of the contributions to the systematic uncertainties taken into account for this analysis.

### 3.7.1 Track cuts

The parameters of the track cuts have been varied, one by one, up and down, taking into account the limits used in [20]. The variations were applied in the same way to the MC and the data. The higher variation for each $p_{\mathrm{T}}$ bin, up or down, was taken as the uncertainly for the given cut. The total contribution of the track cuts to the systematic errors was considered as the square root of the sum in quadrature of all the cuts contributions. In table 3.4, the variations made to each of the track-cuts are shown.

| **Track cut (nominal value)** | **Variation (up - down)** |
|---|---|
| *SetMinRatioCrossedRowsOverFindableClustersTPC(0.8)* | 0.7-0.9 |
| *SetMaxChi2PerClusterTPC(4.0)* | 3.0-5.0 |
| *SetMaxFractionSharedTPCClusters(0.4)* | 0.2-1.0 |
| *SetClusterRequerimentITS(AliESDtrackCuts::kSPD, AliESDtrackCuts::kAny)* | used-not used |
| *SetMaxChi2PerClusterITS(36.0)* | 25.0-49.0 |
| *SetMaxDCAToVertexZ(2.0)* | 1.0-5.0 |
| *SetMaxDCAToVertexXYPtDep(7f($p_{\mathrm{T}}$ ))* | 4f($p_{\mathrm{T}}$ )-10f($p_{\mathrm{T}}$ ) |
| *SetCutGeoNcrNcl(3.0,130.0,...)* | (2.0-4.0,120.0-140.0,...) |

Table 3.4: Track cuts, nominal values and variations applied to compute the systematics, $f(p_{\mathrm{T}}) = 0.0026 + 0.0050/p_{\mathrm{T}}{}^{1.01}$. Only the first two parameters of the track cuts were variated, variation of the other parameters were negligible [20].

The total systematic related to the track cuts and each of the contributions can be seen in figure 3.35 as an example for INEL $> 0$. at $\sqrt{s} = 13$ TeV . The total track cuts systematics for MB and for each of the multiplicity bins can be observed in figure 3.36 for the $\sqrt{s} = 13$ TeV data and in figures 3.37 and 3.37 for the $\sqrt{s} = 5.02$ TeV data, for low and high intensity runs respectively.

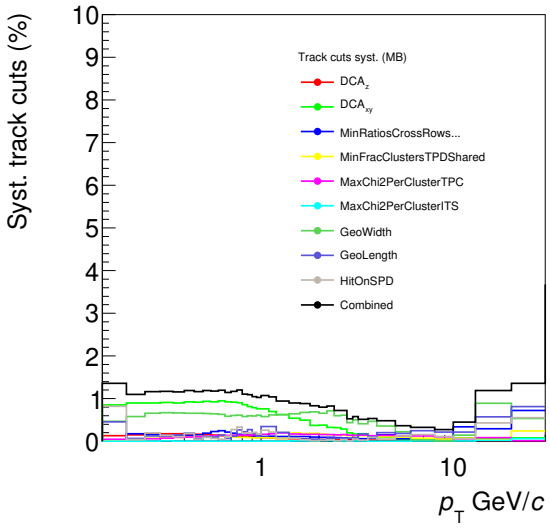


Figure 3.35: Total track systematic error and all the contributions for INEL $> 0.$, at $\sqrt{s} = 13$ TeV .

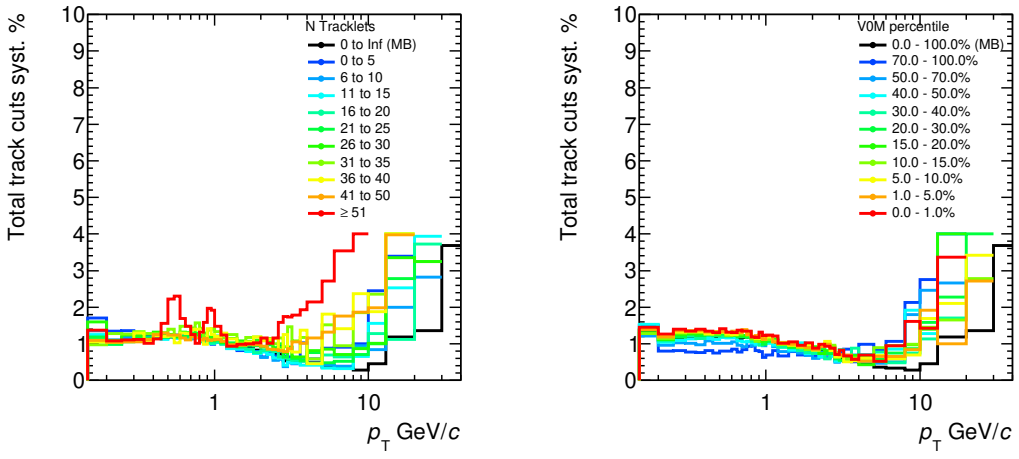


Figure 3.36: Total track systematic errors in function of tracklets (left) and V0M (right) multiplicity bins, at $\sqrt{s} = 13$ TeV .

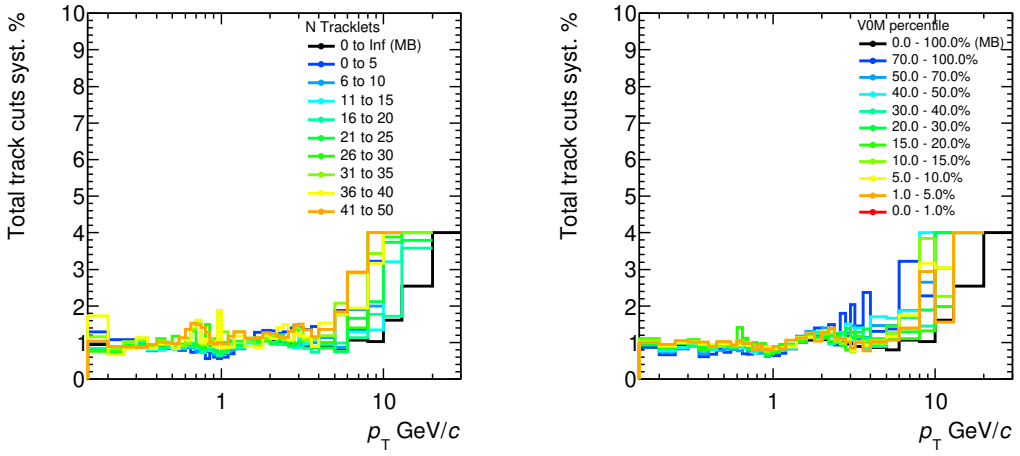


Figure 3.37: Total track systematic errors in function of tracklets (left) and V0M (right) multiplicity bins, for low intensity runs at $\sqrt{s} = 5.02$ TeV .

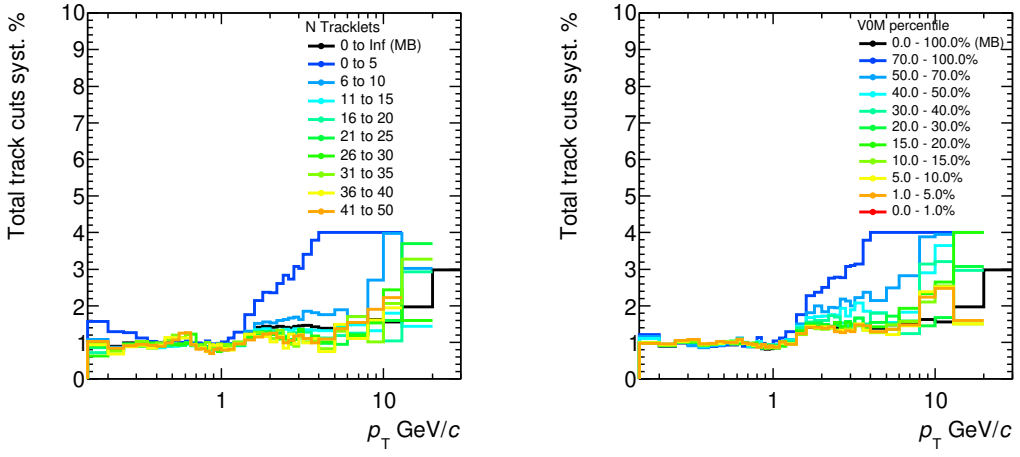


Figure 3.38: Total track systematic errors in function of tracklets (left) and V0M (right) multiplicity bins, for high intensity runs at $\sqrt{s} = 5.02$ TeV .

### 3.7.2 Pile-up rejection

The systematic error related to the pile-up rejection was computed in a similar way as in [22]. If we observe the run condition table, the parameter $\mu$ indicates the probability of interaction per bunch-crossing, in runs with high $\mu$, it is more probable to find pile-up. The ratio between runs with high and low $\mu$ was assigned as the pile-up systematic error. Since in the $\sqrt{s} = 5.02$ TeV data, the highest $\mu$ values are below 5%, the study was done with the $\sqrt{s} = 13$ TeV data. The $\mu$ of the runs for the $\sqrt{s} = 13$ TeV data can be seen in figure 3.39.

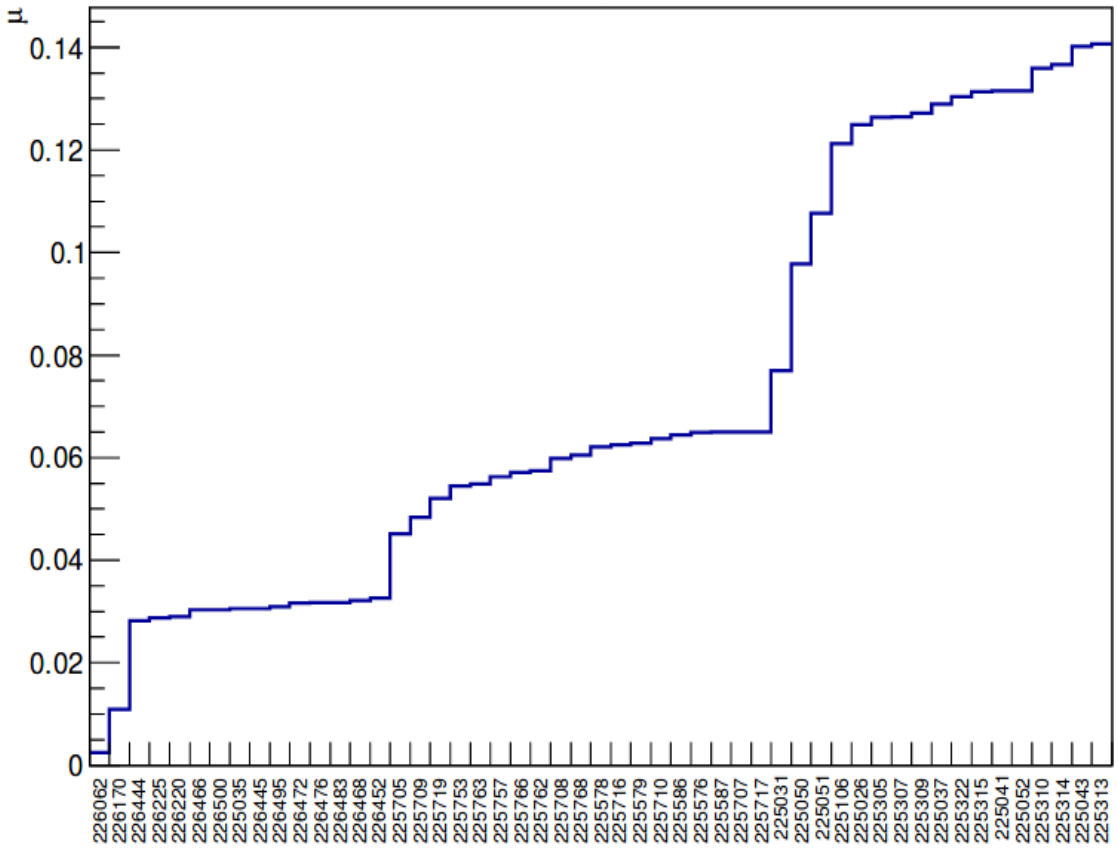


Figure 3.39: Probability of interaction per bunch-crossing ($\mu$) per run at $\sqrt{s} = 13$ TeV data.

From figure 3.39, we decide to use a value of $\mu = 0.07$ to separate into high and low $\mu$ runs. To avoid statistical fluctuations we separate the sample in three multiplicity bins and MB. In figure 3.40 the ratios between high and low $\mu$ and the considered systematic errors can be seen.

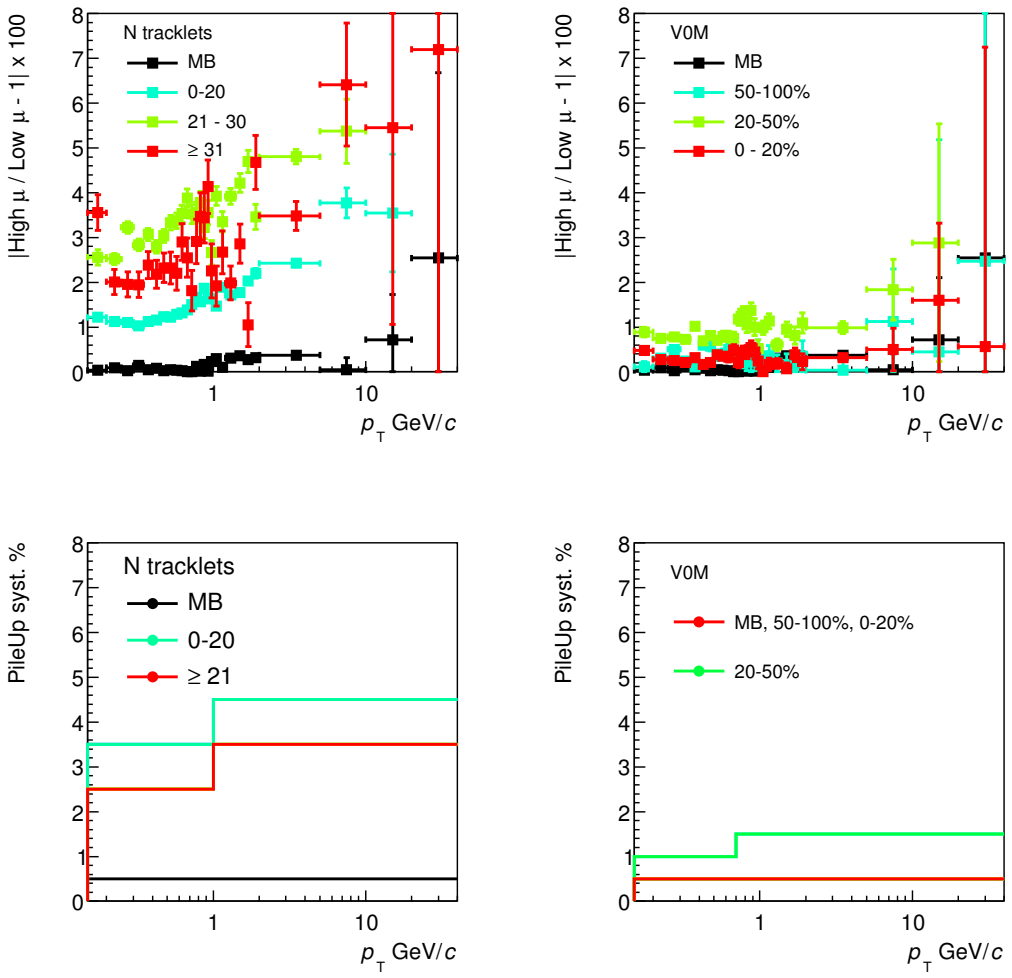


Figure 3.40: Ratios between high and low $\mu$ runs for the tracklets (top left) and V0M (top right) considered bins. Systematic error considered for tracklets (bottom left) and V0M (bottom right), at $\sqrt{s} = 13$ TeV data.

### 3.7.3 Secondaries and feed down

The template fits were not perfect in the very far DCAxy region (near $\pm$ 3 cm). In order to cover this issue we made the fits considering a smaller region (-1.5,1.5) cm. Due to statistics we only compute this systematic error for the INEL $> 0$. case and assign it as a common error for all the multiplicity bins. Taking into account that this systematic error does not change significantly with centrality for pions in Pb-Pb collisions, we conclude that we are safe using the INEL $> 0$. result. The total systematics related to the feed down can be seen in figure 3.41 for the $\sqrt{s} = 13$ TeV analysis. Similar results were obtained for $\sqrt{s} = 5.02$ TeV analysis.

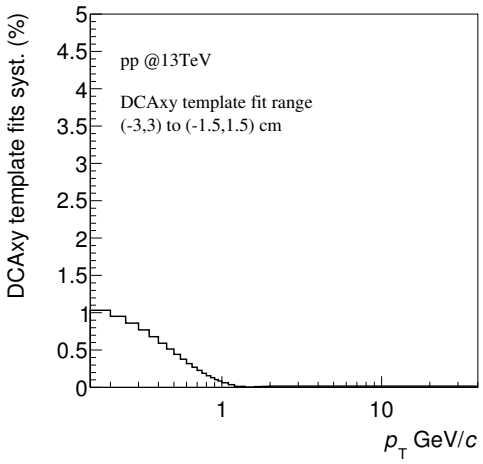


Figure 3.41: Feed down systematic error for pp at $\sqrt{s} = 13$ TeV data.

As explained in section 7, the contamination from secondaries was computed for INEL $> 0$ and was used to correct all the multiplicity bins $p_{\mathrm{T}}$ spectra. A systematic error was assigned to each multiplicity bin taking into account the ratio of the primary particles in each multiplicity bin and the MB case. In figure 3.42, the multiplicity dependence of the primary fractions for the $\sqrt{s} = 13$ TeV analysis is shown, similar results obtained for the $\sqrt{s} = 5.02$ TeV analysis, based on this result 1% was considered for all the multiplicity bins.

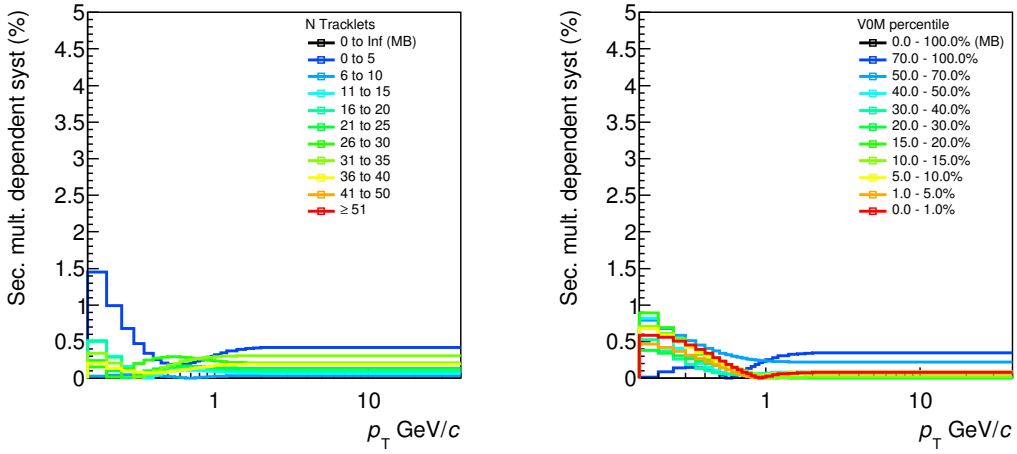


Figure 3.42: Systematic errors from secondaries in Tracklets (left) and V0M (right) multiplicity bins for the $\sqrt{s} = 13$ TeV data.

### 3.7.4 Efficiency and particle composition

The particle composition systematic error was computed for the INEL $> 0$ and taken as a common error for all the multiplicity bins. To compute this uncertainty we scale each of species used in the particle composition up and down. The scaling factors were taken as the highest systematic percentage values computed in the whole spectrum for each of the species. The rest of the particles (the ones that are not measured and were taken from MC) were variated 30%, $\Sigma^+$ and $\Sigma^-$ (estimated using $\Lambda^0$, see section 7) were variate the high syst. error of the $\Lambda^0$ measurement and was increased 100% as a first estimation, the result is very similar to the one obtained in [20]. In figure 3.43 the particle composition systematic error and all the contributions are shown for $\sqrt{s} = 13$ TeV analysis. The same

result was obtained for $\sqrt{s} = 5.02$ TeV analysis.

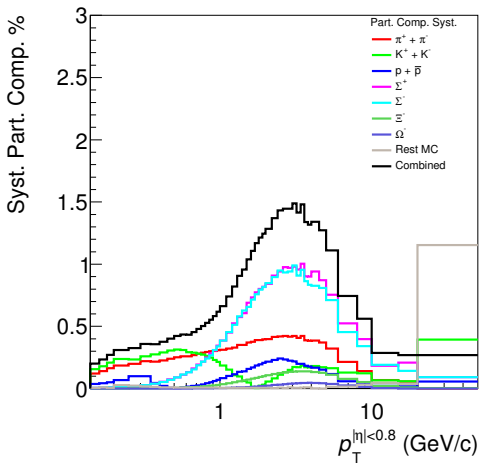


Figure 3.43: Particle composition systematic error for each particle and the total contributions for the $\sqrt{s} = 13$ TeV analysis.

Since INEL $> 0$ efficiency was used to correct all the multiplicity bins, a systematic error was assigned to the multiplicity bins. The evolution of the efficiency with the multiplicity was computed, as mentioned in 7, with pp at 7 TeV data. From right panel of figure 3.19, we can observe the considered systematic for low $p_{\mathrm{T}}$ (from 0.15 to 2.0 GeV/$c$) as the black line, and for high $p_{\mathrm{T}}$ we considered a 3% flat. This error was applied to all the multiplicity bins.

### 3.7.5 Vertex selection

The study was done varying the cut on the z coordinate of the primary vertex. The default value is ± 10cm, the considered variations for this study were ± 5cm and ± 20cm. As in the pile up systematic, we divide the sample in only three multiplicity bins for each estimator, highest variations on the $p_{\mathrm{T}}$ spectra for each bin were taken. This systematic error doesn't show a clear multiplicity dependence. At the end, a constant 0.5% was considered for INEL $> 0$ (as in [20]) as for the multiplicity bins.

### 3.7.6 Signal loss

Signal loss was computed purely with the MC using PYTHIA 6 simulations. The difference with PYTHIA 8 was assigned as a systematic uncertainty. Signal loss systematic error in function of multiplicity for the $\sqrt{s} = 13$ TeV data can be observed in figure 3.44, Results obtained for the $\sqrt{s} = 5.02$ TeV analysis can be seen in figures 3.45 and 3.46 for low and high intensity runs.

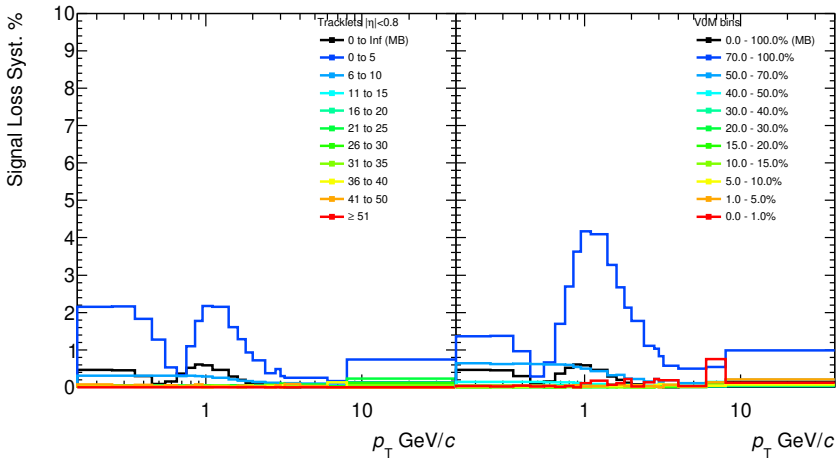


Figure 3.44: Signal loss systematic error in function of multiplicity, Tracklets (left) and V0M (right) estimators, at $\sqrt{s} = 13$ TeV data.

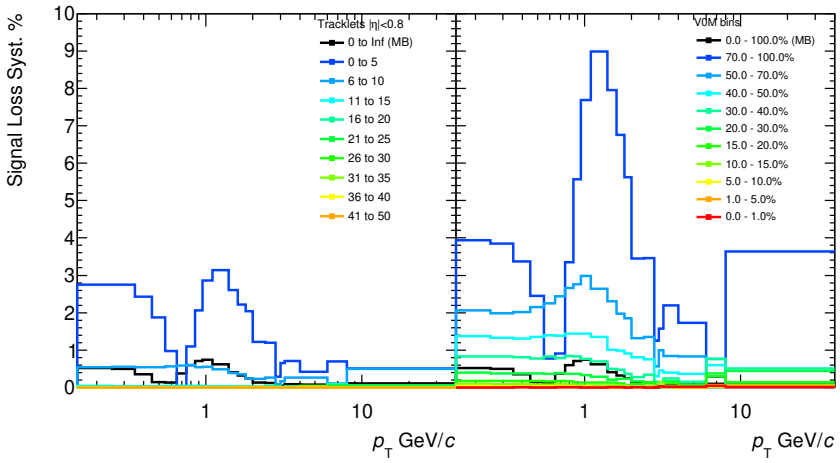


Figure 3.45: Signal loss systematic error in function of multiplicity, tracklets (left) and V0M (right) estimators, $\sqrt{s} = 5.02$ TeV data for low intensity runs.

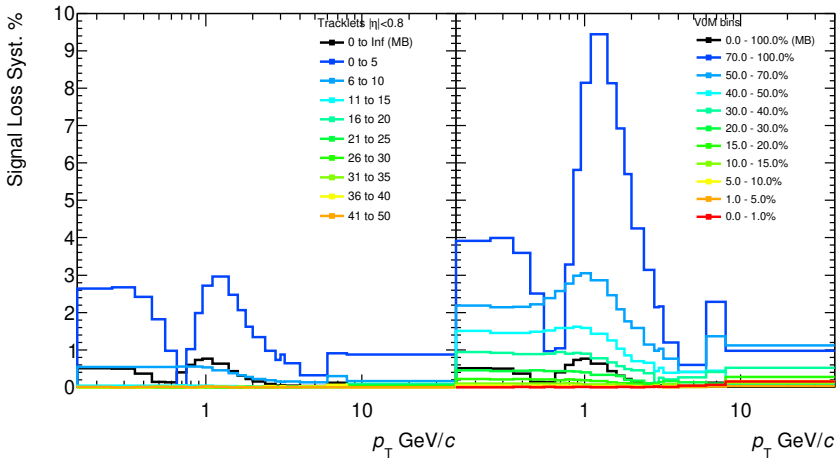


Figure 3.46: Signal loss systematic error in function of multiplicity, Tracklets (left) and V0M (right) estimators, at $\sqrt{s} = 5.02$ TeV data for high intensity runs.

### 3.7.7 Trigger efficiency (normalization)

In the same way as for the signal loss, the trigger efficiency was computed purely with the MC, PYTHIA 6 was used as the basis and the difference with PYTHIA 8 was assigned as a systematic error. This systematics is common for all the $p_{\mathrm{T}}$ bins and is not added to the other contributions it is reported apart. Figure 3.47 shows the normalization systematic error for the $\sqrt{s} = 13$ TeV analysis, similar results obtained for $\sqrt{s} = 5.02$ TeV .

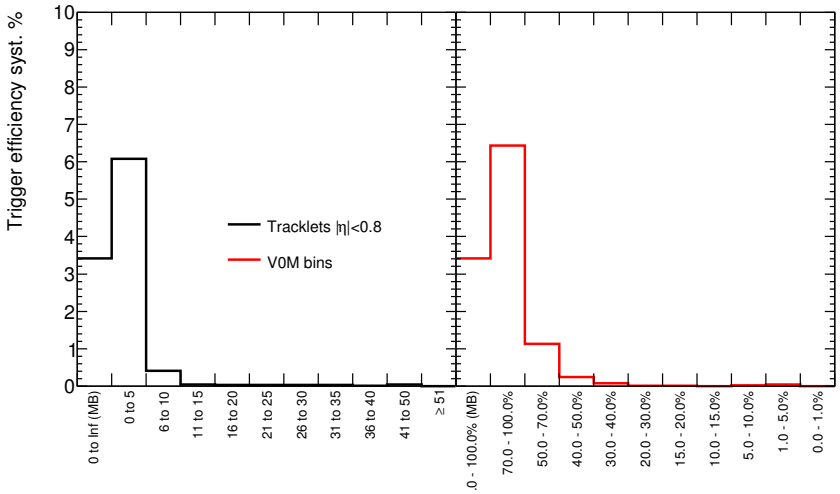


Figure 3.47: Trigger efficiency systematic error in function of multiplicity, Tracklets (left) and V0M (right) estimators, at $\sqrt{s} = 13$ TeV data.

### 3.7.8 Total systematic uncertainties

All the contributions were considered as independent. In order to estimate the total systematic errors we added all the contributions in quadrature. An example of how it looks for the MB case of the $\sqrt{s} = 13$ TeV analysis can be observed in figure 3.48.

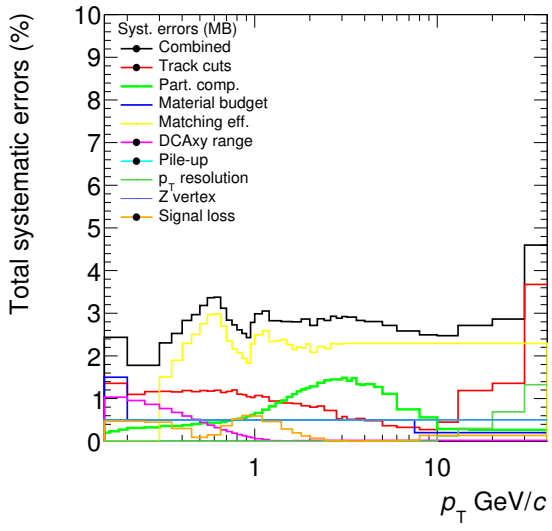


Figure 3.48: Total systematic errors for MB case, at $\sqrt{s} = 13$ TeV data.

For the multiplicity bins the total systematics were computed in the same way than in MB. An example for the lowest and highest multiplicity bins for the Tracklet estimator for the $\sqrt{s} = 13$ TeV analysis can be seen in figure 3.49.

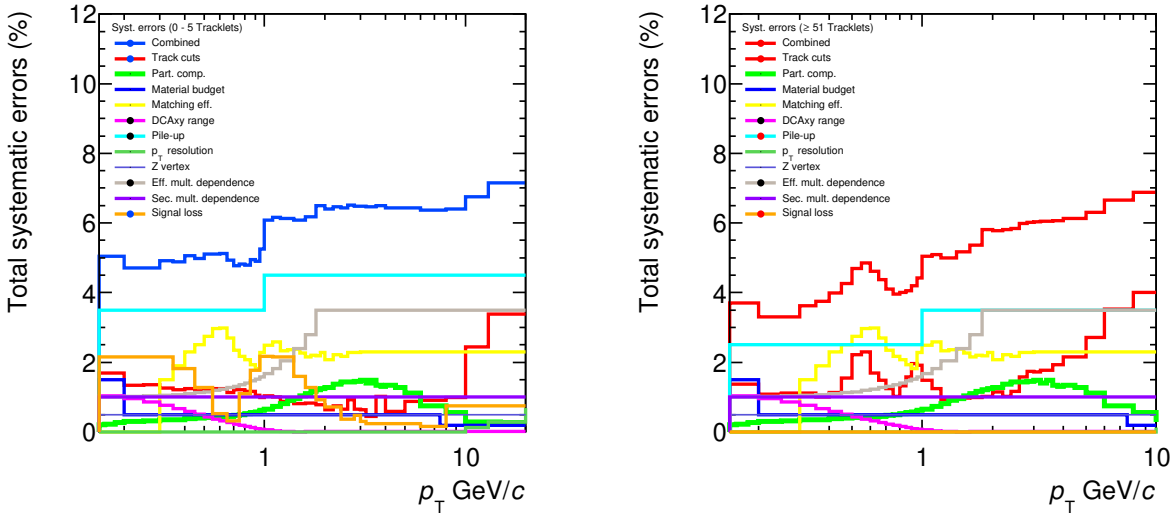


Figure 3.49: Total systematic errors for lowest (left) and highest (right) Tracklets bins, $\sqrt{s} = 13$ TeV analysis.

### 3.7.9 Multiplicity uncorrelated systematic errors

Some contributions to the systematic errors were taken as a common for all the multiplicity bins: $Z_{vtx}$ cut, matching efficiency, $p_{\mathrm{T}}$ resolution, material budget, particle composition and feed down. The other contributions, track cuts, pile-up, secondaries and efficiency multiplicity dependence and signal loss shows a multiplicity dependence.

For the case of the track cuts and the pile up, the uncorrelated errors were taken as in [22], following equation 3.13:

$$Syst_{uncorrelated}(\%) = \left| \frac{(dN/dp_{\mathrm{T}})^{Mult\,Bin\,variated}/(dN/dp_{\mathrm{T}})^{Mult\,Bin\,nominal}}{(dN/dp_{\mathrm{T}})^{INEL>0.,variated}/(dN/dp_{\mathrm{T}})^{INEL>0.\,nominal}} - 1 \right| \mathrm{x100} \tag{3.13}$$

where $MultBin$ refers to the spectra in multiplicity bins, and *variated* refers to the spectra with the variated cut that will be compared with the one with the nominal values.

An example for the lowest and highest multiplicity bins for the Tracklets estimator for the $\sqrt{s} =$ 13 TeV analysis can be seen in figure 3.50.

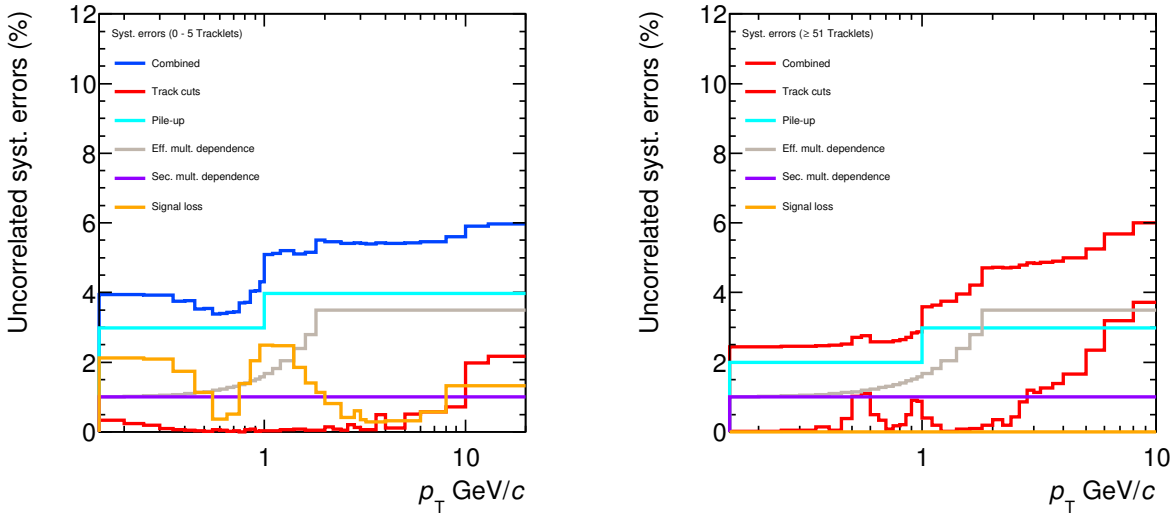


Figure 3.50: Uncorrelated systematic errors for lowest (left) and highest (right) tracklets multiplicity bins, $\sqrt{s} = 13$ TeV analysis.

### 3.7.10 Summary of the total and uncorrelated systematic errors

Total and uncorrelated systematic errors as a function of multiplicity for the pp at $\sqrt{s} = 13$ TeV analysis are shown in figure 3.51, and for $\sqrt{s} = 5.02$ TeV data in figures 3.52 and 3.53, for low and high intensity runs respectively.

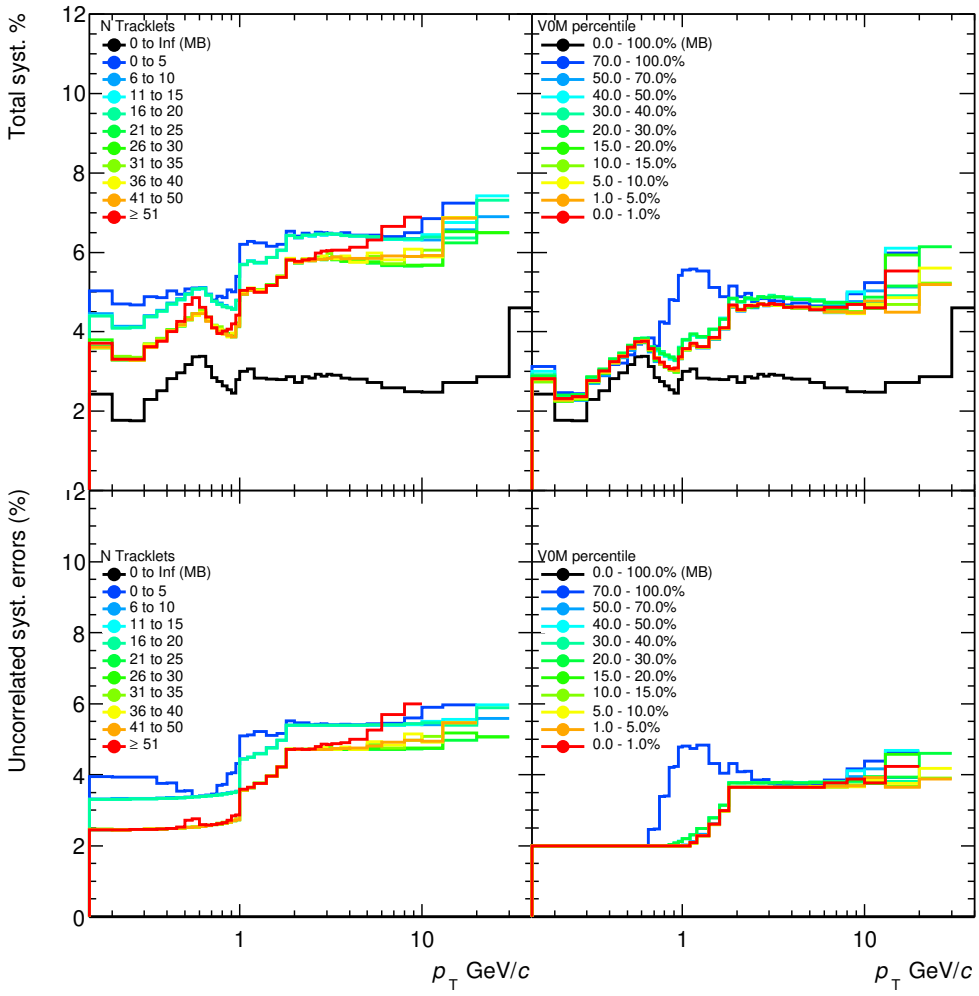


Figure 3.51: Total systematic errors for tracklets (top left) and V0M (top right) and uncorrelated systematic errors for tracklets (bottom left) and V0M (bottom right), at $\sqrt{s} = 13$ TeV data.

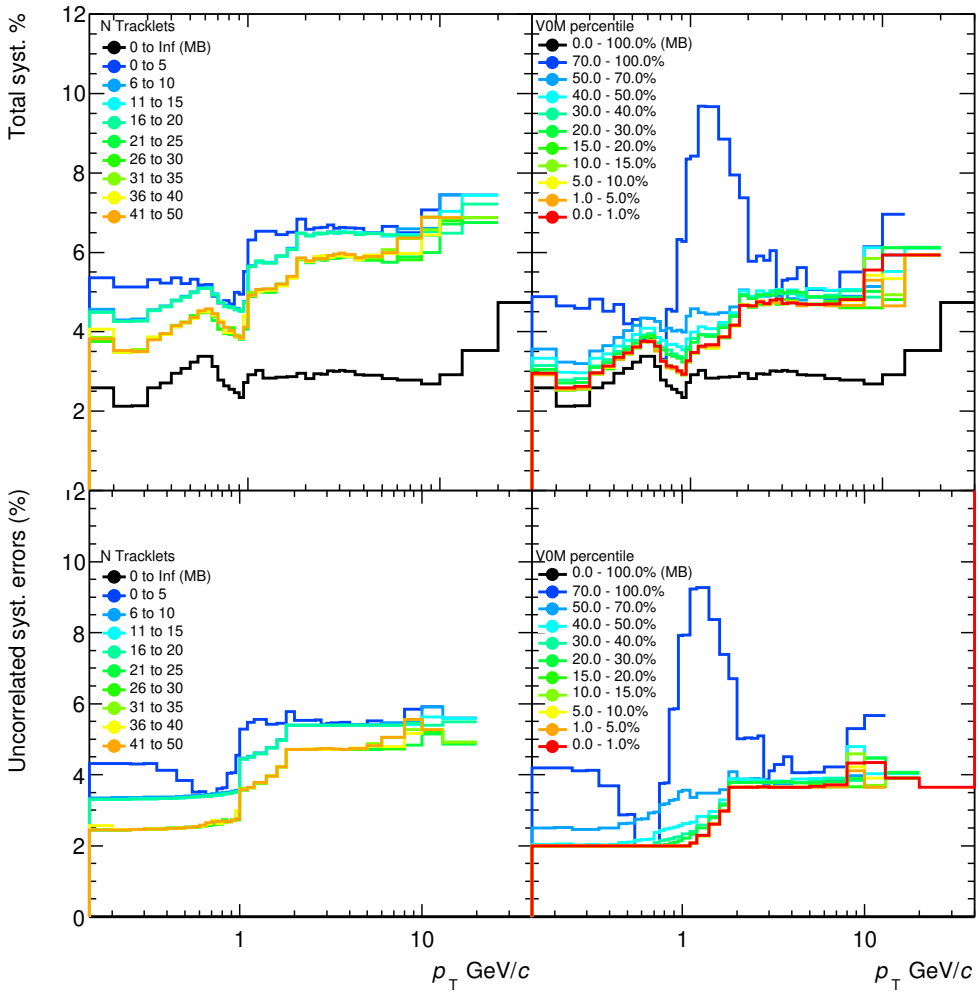


Figure 3.52: Total systematic errors for tracklets (top left) and V0M (top right) and uncorrelated systematic errors for tracklets (bottom left) and V0M (bottom right), at $\sqrt{s} = 5.02$ TeV data, of low intensity runs.

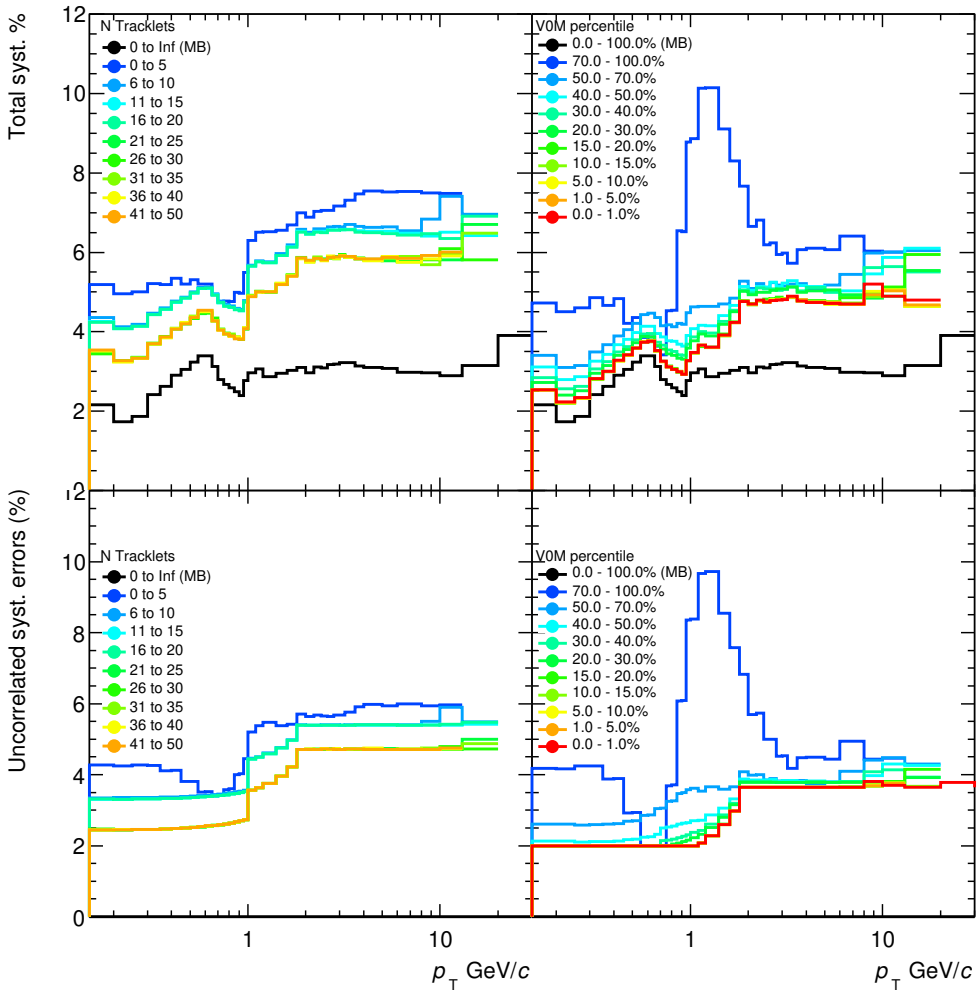


Figure 3.53: Total systematic errors for tracklets (top left) and V0M (top right) and uncorrelated systematic errors for tracklets (bottom left) and V0M (bottom right), at $\sqrt{s} = 5.02$ TeV data, of high intensity runs.

### 3.7.11 $\langle dN/d\eta \rangle$ computation error

As will be explained in section 3.8.4, $\langle dN/d\eta \rangle$ was computed by integrating the $p_{\mathrm{T}}$ spectra in the multiplicity bins, for this is was necessary to extrapolate to the low $p_{\mathrm{T}}$ region that was not measured (0.15 - 1.0 GeV/$c$). Three components of uncertainty were taken into account for the measurement of this quantity, that will be described below. Our first source of uncertainty comes from the extrapolation using the Hagedorn function (from 0.15 - 1.0 GeV/$c$). For this reason we used another four functions to extrapolate to the low $p_{\mathrm{T}}$ region. The fits were done in the range where the functions fit the best, the largest difference with the results obtained using the Hagedorn function, was taken as the uncertainty. The functions and the ranges used can be consulted in table 3.5.

| **Function** | **Fit range** (GeV/$c$) |
|---|---|
| Hagedorn(Basis) | 0.15 - 1.0 |
| Levy-Tsallis | 0.15 - 1.0 |
| Boltzmann | 0.15 - 0.3 |
| True-Tsallis | 0.15 - 1.0 |
| BGBlastWave | 0.15 - 1.0 |

Table 3.5: Functions used to extrapolate the low unmeasured $p_{\mathrm{T}}$ region and the range of the fits.

The quality of the fits of the different functions, for the $\sqrt{s} = 13$ TeV analysis, can be consulted in figures 3.54, 3.55, 3.56, 3.57 and 3.58. Similar results obtained for the $\sqrt{s} = 5.02$ TeV data analysis.

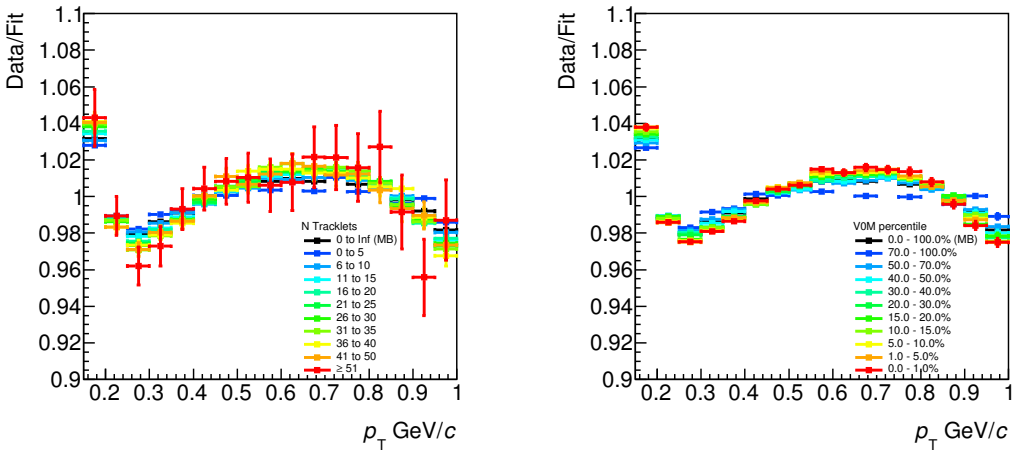


Figure 3.54: Quality of the Hagedorn fits for Tracklets (left) and V0M (right), at $\sqrt{s} = 13$ TeV analysis.

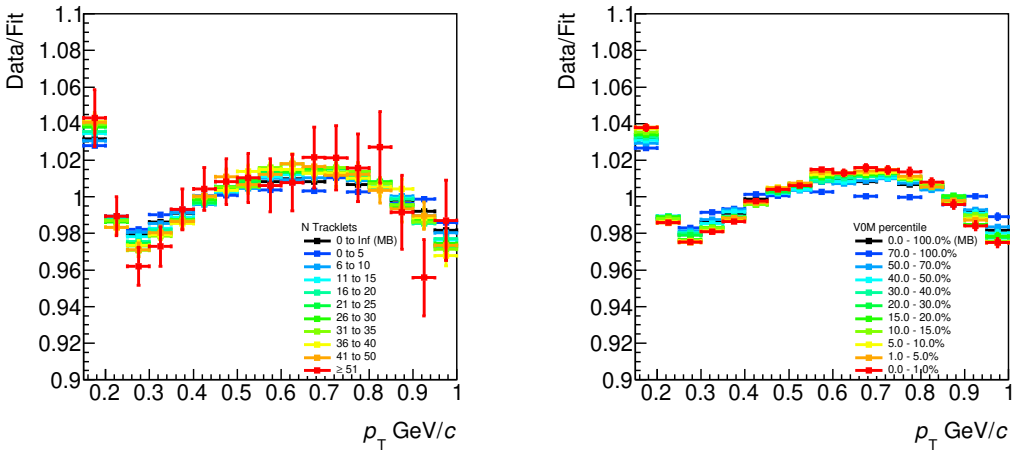


Figure 3.55: Quality of the Levy-Tsallis fits for tracklets (left) and V0M (right), at $\sqrt{s} = 13$ TeV data analysis.

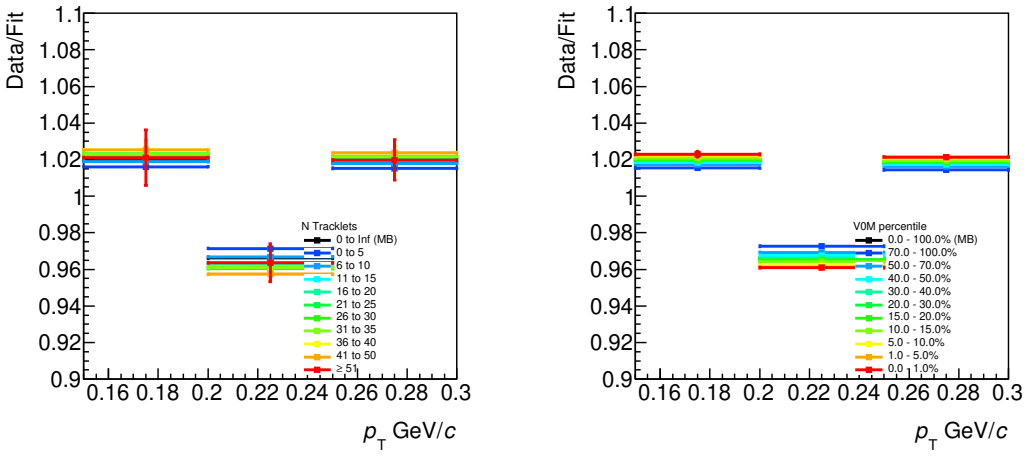


Figure 3.56: Quality of the Boltzmann fits for tracklets (left) and V0M (right), at $\sqrt{s} = 13$ TeV data analysis.

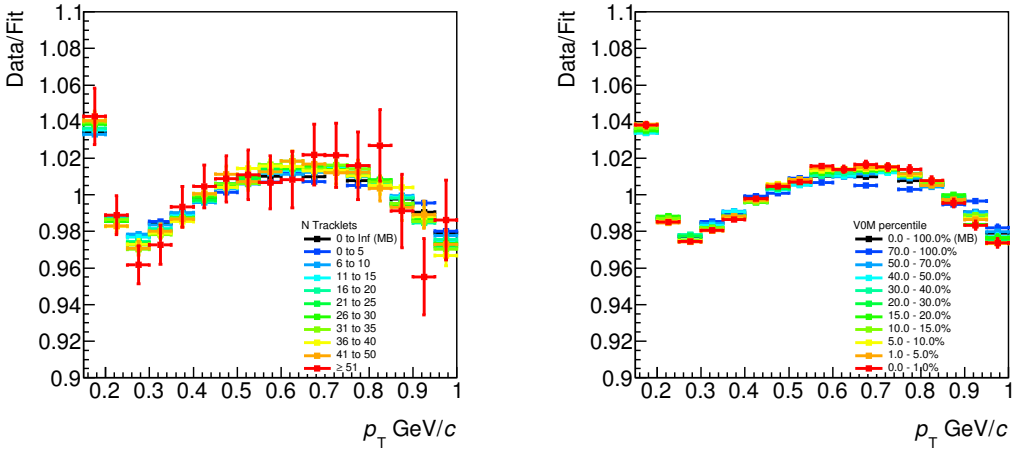


Figure 3.57: Quality of the True-Tsallis fits for Tracklets (left) and V0M (right), at $\sqrt{s} = 13$ TeV analysis.

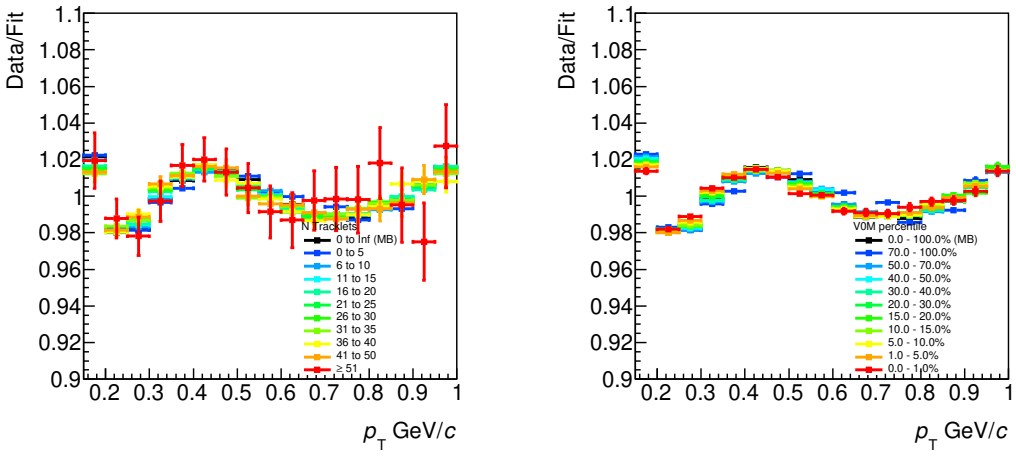


Figure 3.58: Quality of the BGBlastWave fits for tracklets (left) and V0M (right), at $\sqrt{s} = 13$ TeV data analysis.

The second source of uncertainty is the systematic errors of the measured spectra. We shift the spectra to the top and bottom of the systematic errors, then we fit the Hagedorn function (basis function to extrapolate the low $p_{\mathrm{T}}$ region) and compute the $\langle dN/d\eta \rangle$.

The third source of uncertainty is the normalization systematic error, values shown in figure 3.47, and the similar ones obtained for the $\sqrt{s} = 5.02$ TeV analysis. Finally, the three components were added in quadrature.

### 3.7.12 Systematic errors of the power law exponent

The power law exponent as a function of multiplicity was extracted by fitting power law functions to the spectra above 4.0 GeV/$c$. To compute the systematic error related to the exponent of the power law fit, we move the spectra inside the total systematic errors as hard as it can be and as soft as it can be, an example can be found in figure 3.59

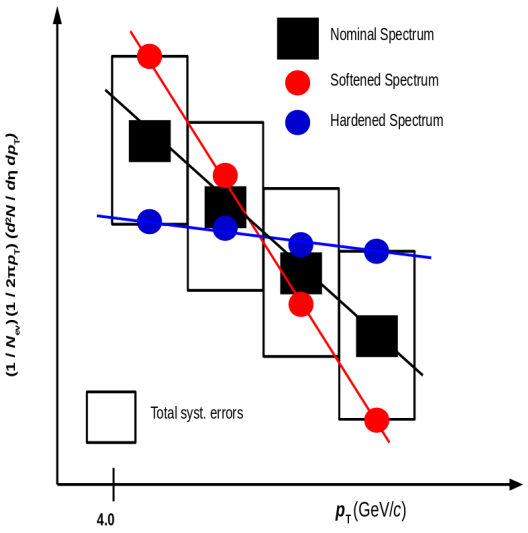


Figure 3.59: Example of how the power law exponent systematic error was computed.

The percentage assigned to each of the multiplicity bins for both energies: $\sqrt{s} = 5.02$ and 13 TeV , and both multiplicity estimators can be consulted in tables 3.6, 3.7, 3.8 and 3.9.

| N Tracklets | Power law exp. | syst. (%) |
|---|---|---|
| 0 to 5 | 6.21 | 2.27 |
| 6 to 10 | 6.01 | 2.11 |
| 11 to 15 | 5.87 | 2.12 |
| 16 to 20 | 5.78 | 2.10 |
| 21 to 25 | 5.66 | 1.94 |
| 26 to 30 | 5.58 | 1.97 |
| 31 to 35 | 5.48 | 2.08 |
| 36 to 40 | 5.42 | 2.23 |
| 41 to 50 | 5.36 | 2.40 |
| $\geq 51$ | 5.01 | 3.57 |

Table 3.6: Values of the power law exponent and the assigned systematic error for the tracklets multiplicity bins, at $\sqrt{s} = 13$ TeV data.

| N Tracklets | Power law exp. | syst. (%) |
|---|---|---|
| 70 - 100% | 6.14 | 1.84 |
| 50 - 70% | 5.94 | 1.64 |
| 40 - 50% | 5.90 | 1.67 |
| 30 - 40% | 5.88 | 1.61 |
| 20 - 30% | 5.83 | 1.59 |
| 15 - 20% | 5.80 | 1.56 |
| 10 - 15% | 5.79 | 1.53 |
| 5 - 10% | 5.79 | 1.53 |
| 1 - 5% | 5.77 | 1.53 |
| 0 - 1% | 5.77 | 1.62 |

Table 3.7: Values of the power law exponent and the assigned systematic error for the V0M multiplicity bins, at $\sqrt{s} = 13$ TeV data.

| N Tracklets | Power law exp. | syst. (%) |
|---|---|---|
| 0 to 5 | 6.63 | 3.05 |
| 6 to 10 | 6.35 | 2.49 |
| 11 to 15 | 6.17 | 2.34 |
| 16 to 20 | 6.04 | 2.29 |
| 21 to 25 | 5.92 | 2.17 |
| 26 to 30 | 5.83 | 2.33 |
| 31 to 35 | 5.77 | 2.40 |
| 36 to 40 | 5.65 | 2.71 |
| 41 to 50 | 5.52 | 2.78 |

Table 3.8: Values of the power law exponent and the assigned systematic error for the tracklets multiplicity bins, at $\sqrt{s} = 5.02$ TeV data.

| N Tracklets | Power law exp. | syst. (%) |
|---|---|---|
| 70 - 100% | 6.35 | 2.62 |
| 50 - 70% | 6.24 | 2.18 |
| 40 - 50% | 6.13 | 2.22 |
| 30 - 40% | 6.11 | 2.06 |
| 20 - 30% | 6.09 | 1.81 |
| 15 - 20% | 6.06 | 1.80 |
| 10 - 15% | 6.06 | 1.90 |
| 5 - 10% | 6.04 | 1.87 |
| 1 - 5% | 6.02 | 1.82 |
| 0 - 1% | 6.02 | 1.96 |

Table 3.9: Values of the power law exponent and the assigned systematic error for the V0M multiplicity bins, at $\sqrt{s} = 5.02$ TeV data.

### 3.7.13 Systematic errors of integrated yields

Integrated yields of the $p_{\mathrm{T}}$ spectra, from 4 to 10 GeV/$c$, in multiplicity bins divided by the INEL $> 0.$ one were also computed in this analysis. To compute the systematic errors related to this observable, we shift the spectra of the multiplicity bins inside the uncorrelated systematic error (which is zero for the INEL $> 0.$ case), up and then down. The highest variation was considered as the systematic error. Values of the ratios of the integrated yields to the INEL $> 0.$ one and the assigned errors can be consulted in tables 3.10, 3.11, 3.12 and 3.13 for both energies: $\sqrt{s} = 5.02$ and 13 TeV , and both multiplicity estimators.

| N Tracklets | Int. Yield$^{Multiplicity\,bin}$ /Int. Yield$^{INEL>0.}$ | syst. (%) |
|---|---|---|
| 0 to 5 | 0.14 | 5.40 |
| 6 to 10 | 1.06 | 5.39 |
| 11 to 15 | 2.48 | 5.39 |
| 16 to 20 | 4.26 | 5.39 |
| 21 to 25 | 6.35 | 4.71 |
| 26 to 30 | 8.75 | 4.72 |
| 31 to 35 | 11.42 | 4.75 |
| 36 to 40 | 14.88 | 4.77 |
| 41 to 50 | 19.24 | 4.77 |
| $\geq 51$ | 29.34 | 5.12 |

Table 3.10: Values of the integrated yield in multiplicity bins over INEL $> 0.$ for the tracklets multiplicity bins, for $\sqrt{s} = 13$ TeV data.

| N Tracklets | Int. Yield$^{Multiplicity\,bin}$ /Int. Yield$^{INEL>0.}$ | syst. (%) |
|---|---|---|
| 70 - 100% | 0.09 | 3.71 |
| 50 - 70% | 0.40 | 3.64 |
| 40 - 50% | 0.74 | 3.78 |
| 30 - 40% | 1.10 | 3.78 |
| 20 - 30% | 1.61 | 3.77 |
| 15 - 20% | 2.17 | 3.64 |
| 10 - 15% | 2.70 | 3.65 |
| 5 - 10% | 3.50 | 3.64 |
| 1 - 5% | 4.92 | 3.64 |
| 0 - 1% | 7.54 | 3.65 |

Table 3.11: Values of the integrated yield in multiplicity bins over INEL $> 0.$ for the V0M multiplicity bins, for $\sqrt{s} = 13$ TeV data.

| N Tracklets | Int. Yield$^{Multiplicity\,bin}$ /Int. Yield$^{INEL>0.}$ | syst. (%) |
|---|---|---|
| 0 to 5 | 0.11 | 6.00 |
| 6 to 10 | 0.83 | 5.41 |
| 11 to 15 | 2.11 | 5.42 |
| 16 to 20 | 3.81 | 5.41 |
| 21 to 25 | 5.88 | 4.76 |
| 26 to 30 | 8.38 | 4.75 |
| 31 to 35 | 11.31 | 4.77 |
| 36 to 40 | 14.57 | 4.77 |
| 41 to 50 | 19.26 | 4.84 |

Table 3.12: Values of the integrated yield in multiplicity bin over INEL $> 0.$ for the tracklets multiplicity bins, for $\sqrt{s} = 5.02$ TeV data.

| N Tracklets | Int. Yield$^{Multiplicity\,bin}$ /Int. Yield$^{INEL>0.}$ | syst. (%) |
|---|---|---|
| 70 - 100% | 0.10 | 4.50 |
| 50 - 70% | 0.42 | 3.81 |
| 40 - 50% | 0.74 | 3.90 |
| 30 - 40% | 1.08 | 3.81 |
| 20 - 30% | 1.55 | 3.80 |
| 15 - 20% | 2.06 | 3.67 |
| 10 - 15% | 2.55 | 3.66 |
| 5 - 10% | 3.28 | 3.66 |
| 1 - 5% | 4.55 | 3.67 |
| 0 - 1% | 6.91 | 3.69 |

Table 3.13: Values of the integrated yield in multiplicity bins over INEL $> 0.$ for the V0M multiplicity bins, at $\sqrt{s} = 5.02$ TeV data analysis.

## 3.8 Cross checks

The idea of this section is to prove that the analysis was done right and the results are consistent with other analyses or by checking consistency in some details of our own results.

### 3.8.1 Consistency between MB and multiplicity bins

To see that the normalization is under control was the first cross check we made. The consistency between the spectra in multiplicity bins and the MB was checked following the equation 3.14.

$$\frac{\sum_{Mult.Bins} \frac{N_{ev}^{Mult.Bin}}{N_{ev}^{MB}} \frac{dN^{Mult.Bin}}{dp_{\mathrm{T}}}}{\frac{dN^{M.B.}}{dp_{\mathrm{T}}}} = 1 \tag{3.14}$$

The ratios between the MB and the sum of the weighted multiplicity bins are shown in figures 3.60, 3.61 and 3.62 for the $\sqrt{s} = 5.02$ and 13 TeV data. The maximum deviations are of 2% and can be attributed to the differences in the calculation of the fractional signal loss which was calculated in the inclusive case using only MC generator simulations. This deviations are within the systematical errors.

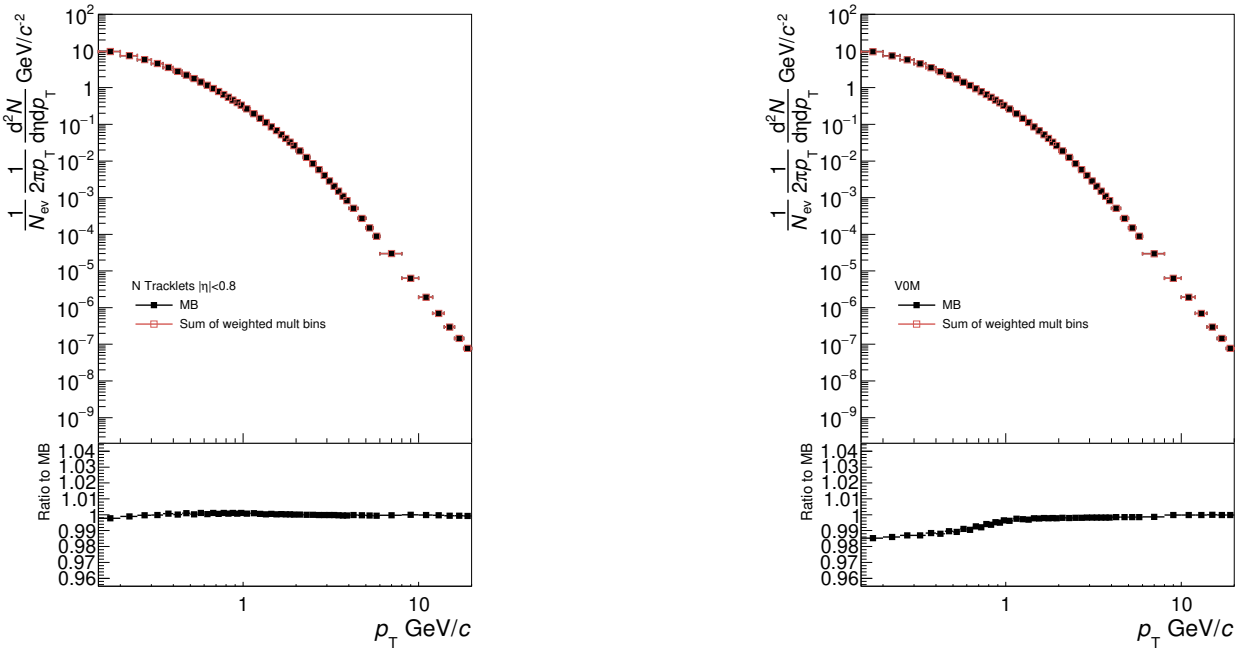


Figure 3.60: Consistency between multiplicity bins and M.B. case for tracklets (left) and V0M (right), for $\sqrt{s} = 13$ TeV data.

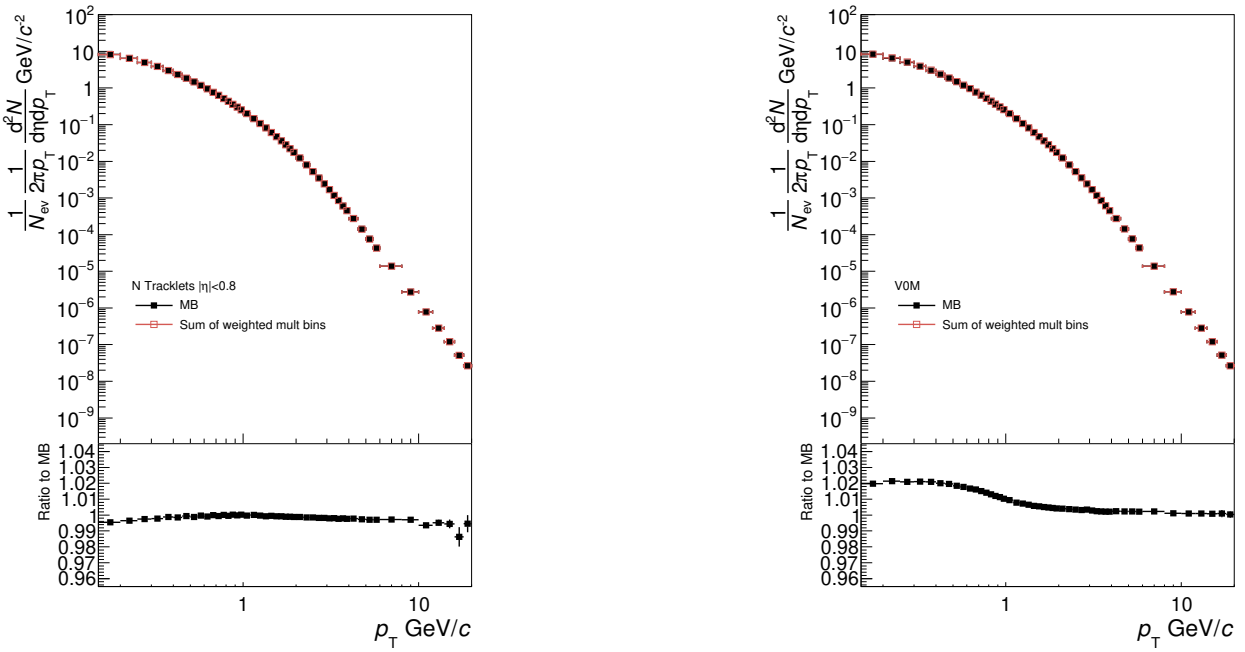


Figure 3.61: Consistency between multiplicity bins and MB case for tracklets (left) and V0M (right), for $\sqrt{s} = 5.02$ TeV data, for low intensity runs.

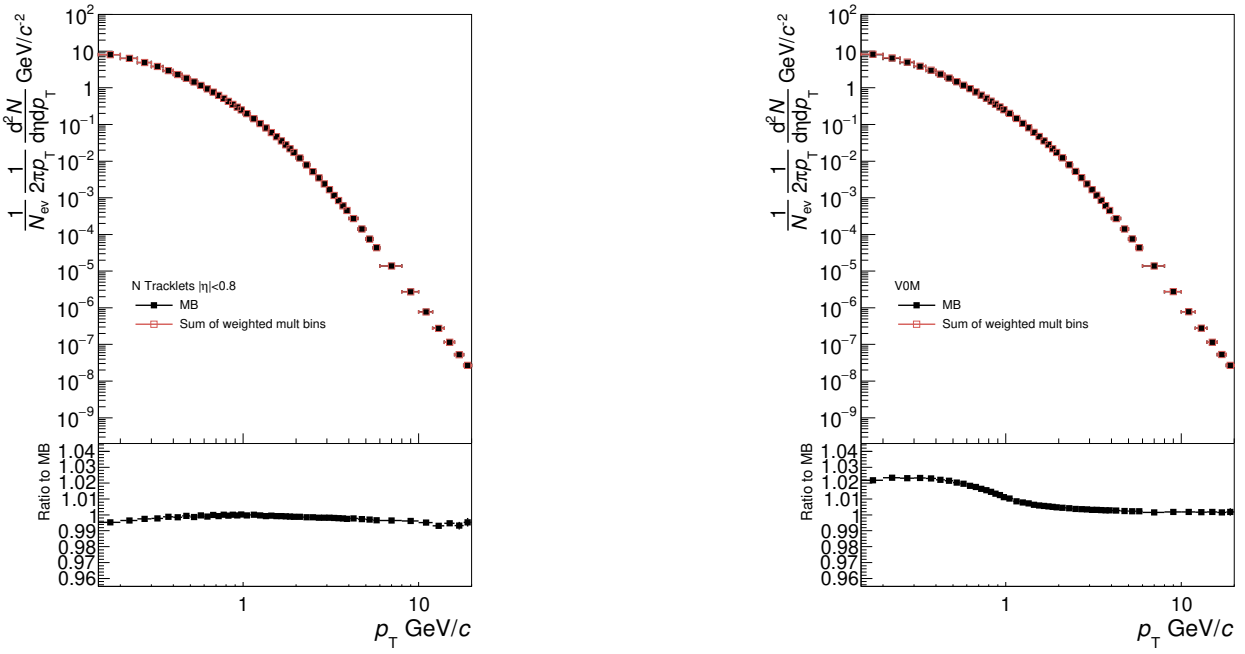


Figure 3.62: Consistency between multiplicity bins and MB case for tracklets (left) and V0M (right), for $\sqrt{s} = 5.02$ TeV data, for high intensity runs.

### 3.8.2 Consistency with 13 TeV published result

In this section we compare our INEL $> 0$ $p_{\mathrm{T}}$ spectrum at $\sqrt{s} = 13$ TeV result with the published one [3]. The comparison can be observed in figure 3.63. As can be seen, there is a deviation of 10% at mid $p_{\mathrm{T}}$ but is well covered by the systematic errors.

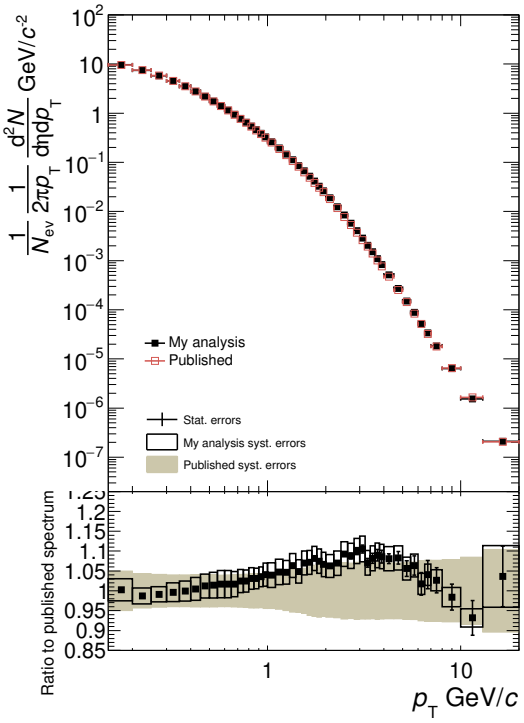


Figure 3.63: Comparison of INEL $> 0$ at $\sqrt{s} = 13$ TeV $p_{\mathrm{T}}$ spectrum obtained in this analysis with the published.

The differences are logical since in the published result the MC particle composition was used to compute the tracking efficiency, no real particle composition was applied. The correction for secondaries were taken from MC (no DCAxy template fits) and no signal loss correction was applied (probably signal loss no required in the published result, since it was done with kMB trigger). Also, the inclusion of the geometric-length track cut instead of the N crossed TPC rows, leads to a bump at mid $p_{\mathrm{T}}$ . When we correct our result with the MC efficiency and MC secondaries, remove the signal loss, remove the geo-cuts and keep the N crossed rows cut and using kMB trigger, we are able to reproduce the published result, see figure 3.64.

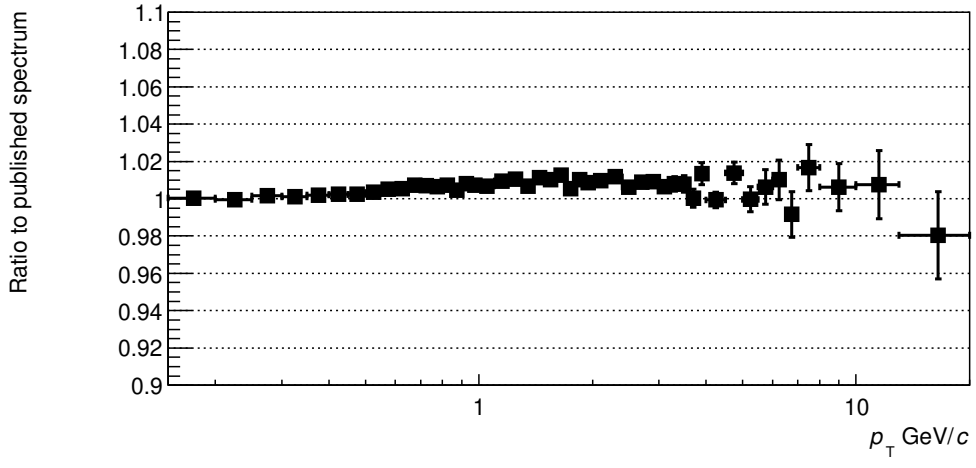


Figure 3.64: Comparison of MB $\sqrt{s} = 13$ TeV $p_{\mathrm{T}}$ spectrum obtained in this analysis, without particle composition, without feed down, without signal loss, replacing geo-cuts by N crossed rows and using kMB trigger (conditions of the publication), with the published result.

### 3.8.3 Consistency with 5 TeV MB analysis

Here we compare our data at 5 TeV MB result with the one obtained in[20]. The most recent correction techniques are applied in both results, i.e. particle composition, feed down and signal loss. As can be observed in figure 3.65, both analyses are in agreement within 1.5% differences.

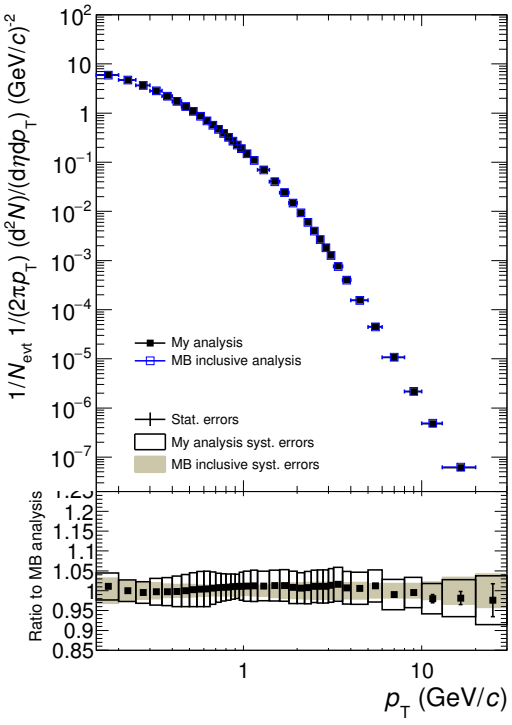


Figure 3.65: Comparison of INEL $> 0$ at $\sqrt{s} = 5.02$ TeV $p_{\mathrm{T}}$ spectrum obtained in this analysis with the one obtained in [20].

### 3.8.4 $\langle dN/d\eta \rangle$ comparison

We compute the mean true multiplicity ($\langle dN/d\eta \rangle$) for each of the multiplicity bins by integrating the spectra and extrapolating the unmeasured region with the Hagedorn function, more fits and the systematic errors of the spectra were considered to compute the systematic errors of the $\langle dN/d\eta \rangle$, see section 10 for more details.

#### a) with multiplicity PAG results

The measured multiplicity is compared with the one measured by the dedicated analysis as a cross check. Tables with the comparisons can be observed in 3.14 and 3.15 for $\sqrt{s} = 5.02$ and 13 TeV .

| V0M bins | $\langle dN/d\eta \rangle_{\|\eta\|<0.8}$(syst.(%)[1]) (This analysis) | $\langle dN/d\eta \rangle_{\|\eta\|<0.5}$(syst.(%)) (Mult. PAG ana.[2]) |
|---|---|---|
| 0 - 100%(M-B.) | 7.15 (4.65) | 6.49 (2.92)[3] |
| 70 - 100% | 2.62 (7.38) | 2.76 (1.81) |
| 50 - 70% | 5.11 (3.68) | 4.77 (1.88) |
| 40 - 50% | 7.08 (3.81) | 6.62 (1.96) |
| 30 - 40% | 8.80 (3.86) | 8.24 (2.06) |
| 20 - 30% | 10.98 (3.91) | 10.31 (2.03) |
| 15 - 20% | 13.07 (3.81) | 12.28 (2.03) |
| 10 - 15% | 14.88 (3.80) | 14.00 (2.07) |
| 5 - 10% | 17.40 (3.83) | 16.40 (2.07) |
| 1 - 5% | 21.36 (3.85) | 20.16 (2.03) |
| 0 - 1% | 27.61 (3.87) | 26.18 (2.10) |

Table 3.14: $\langle dN/d\eta \rangle$ measured by this analysis and a comparison with the values measured by the dedicated analysis, at $\sqrt{s} = 13$ TeV data.

| V0M bins | $\langle dN/d\eta \rangle_{\|\eta\|<0.8}$(syst.(%)[4]) (This analysis) | $\langle dN/d\eta \rangle_{\|\eta\|<0.5}$ (Mult. PAG ana.[5] ) |
|---|---|---|
| 0 - 100%(INEL $> 0$) | 5.77 (4.50) | 5.59 (1.43) |
| 70 - 100% | 2.36 (9.45) | 2.63 |
| 50 - 70% | 4.15 (4.75) | 4.09 |
| 40 - 50% | 5.56 (4.58) | 5.37 |
| 30 - 40% | 6.80 (4.26) | 6.50 |
| 20 - 30% | 8.38 (4.09) | 7.93 |
| 15 - 20% | 9.88 (3.91) | 9.30 |
| 10 - 15% | 11.19 (3.91) | 10.52 |
| 5 - 10% | 12.97 (3.92) | 12.16 |
| 1 - 5% | 15.77 (3.95) | 14.78 |
| 0 - 1% | 20.10 (3.97) | 18.81 |

Table 3.15: $\langle dN/d\eta \rangle$ measured by this analysis and a comparison with the values measured by the dedicated analysis, at $\sqrt{s} = 5.02$ TeV .

**b) comparison with PYTHIA 8**

The values that are not measured by the dedicated analysis at the moment are compared with PYTHIA MC. See tables 3.16 and 3.17. With this comparison we want to check that the MC and the data follows the same behaviors, not the same values necessarily.

[1] Normalization systematic errors also taken into account, see section 10.10
[2] Approved results, presented in QM2017[30]
[3] Published result [3]
[4] Normalization systematic errors also taken into account, see section 10.10
[5] First preliminary values, not approved at the moment.

| N Tracklets | $\langle dN/d\eta \rangle_{\|\eta\|<0.8}$(syst.(%)[6]) (This analysis) | $\langle dN/d\eta \rangle_{\|\eta\|<0.8}$ (PYTHIA 8 Monash) |
|---|---|---|
| 0 to 5 | 3.02 (7.93) | 3.31 |
| 6 to 10 | 9.43 (5.21) | 8.73 |
| 11 to 15 | 15.08 (5.28) | 14.22 |
| 16 to 20 | 20.47 (5.34) | 19.3 |
| 21 to 25 | 25.71 (4.74) | 24.06 |
| 26 to 30 | 30.81 (4.83) | 28.61 |
| 31 to 35 | 35.87 (4.83) | 33.07 |
| 36 to 40 | 40.82 (4.83) | 37.32 |
| 41 to 50 | 46.94 (4.87) | 42.65 |
| $\geq 51$ | 56.50 (4.76) | 50.96 |

Table 3.16: $\langle dN/d\eta \rangle$ measured by this analysis and a comparison with reconstructed PYTHIA 8 Monash MC, at $\sqrt{s} = 13$ TeV .

| N Tracklets | $\langle dN/d\eta \rangle_{\|\eta\|<0.8}$(syst.(%)[7]) (This analysis) | $\langle dN/d\eta \rangle_{\|\eta\|<0.8}$ (PYTHIA 8 Monash) |
|---|---|---|
| 0 to 5 | 2.29 (7.82) | 2.55 |
| 6 to 10 | 6.82 (5.26) | 6.39 |
| 11 to 15 | 11.10 (5.31) | 10.45 |
| 16 to 20 | 15.26 (5.40) | 14.34 |
| 21 to 25 | 19.36 (4.83) | 18.1 |
| 26 to 30 | 23.41 (4.90) | 21.77 |
| 31 to 35 | 27.40 (5.01) | 25.41 |
| 36 to 40 | 31.38 (5.04) | 29 |
| 41 to 50 | 36.27 (5.09) | 33.41 |

Table 3.17: $\langle dN/d\eta \rangle$ measured by this analysis and a comparison with reconstructed PYTHIA 8 Monash MC, at $\sqrt{s} = 5.02$ TeV .

## 3.9 Merging the $\sqrt{s} = 5.02$ TeV data analysis, low and high intensity runs

As described before, the $\sqrt{s} = 5.02$ TeV analysis was done in two independent steps. High and low intensity runs were analyzed separately. We merge the fully corrected low and high intensity runs results by averaging them, propagating the statistical errors. For the systematic errors, we take the biggest for each bin. In figure 3.66, the results of the merged compared with high and low intensity runs results can be consulted. As can be seen, the ratios are consistent inside a 2%.

[6] Normalization systematic errors also taken into account, see section 10.10
[7] Normalization systematic errors also taken into account, see section 10.10

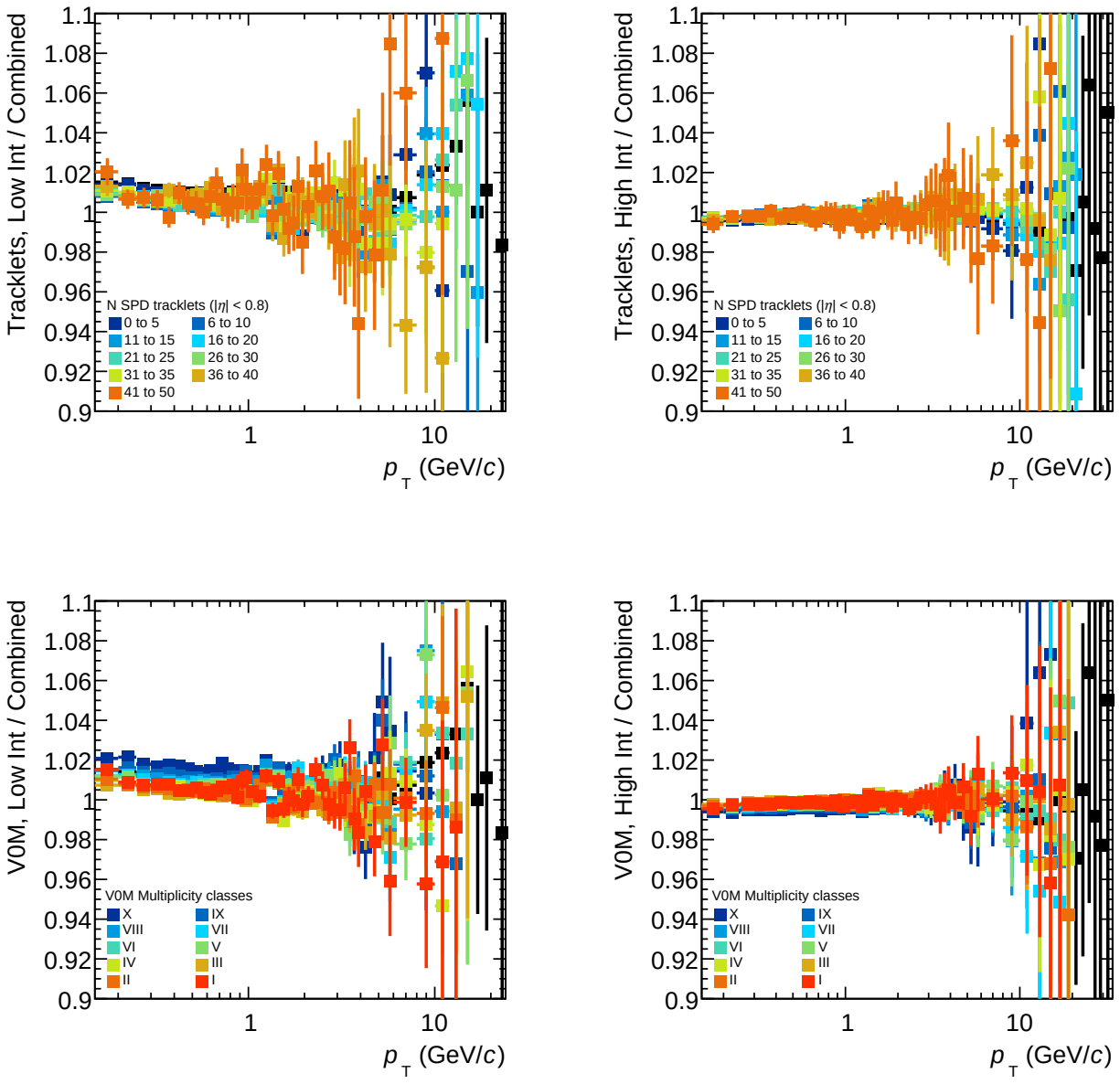


Figure 3.66: Ratios between low (top left) and high (top right) intensity runs to the combined results for the Tracklets case, same for the V0M (bottom), at $\sqrt{s} = 5.02$ TeV data analysis.

# Chapter 4

# Results and discussion

This chapter is conformed by two sections. First, the presentation and description of the results, many of them officially approved as preliminary results by the ALICE collaboration and were presented at the international conferences [33] and [32]. The second part of the chapter will consist of the discussions of the results and the conclusions of the thesis. In more detail, the first of the sections will contain the fully corrected $p_{\mathrm{T}}$ spectra in function of multiplicity for both multiplicity estimators (Tracklets and V0M) and both energies $\sqrt{s} = 5.02$ and 13 TeV . Also the analysis of exponent from the power law fit and the integrated yield vs multiplicity can be observed in this chapter.

## 4.1 Presentation of the results and discussion

### 4.1.1 $p_{\mathrm{T}}$ spectra for V0M multiplicity bins

In this section the results are shown for the V0M percentile analysis. For the $\sqrt{s} = 13$ TeV case, it is possible to see the spectra and the ratios to INEL $> 0$ in figure 4.1. The same results are shown for $\sqrt{s} = 5.02$ TeV analysis in figure 4.2.

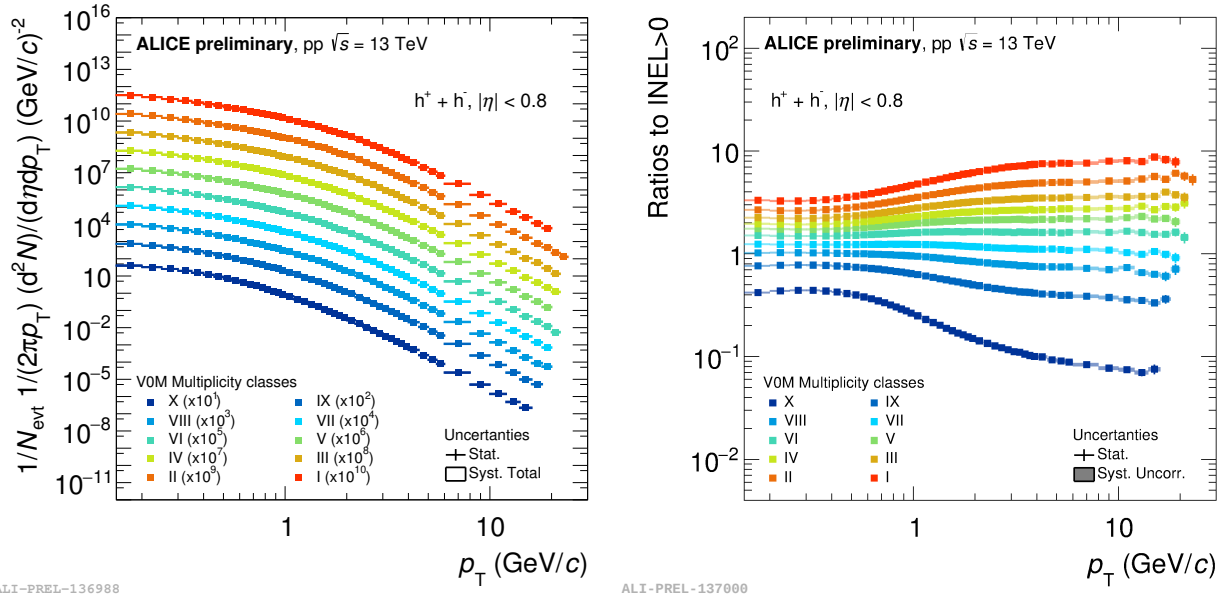


Figure 4.1: Measured $p_{\mathrm{T}}$ spectra of charged particles in V0M bins (left) and their ratios to the INEL $> 0$ case (right) for pp collisions at $\sqrt{s} = 13$ TeV .

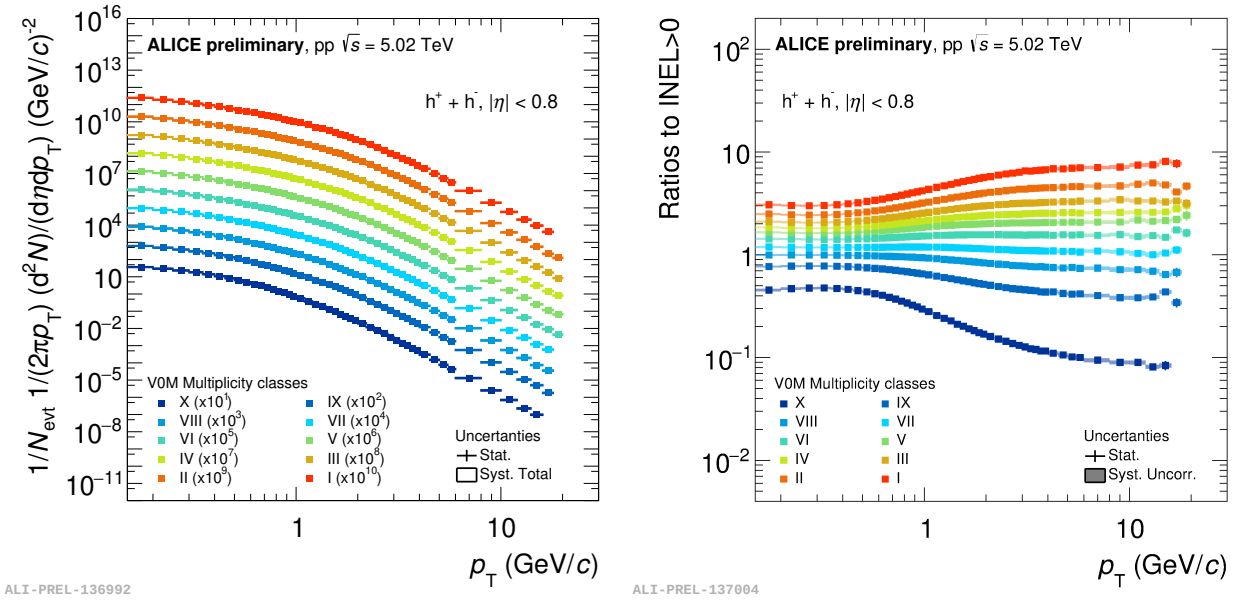


Figure 4.2: Measured $p_{\mathrm{T}}$ spectra of charged particles in V0M bins (left) and their ratios to the INEL $> 0$ case (right) for pp collisions at $\sqrt{s} = 5.02$ TeV .

As can be seen from figures 4.1 and 4.2, right panels, there is a saturation effect observed in the ratios for the highest multiplicity bins. The effect is present in both energies, $\sqrt{s} = 5.02$ and 13 TeV . We think that the effect is due to the wide regions of multiplicity in the central barrel that we indirectly select when we cut in a V0M multiplicity bin. It means, for a given V0M multiplicity bin, we have a mixture of low-mid-high multiplicity in the central barrel.

### 4.1.2 $p_{\mathrm{T}}$ spectra in Tracklets bins

In this sections the results for the Tracklets multiplicity estimator are shown. In figure 4.3 the spectra and the ratios to reference can be observed for the $\sqrt{s} = 13$ TeV analysis. For the $\sqrt{s} = 5.02$ TeV analysis results see figure 4.4.

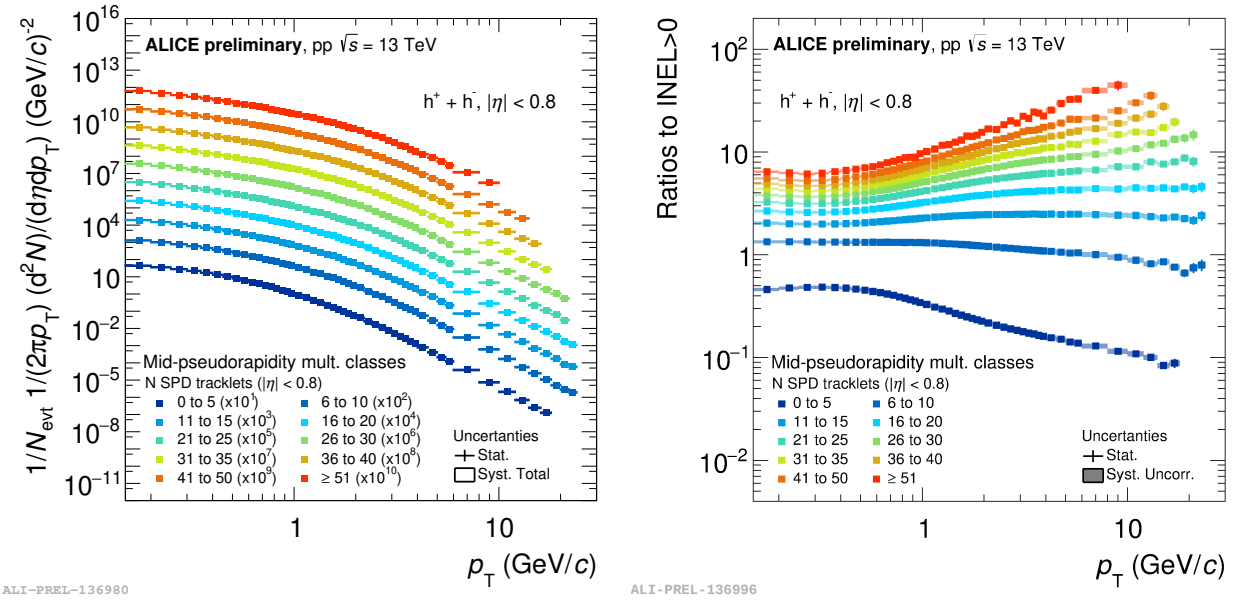


Figure 4.3: Measured $p_{\mathrm{T}}$ spectra of charged particles in tracklets bins (left) and their ratios to the INEL $> 0$ case (right) for pp collisions at $\sqrt{s} = 13$ TeV .

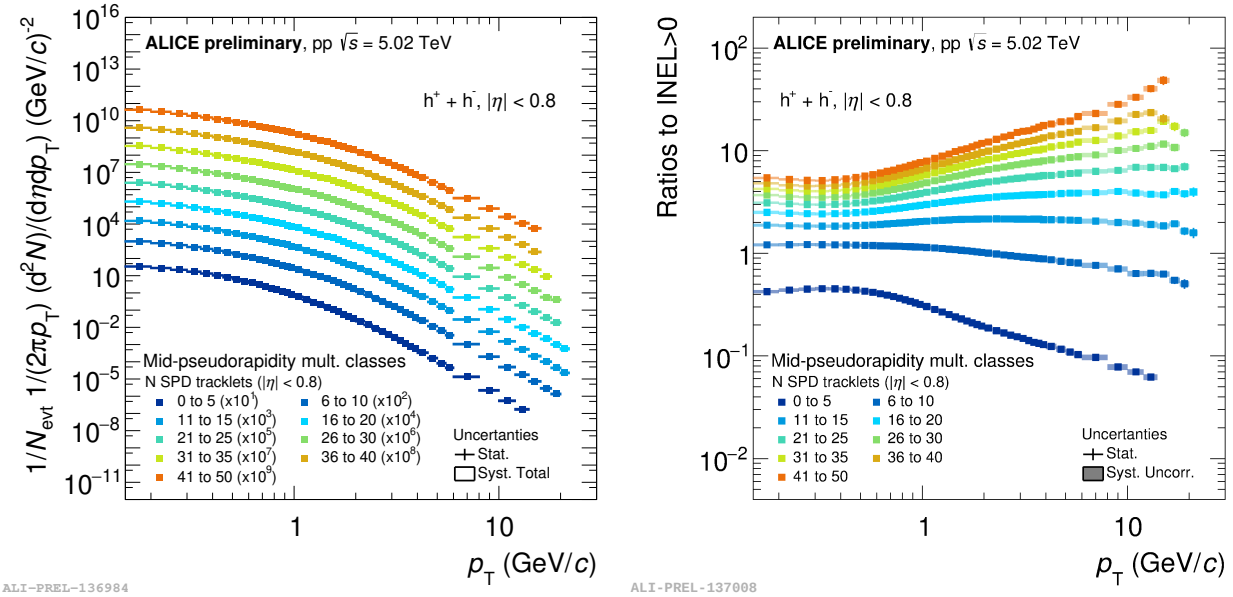


Figure 4.4: Measured $p_{\mathrm{T}}$ spectra of charged particles in tracklets bins (left) and their ratios to the INEL $> 0$ case (right) for pp collisions at $\sqrt{s} = 5.02$ TeV .

From the previous figures, 4.3 and 4.4, we can see how the spectra tends to grow when we move to the highest multiplicity bins for the central pseudo-rapidity multiplicity estimator. Since the multiplicity bins are measured with the tracklets in the central barrel, the mixture which we talked about for the V0M case is cosiderably reduced. As mentioned earlier, high multiplicity in the central barrel tends to jets, we can say that this result is strongly related to jet production.

### 4.1.3 Power law exponent vs multiplicity

Power law functions were fitted to the spectra in order to extract the exponent, the fits were done for $p_{\mathrm{T}}$ higher than 4.0 GeV/$c$. Figures 4.5 and 4.6 show the quality of the fits obtained for $\sqrt{s} =$

5.02 and 13 TeV data analyses.

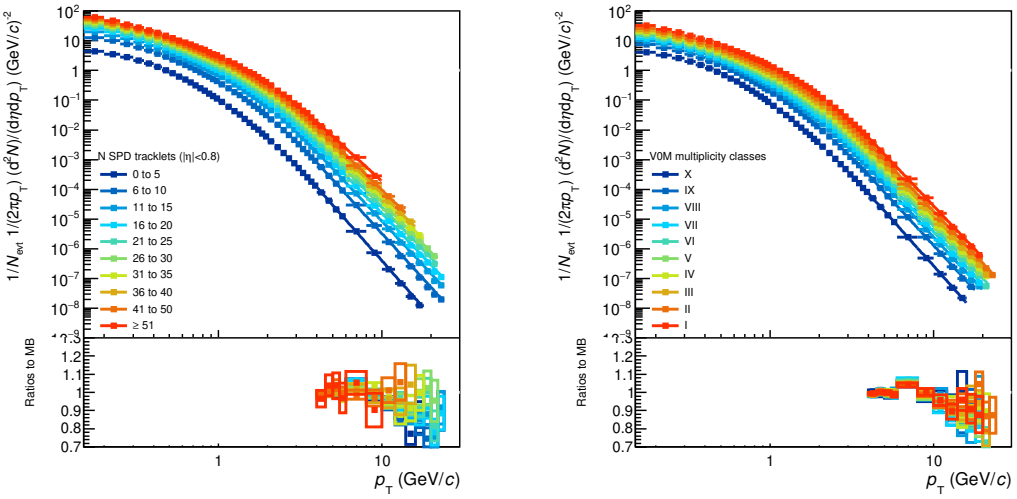


Figure 4.5: Power law fits and its ratios to the $p_{\mathrm{T}}$ spectra for the tracklets (left) and V0M (right) estimators for pp collisions at $\sqrt{s} = 13$ TeV .

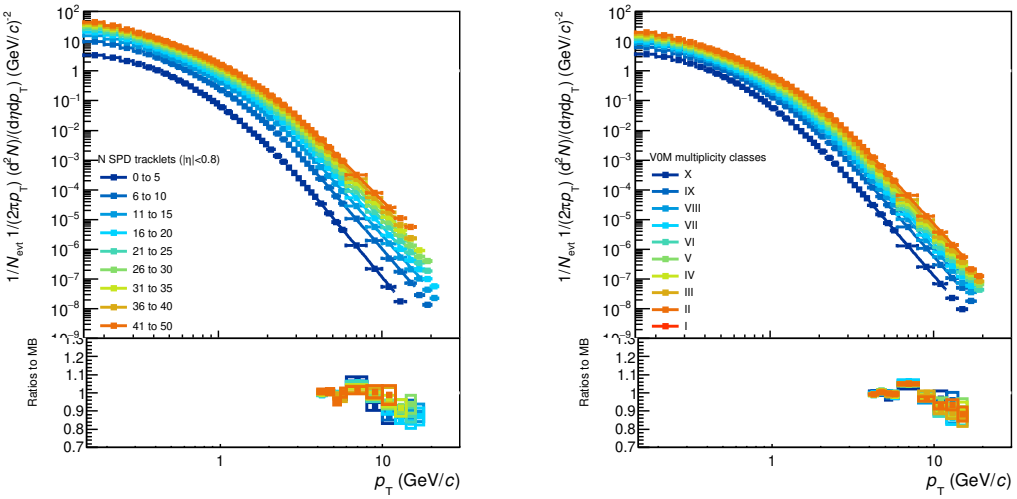


Figure 4.6: Power law fits and its ratios to the $p_{\mathrm{T}}$ spectra for the tracklets (left) and V0M (right) estimators for pp collisions at $\sqrt{s} = 5.02$ TeV .

The power law exponent as a function of multiplicity comparing two energies for a given multiplicity estimator in the same plot, is shown in figure 4.7.

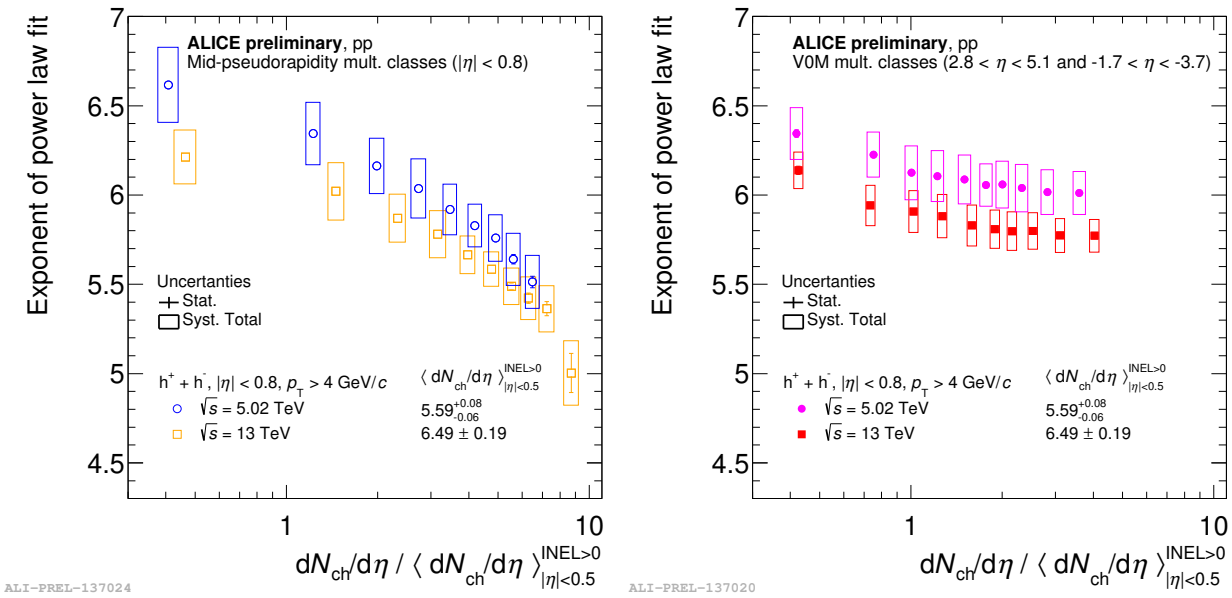


Figure 4.7: Power law exponent as a function of multiplicity comparing two energies for a given multiplicity estimator, tracklets (left) and V0M (right).

Power law exponent as a function of multiplicity for two multiplicity estimators for a given energy in the same plot, can be seen in figure 4.8.

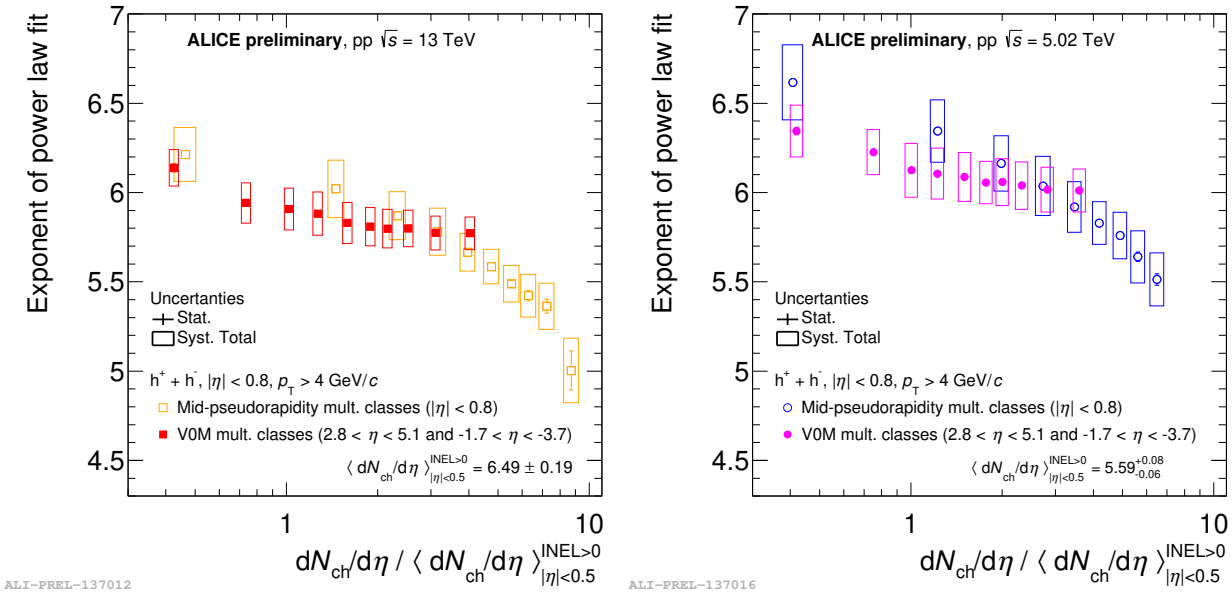


Figure 4.8: Power law exponent as a function of multiplicity, multiplicity estimators comparison, $\sqrt{s} = 13$ TeV (left) and $\sqrt{s} = 5.02$ TeV (right).

We have here another observable, power law exponent evolution in function of multiplicity, that confirm the statements observed in the ratios to INEL $> 0$ in previous sections. The exponent tends to saturate for the V0M case, like the ratios, while the exponent seems to rapidly get diminished when we move from low to high multiplicity.

### 4.1.4 High $p_{\mathrm{T}}$ charged hadrons integrated yields and comparison with heavy flavors hadrons

A comparison of the integrated yields of spectra in multiplicity bins divided by the INEL $> 0$ ones, for $p_{\mathrm{T}}$ values between 4 and 10 GeV/$c$, was done with the heavy flavors data. In figures 4.9 and 4.10 a comparison of the charged hadrons with the $J/\Psi$ and the $D$ mesons production can be observed. The results for high $p_{\mathrm{T}}$ charged particles are in agreement, at least qualitatively, with the heavy flavors results. The $D$ mesons were taken from the publication cited in the figures, and the $J/\Psi$ is a preliminary result from [28].

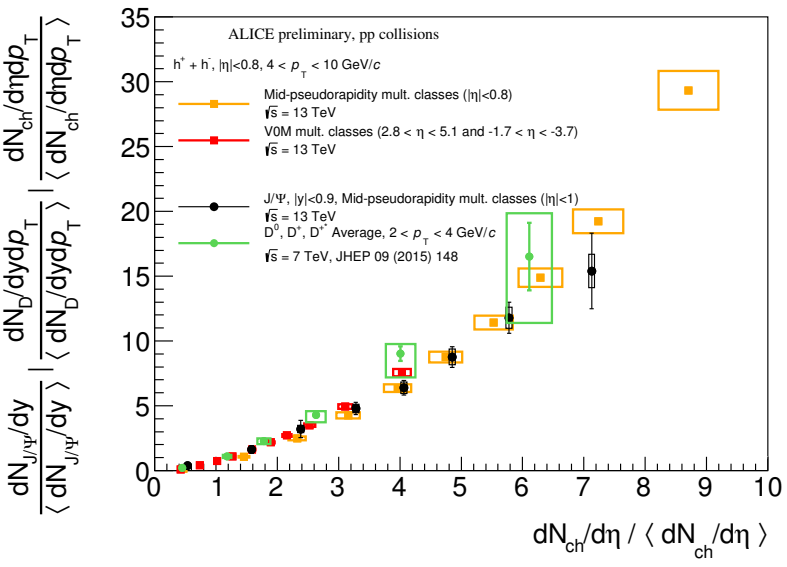


Figure 4.9: Integrated yields of spectra normalized by the INEL $> 0$ integrated yield as a function of multiplicity for charged hadrons (pp $\sqrt{s} = 13$ TeV ) and heavy flavors particles.

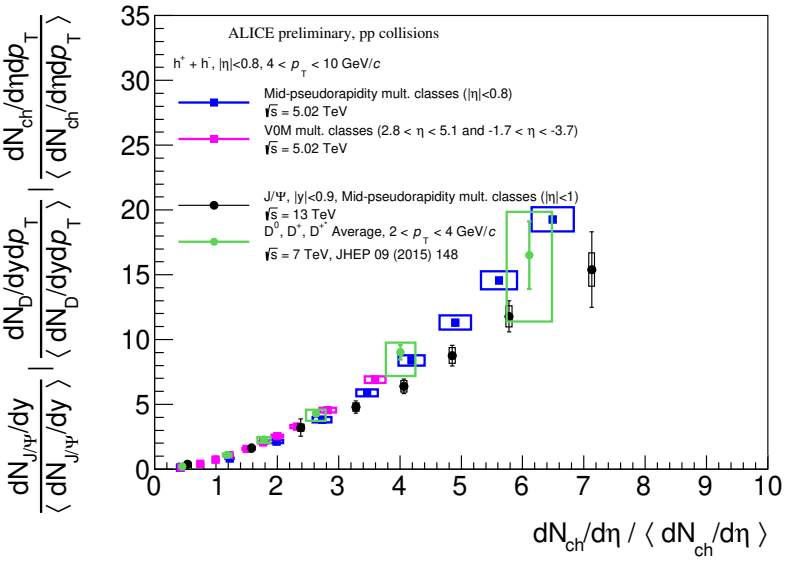


Figure 4.10: Integrated yields of spectra normalized by the INEL $> 0$ integrated yield as a function of multiplicity for charged hadrons (pp $\sqrt{s} = 5.02$ TeV ) and heavy flavors particles.

An energy and multiplicity estimator comparison between high $p_{\mathrm{T}}$ charged hadrons can be observed in figure 4.11

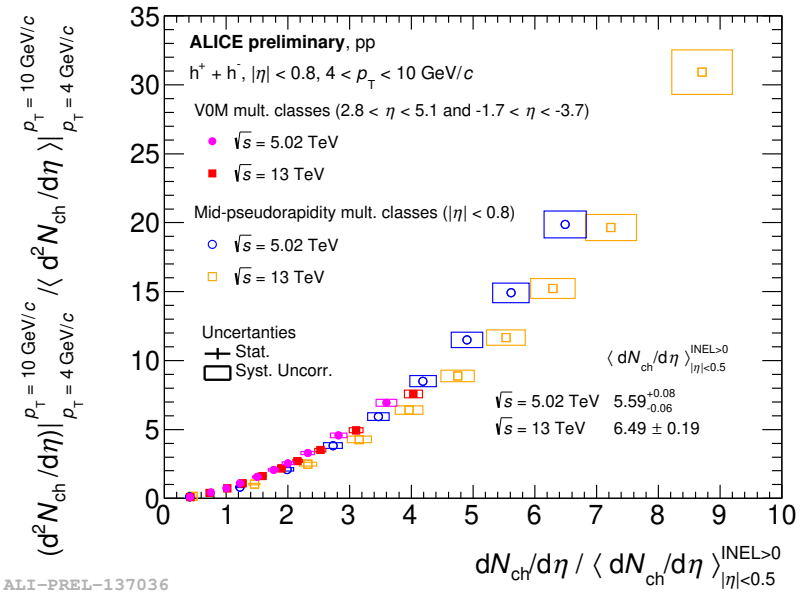


Figure 4.11: Integrated yields of spectra normalized by the INEL $> 0$ integrated yield as a function of multiplicity for charged hadrons (pp $\sqrt{s} = 5.02$ and 13 TeV ), both multiplicity estimators are plotted together.

From these results we can observe that the heavy flavor particles and the high $p_{\mathrm{T}}$ hadrons tends to have the same non linear rize with multiplicity. It suggest a common production underlying mechanism, and suggest and strong relation to jets too, since heavy flavor particles usually comes from hard (jetty) interactions.

### 4.1.5 Comparison of pp power law exponent with PbPb data

A comparison of the power law exponent vs multiplicity of the pp data with the PbPb data is presented in figure 4.12.

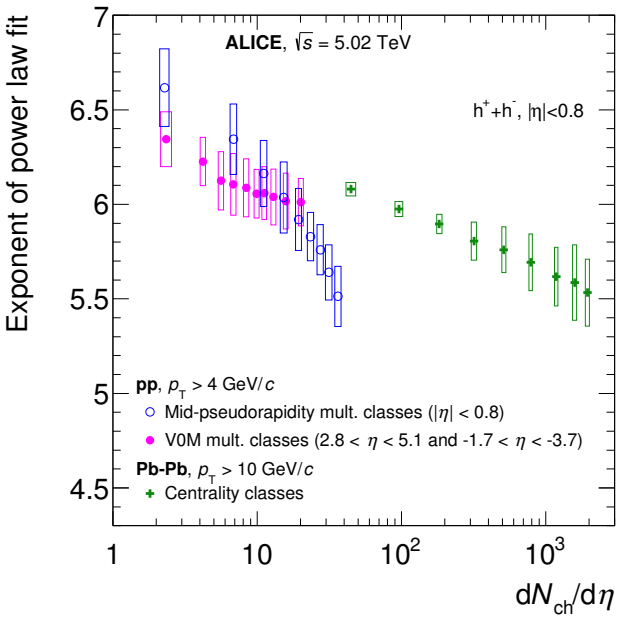


Figure 4.12: Power law exponent as a function of multiplicity for pp results compared with PbPb at $\sqrt{s} = 5.02$ TeV data.

It can be observed that the PbPb points seems to follow the tend of the V0M data. It sounds reasonable for us, since centrality is computed using the amplitude of the V0M detectors. In that way, the V0M multiplicity in pp collisions can be interpreted as a centrality-like measurement.

### 4.1.6 Comparison with MC models

We generated 1 billion of inelastic pp collisions, for each of the two energies ($\sqrt{s} = 5.02$ and 13 TeV ), using PYTHIA 8 (Monash Tune). For the multiplicity classes in the central barrel (comparison with Tracklets) we used bins of 1 $N_{ch}$ bin width to the multiplicity measured in $|\eta| < 0.5$. For the forward-backward (F-B) multiplicity classes (comparison with the V0M), we obtain the true multiplicity in the V0A + V0C pseudo-rapidity windows and we make bins of 5 $N_{ch}$ bin width, the $\langle dN/d\eta \rangle_{|\eta|<0.5}$ for each of the F-B multiplicity bins was taken to compare with the data. For EPOS-LHC and PYTHIA 6, we used the ALICE simulations at generation level, the number of events for this last two generators is around 50 millions, we used larger bins than in the case of PYTHIA 8 due to the lower number of available events.

The power law exponent as a function of multiplicity, comparing two energies for a given multiplicity estimator in the same plot, is shown in figure 4.13 for both multiplicity estimators.

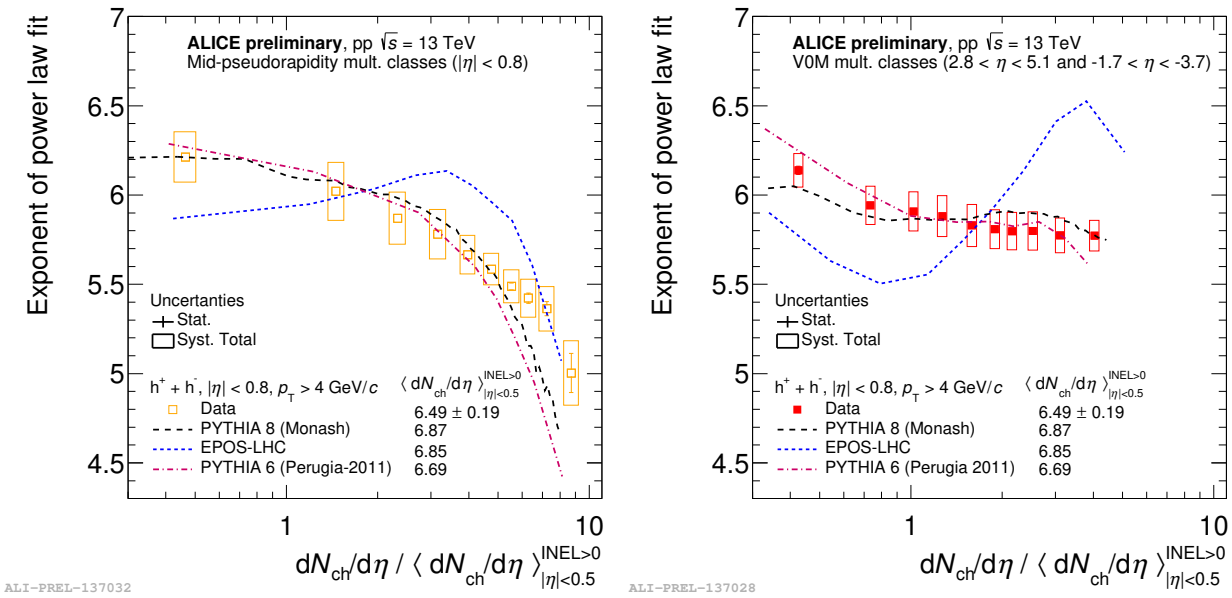


Figure 4.13: Power law exponent as a function of multiplicity, energy comparison, Tracklets (left) and V0M (right) multiplicity estimators, MC models are included in the plots.

As can be observed, PYTHIA 6 and 8 seems to be in good agreement with the data, at least qualitatively, since EPOS-LHC cannot describe the power law exponent. We know that EPOS-LHC is very good reproducing low-$p_{\mathrm{T}}$ (soft component) region, but extracting the power law exponent for high $p_{\mathrm{T}}$ region, we can conclude that it is not good describing the hard component of the collisions.

The integrated yields for the $\sqrt{s} = 13$ TeV analysis in comparison with MC models, and the dependence with the $p_{\mathrm{T}}$ cut can be observed in figures 4.14 and 4.15 respectively.

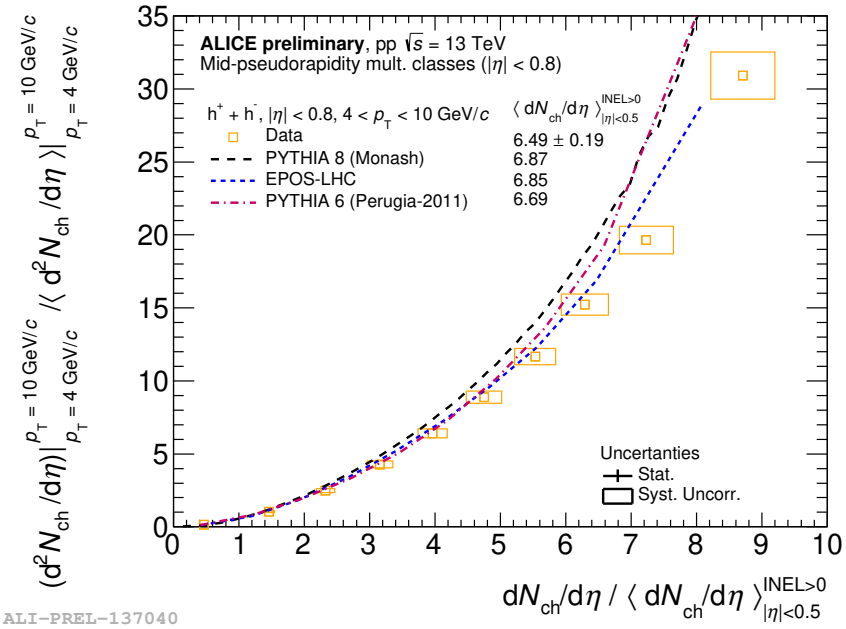


Figure 4.14: Integrated yields of spectra normalized by the INEL $> 0$ integrated yield as a function of multiplicity for charged hadrons produced in pp at $\sqrt{s} = 13$ TeV for central multiplicity estimator and its comparison with PYTHIA 6, 8 and EPOS-LHC.

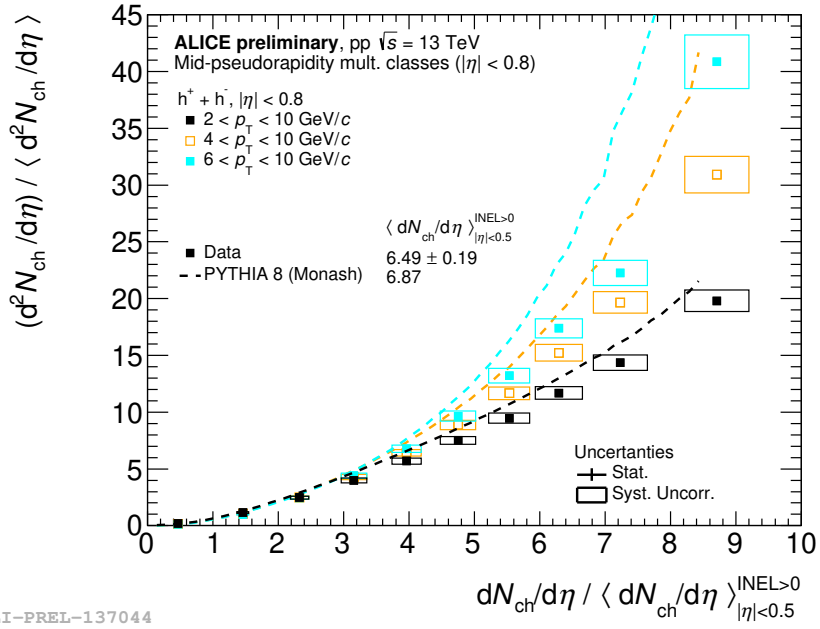


Figure 4.15: Integrated yields of spectra normalized by the INEL $> 0$ integrated yield as a function of multiplicity for charged hadrons produced in pp at $\sqrt{s} = 13$ TeV for central multiplicity estimator, for three different $p_{\mathrm{T}}$ cuts in comparison with PYTHIA 8.

From figure 4.14, it can be concluded that EPOS-LHC is the best describing the integrated yields vs multiplicity, it means, the productions o charged hadrons, but not the shape of the spectra, since it not was good describing the power law exponent.

# Chapter 5

# Conclusions

The ALICE experiment is designed to study the deconfined matter created during Pb-Pb collisions, but as we have seen in this work, the experiment is also useful to study pp collisions. The $p_{\mathrm{T}}$ spectra is one of the most important observables to extract information of the collisions in high energy physics experiments, since it revels the physical processes of the collision. It is also important that measure the $p_{\mathrm{T}}$ spectra in multiplicity bins can be take as baseline to compare the results with other colliding systems, like pA and AA.

We present the $p_{\mathrm{T}}$ spectra for pp collisions at two colliding energies, $\sqrt{s} = 5.02$ and 13 TeV , using two multiplicity estimators, one of them estimates the multiplicity in the central barrel $|\eta| < 0.8$ by taking the number of reconstructed tracklets, the other estimates the multiplicity in forward-backward pseudo-rapidity $2.8<\eta<5.1$ for V0A and $-3.7<\eta<-1.7$ for V0C by using the signal of V0 scintillators.

Different results are observed between the two multiplicity estimators. When we observe the ratios of $p_{\mathrm{T}}$ spectra in multiplicity bins over INEL $> 0$ for the tracklets case, we can see that for the higher multiplicity bins there is a constant rise of the ratios, may be caused by the jetty-like events that we are selecting by taking high multiplicity in the central barrel, in other words, we are mostly isolating hard QCD processes by selecting high multiplicity in the central barrel. For the V0M, we observe a saturation on the higher multiplicity bins, the ratios are nearly flat. This behavior observed in the V0M case can be explained as follows, for each V0M bin, we have a mixture of high and low multiplicity events on the central barrel, it does not matter that we have selected the highest multiplicity bin on V0M, there is a wide distribution of multiplicity in the central barrel, it means that for each V0M bin we have a mixture of low and high multiplicity in the central barrel events, so we have a mixture of soft and hard physics processes that contributes to the spectra, in that sense, the ratios stay flat.

In order to study the high $p_{\mathrm{T}}$ rise (high multiplicity trackles) and saturation (high multiplicity V0M) we have extracted the power law exponent for the spectra as a function of the event multiplicity by fitting power law functions. At high multiplicity in the central barrel, the exponent for the two energies seems to coalesce and to tend to the predicted QCD value, and also are in good agreement with the values measured for jets $p_{\mathrm{T}}$ spectra. For the V0M this is not observed for the reasons mentioned above, we have mixture of hard and soft QCD processes that contributes to the hadron production.

The extracted power law exponents for pp collisions at $\sqrt{s} = 5.02$ TeV were also compared with PbPb system at $\sqrt{s} = 5.02$ TeV . It can be observed that the PbPb exponents follow the trend of the pp exponents which were measured in V0M multiplicity bins, is not the case for the central pseudo-rapidity multiplicity estimator. This can be understand by the fact that V0M multiplicity bins in pp collisions are something similar to the centrality in PbPb. With the V0M we are selecting mixture of events of various multiplicities without bias in physics processes like the central pseudorapidity multiplicity estimator, that select Jets in high multiplicity. The power law exponent evolution seems to follows a very similar behavior between the two energies.

We have also compared the measurements with MC models. We have used PYTHIA6 and 8, that have incorporated Multi Parton Interactions (that allows multiple partons to interact in a collision) and Color Reconnection (which is the PYTHIA model that allow each parton interaction to be affected by the others) as phenomenological models additional to perturbative QCD models, and we also have used EPOS-LHC, which evolves the soft component with hydrodynamics independently from the hard component. We observed how PYTHIA 6 and 8 were good describing the power law exponent extracted from the data (at least qualitatively), while EPOS-LHC is far from describing it. This is a surprise, since at the moment, EPOS-LHC is the most accurate MC event generator for pp collisions, taking into account that most of the comparisons were done to low $p_{\mathrm{T}}$ dominant observables, like $<p_{\mathrm{T}}>$ vs multiplicity.

Finally we extracted the behavior of the ratio of the high momentum yields of the charged hadrons to the mean yield; compared for similar ratios of $D$ and $J/\Psi$ mesons. We observe a similar behavior for the charged hadrons and the heavy flavors which seems to point to an important similarity of production of high momentum hadrons and heavier mesons. By comparing the integrated ratios with MC models, we can conclude that EPOS-LHC is the best reproducing the high $p_{\mathrm{T}}$ particle production, but not the shape of the intermediate to high $p_{\mathrm{T}}$ spectra, as we have observed from the power law exponent studies.

Remarks: this work is important in order to understand the physics in proton-proton collisions, comparing with models that uses different physical models. This results are also important in order to compare the similarities and difference with more dense systems like PbPb in this case. The power law exponent can be associated with parameters of the Tsallis distribution to get information about the temperature of the system. It has also been found theoretically to be approximately valid by extracting multiple scattering processes.

# Bibliography


[1] J. Adam *et al.* [ALICE Collaboration], Nature Phys. **13**, 535 (2017) doi:10.1038/nphys4111 [arXiv:1606.07424 [nucl-ex]].

[2] J. Adam *et al.* [ALICE Collaboration], JHEP **1509**, 148 (2015) doi:10.1007/JHEP09(2015)148 [arXiv:1505.00664 [nucl-ex]].

[3] J. Adam *et al.* [ALICE Collaboration], Phys. Lett. B 753, 319 (2016) doi:10.1016/j.physletb.2015.12.030 [arXiv:1509.08734 [nucl-ex]].

[4] http://home.thep.lu.se/ torbjorn/pythia82html/QCDProcesses.html

[5] T. Pierog, I. Karpenko, J. M. Katzy, E. Yatsenko and K. Werner, Phys. Rev. C **92**, no. 3, 034906 (2015) doi:10.1103/PhysRevC.92.034906 [arXiv:1306.0121 [hep-ph]].

[6] P. Bartalini *et al.*, arXiv:1111.0469 [hep-ph].

[7] O. Busch [ALICE Collaboration], arXiv:1306.2747 [nucl-ex].

[8] M. Cacciari, G. P. Salam and G. Soyez, Eur. Phys. J. C 72, 1896 (2012)

[9] A. Ortiz, G. Bencedi and H. Bello, J. Phys. G **44**, no. 6, 065001 (2017) doi:10.1088/1361-6471/aa6594 [arXiv:1608.04784 [hep-ph]].

[10] X. Zhu [ALICE Collaboration], arXiv:1311.2394 [hep-ex].

[11] F. Abe *et al.* [CDF Collaboration], Phys. Rev. Lett. **68**, 1104 (1992). doi:10.1103/PhysRevLett.68.1104.

[12] T. Affolder et al. (CDF Collaboration) Phys. Rev. D 64, 032001 (2001) – Published 14 June 2001.

[13] https://en.wikipedia.org/wiki/Elementary_particle#/media/File:Standard_Model_of_Elementary_Particl

[14] http://home.thep.lu.se/Pythia/pythia82html/ColourReconnection.html

[15] https://aliceinfo.cern.ch/Figure/node/11218

[16] http://alice-collaboration.web.cern.ch/documents/tdr/index.html

[17] V. Khachatryan *et al.* [CMS Collaboration], [arXiv:1606.06198 [nucl-ex]].

[18] A. Ortiz Velasquez, P. Christiansen, E. Cuautle Flores, I. Maldonado Cervantes and G. Paić, Phys. Rev. Lett. 111, no. 4, 042001 (2013) doi:10.1103/PhysRevLett.111.042001 [arXiv:1303.6326 [hep-ph]].

[19] M. Petrovici *et al.* https://aliceinfo.cern.ch/Notes/node/477

[20] E. Pérez *et al.* https://aliceinfo.cern.ch/Notes/node/472

[21] G. Bencedi https://aliceinfo.cern.ch/Notes/node/476

[22] M. Floris and F. Fionda https://aliceinfo.cern.ch/Notes/node/478

[23] https://twiki.cern.ch/twiki/bin/view/ALICE/PWGPPEvSelRun2pp

[24] https://twiki.cern.ch/twiki/bin/view/ALICE/AliceHMTFEstimators

[25] V. Vislavicius https://aliceinfo.cern.ch/Notes/node/422

[26] C. Y. Wong and G. Wilk, Phys. Rev. D 87, no. 11, 114007 (2013) doi:10.1103/PhysRevD.87.114007 [arXiv:1305.2627 [hep-ph]].

[27] B. Kim *et al.* https://aliceinfo.cern.ch/Notes/node/603

[28] S. Weber, https://aliceinfo.cern.ch/Notes/node/594

[29] https://www.dropbox.com/s/0igf00icsdv1s0d/normalization1.pdf?dl=0

[30] Prabhakar Palni, https://aliceinfo.cern.ch/Notes/node/510

[31] Beomkyu Kim, https://aliceinfo.cern.ch/Notes/node/603

[32] https://indico.cern.ch/event/578078/contributions/2659826/

[33] https://indico.cern.ch/event/617445/contributions/2777444/

# Presentations at CERN meetings

https://indico.cern.ch/event/634192/contributions/2566158/attachments/1452850/2242315/ALICE-PF-S_IGA_03052017.pdf

https://indico.cern.ch/event/630937/contributions/2552496/attachments/1442807/2222140/ALICESPECTRA_10042017.pdf

https://indico.cern.ch/event/625549/contributions/2529744/attachments/1438043/2213417/ALICE-LFPREVIEW_03042017.pdf

https://indico.cern.ch/event/619127/contributions/2499141/attachments/1426292/2189133/ALICE-LF_13032017.pdf

https://indico.cern.ch/event/612807/contributions/2477468/attachments/1415386/2167056/ALICE-LF_20Feb2017.pdf

https://indico.cern.ch/event/613713/contributions/2474024/attachments/1411850/2159847/ALICESPECTRA_13Feb2017.pdf

https://indico.cern.ch/event/592525/contributions/2397550/attachments/1389729/2116526/PWG-LF_15Dec2016.pdf

https://indico.cern.ch/event/558577/contributions/2255664/attachments/1315186/1969987/ALICE_spectra_21july2016. pdf

https://indico.cern.ch/event/564021/contributions/2279841/attachments/1325486/1989588/ALICE_SPECTRA_22Aug20 16.pdf

https://indico.cern.ch/event/571893/contributions/2314153/attachments/1343342/2024160/ALICE-ICN_26Sept2016.pdf

https://indico.cern.ch/event/580355/contributions/2355877/attachments/1363819/2064998/ALICE_SPECTRA_31Oct20 16.pdf